A STEEP-SLOPE THRESHOLD SWITCHING SELECTOR USING SILVER-DOPED POLYCRYSTALLINE ZINC OXIDE: FABRICATION, CHARACTERIZATION, & APPLICATION FOR 3D X-POINT MEMORY & NEUROMORPHIC DEVICES

by

Akshay Sahota

APPROVED BY SUPERVISORY COMMITTEE:

_____

Jiyoung Kim, Chair

_____

Jeong-Bong Lee

_____

Chadwin D. Young

_____

Qing Gu

ਮੈਂ ਆਪਣਾ ਇਹ ਉਪਰਾਲਾ ਆਪਣੇ ਮਾਤਾ ਪਿਤਾ ਜੀ ਨੂੰ ਸਮਰਪਿਤ ਕਰਦਾ ਹਾਂ,
ਜਿਹਨਾਂ ਨੇ ਮੈਨੂੰ ਇਸ ਕਾਬਲ ਬਣਾਇਆ ਕਿ ਮੈਂ ਇਹ ਕੰਮ ਕਰ ਸਕਾਂ।

To my parents

A STEEP-SLOPE THRESHOLD SWITCHING SELECTOR USING SILVER-DOPED POLYCRYSTALLINE ZINC OXIDE: FABRICATION, CHARACTERIZATION, & APPLICATION FOR 3D X-POINT MEMORY & NEUROMORPHIC DEVICES

by

AKSHAY SAHOTA, (MTech, BTech)

DISSERTATION

Presented to the Faculty of

The University of Texas at Dallas

in Partial Fulfillment

of the Requirements

for the Degree of

DOCTOR OF PHILOSOPHY IN

ELECTRICAL ENGINEERING

THE UNIVERSITY OF TEXAS AT DALLAS

December 2021

ACKNOWLEDGMENTS

This dissertation represents not only my hard work at The University of Texas at Dallas but is the most valuable academic milestone in the last decade of my life, an absolutely life-changing experience for me. My doctoral journey at UTD has been nothing short of amazing and is the outcome of support and guidance by numerous people, whom I sincerely wish to thank.

There are no proper words to convey my heartfelt gratefulness and respect for my PhD supervisor, Professor Jiyoung Kim, for his invaluable advice, patience and steady support during my PhD study and it was truly an honor working with him. I sincerely acknowledge the opportunity he provided me to grow in this field of expertise. His constant guidance and overall insights have made this doctoral quest an incredibly inspiring experience for me. I utterly relish his amicable yet informative chats, and individual assistance in my academic and family endeavors. The meetings and conversations I had with him were vital in inspiring and motivating me to think outside the box, come up with new ideas considering multiple perspectives to form an objective and comprehensive critique. I could not have portrayed a better mentor – a 'Shifu', a 'Seonsaengnim', than him for my arduous doctoral study.

Together with my advisor, I want to show my gratitude to the rest of my doctoral thesis committee members, Professor Jeong-Bong Lee, Professor Chadwin D. Young and Professor Qing Gu, for their perceptive remarks and positivism during my doctoral proposal exam, and for their crisp questions and genuine feedback which spurred me to expand my research scope, and step outside my comfort zone. I deeply appreciate Professor Chadwin Young for allowing me to use his eCOMETS laboratory equipment to conduct my electrical characterization experiments and writing wonderful recommendation letters for me.

Although I have been enrolled with the Electrical Engineering department, but I would like to mention that the administrative staff in the Materials Science and Engineering department are memorable not only for their expeditious support but also for friendly behavior: Ashley Willess, Julieta Terry, Aura Thomas, Michele Brown, and others. I cannot begin to express my special thanks to Ashley Willess, who has been right there, helping out wherever and whenever needed, from the beginning of my application process, even when I have not had arrived in the United States. I am extremely appreciative of her assistance, her sincerity and dedication.

I thank all my previous and current fellow lab mates, including Dr. Antonio Lucero, Dr. Heber Hernandez-Arriaga, Dr. Yongchan Jung, Dr. Jaebeom Lee, Dr. Arul Ravichandran, Dr. Harrison Kim, Dr. Takashi Onaya, Dr. Su Min Hwang, Jaidah Mohan, Dan Le, and Jinhyun Kim for a cherished time spent together, and for all the fun we have had in the lab and other social feasts. I cannot leave UTD without specifically mentioning Arul, who helped me acclimatize smoothly in a completely new set up when I first arrived in the States and guided me continuously. It was sheer fun playing pranks on Dan – 'The Whining Mommy', seeing her getting paranoid and giving the most entertaining reactions every single time.

I also want to sincerely thank the whole NSERL cleanroom staff: Dr. Alexandra Joshi-Imre, Dr. Gordon Pollack, Zane Borg, and others, who worked diligently to keep the research facilities running efficiently and thus ensuring unobstructed research activities.

I deeply thank my parents, Saran Dass Sahota and Naresh Kumari for their unconditional trust, endless patience and support they have shown me through the culmination of all these years of distance learning. It was their unqualified love, ceaseless inspiration, persistent encouragement, and hopefulness that raised me up again when I got weary and was close to collapsing. My sisters,

Abhilasha, and Rajeshwari, my brother-in-law, Dharminder Kumar, and my cute little nieces, Anweshaa and Aradhya, have also been generous with their affection and encouragement throughout my doctoral study.

I would like to convey my thankfulness to my parents-in-law, Bhupinder Jalota and Neeru Jalota, for their emotional support, help and suggestions in personal affairs and sending me delicious food and desserts.

I want to thank my wife, Ruchi, for understanding me best even when I was more cantankerous than normal whilst I underwent this PhD journey, covering up my tracks whenever I messed stuff up and for being such a great companion. Her unlimited love, support, and encouragement helped me get through this poignant period in the most sanguine way.

Finally, I want to thank me for doing all this hard work, being strict on myself, taking no unnecessary days off, for never quitting, graciously accepting all the criticism and for just being me at all times. I am thankful to God for being able to fulfill the dream of being the first doctorate in the family.

GAMSAHABNIDA!

DHANNVAAD!

SHUKRIYA!

XIÈXIÈ!

GRACIAS!

THANK YOU!

October 2021

A STEEP-SLOPE THRESHOLD SWITCHING SELECTOR USING SILVER-DOPED POLYCRYSTALLINE ZINC OXIDE: FABRICATION, CHARACTERIZATION, & APPLICATION FOR 3D X-POINT MEMORY & NEUROMORPHIC DEVICES

Akshay Sahota, PhD
The University of Texas at Dallas, 2021

Supervising Professor: Jiyoung Kim

An assortment of emerging non-volatile memory (NVM) devices has displayed a surge of interest in being investigated for their implementation in energy-efficient bio-inspired neuromorphic computing. The intrinsic device physics of NVMs give them the capability to be employed for emulating the dynamics of a biological neuron and synapse. NVM devices are connected in a dense cross (X)-point circuit architecture thus enabling massive system-level parallelism necessary for a neural network. However, the leakage/sneak current that typically arises from neighboring unselected memory cells is considered as a stumbling block in enlarging X-point arrays. Metal-filament threshold switch has been suggested as a selector device, demonstrated on low leakage characteristics, that holds potentiality due to its straightforward metal-insulator-metal structure, superior performance, and excellent CMOS process compatibility.

This dissertation demonstrates research study on the electrical and surface characterization of nano-polycrystalline silver-doped zinc oxide (ZnO) thin films for threshold switching selector device, to propose a way for amending the prevalent selector drawbacks: threshold voltage (V_{th})

variabilities *i.e.*, intercell and cycle-to-cycle shifts and lousy DC cycling endurance. The current work demonstrates a novel approach to subside system variabilities by uniformly doping a crystalline selector medium *i.e.*, ZnO with Ag metal atoms, rather than incorporating an Ag active metal layer/electrode.

First, electrochemical deposition (ECD) process has been employed to slightly dope ZnO with Ag, because of its admirable dopant concentration controllability having atomic percent precision. ECD process helps in demonstrating the proof-of-concept experiment and provides an understanding of volatile switching behavior when ZnO is lightly doped with Ag. Next, "super-cycle ALD" technique has been evaluated, where alternating ZnO ALD and Ag metal ALD was employed for lightly doping/delta doping ZnO with Ag.

To fend off the shortcomings/drawbacks associated with both the ECD and ALD processes, RF magnetron co-sputtering process is the last fabrication method put to evaluation. Co-sputtering technique provides the wherewithal to control Ag doping levels when lightly doped composite targets (ZnO/Ag 100-x/x at. %, x=1,3,10) are employed. The switching parameters were observed to significantly improve and the trends have been explained based on surface characterizations with XPS, GIXRD, AFM, SEM, EDAX, ICP-MS, HR-TEM, and semiconductor parameter analyzer.

TABLE OF CONTENTS

LIST OF FIGURES

LIST OF TABLES

CHAPTER 1

INTRODUCTION AND BACKGROUND

1.1 3D X-point Memory Array Motivation

For processing proliferating volumes of data, the semiconductor industry has been confiding in the Dennard[1] and Moore's Law[2] for scaling down the size and scaling up the performance of traditional von Neumann based devices. Since last three decades, it has been the trend to scale down chip size, accommodating more transistors, expecting a continuous dip in price per bit and simultaneous enhancement in device performance and capacity. But the semiconductor industry has been struggling lately with scaling effect, and memory wall has become a grave challenge. Emerging non-volatile memories were thus developed to span the performance gap between fast processor and memory technology. However, device performance and chip capacity are directly driven by their application demand *i.e.*, cognitive tasks aimed to be performed by next generation computing systems, thereby driving the memory architecture to move in three-dimensions (3D).

The first breakthrough in memory technology happened in 1999, where the memory devices took advantage of the 3D structure with the development of 3D FinFET transistor.[3] It was a SRAM memory device made of logic transistors that was able to successfully solve many scaling issues, immediately followed by 3D DRAM. With the advancements in technology, DRAM device with a $4F^2$ cross-sectional (F is minimum feature size) cell area was successfully demonstrated,[4] that paved the way for future 3D memories having $4F^2$ cell area *i.e.*, 3D cross (X)-point architecture.

3D X-point architecture possess the potentiality for realizing a high-density memory architecture with fast processing speed, random access and comprising of non-volatile memory components having smallest possible cell size. In a X-point architecture, non-volatile memory device or a memristor is situated at the intersection of a bit-line (BL) and word-line (WL) constituting a cell area of $4F^2$. The density of this architecture can be enhanced by stacking identical array layers on top of one another. So, if 100 layers are stacked over each other, the density of memory elements amplifies by 100 times. Figure 1.1a shows an illustrative example of a 3D X-point architecture,[5] and Figure 1.1b displays the commercially available 3D X-point memory device named Optane. Nonetheless, X-point structure is a promising architecture for implementation of massive parallel computing algorithms based on the weighted sum and resulting weight update operations, carried out in conventional brain-inspired computing.[6–8] Adopting a X-point architecture for neural computing is expected to cut down the energy costs owing to parallel processing capability.[9] Hence, X-point can potentially and effectively mimic brain functionality.

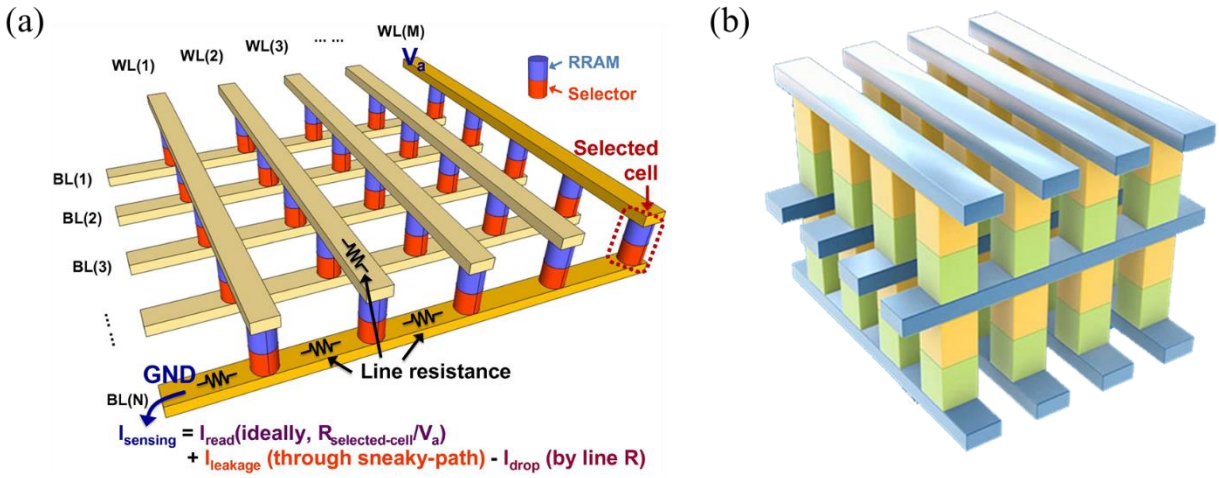

Figure 1.1. Schematic view of (a) typical 3D X-point array architecture with world lines and bit lines having memory and selection devices at intersection points, and (b) commercially available Optane - 3D XPointTM Memory. (Image Source- https://www.cleanpng.com/png-3d-xpoint-intel-micron-technology-phase-change-mem-5896832/download-png.html).

1.2 Competing Characteristics of Non-Volatile Memory for Neuromorphic Computing

The evolution of information technology at an expeditious rate has quickly led to an upsurge of artificial intelligence (AI). However, the von Neumann bottleneck *i.e.*, the unwanted delays between the memory and processor, makes the conventional computing systems unreliable due to their volatile nature, thereby making them unfit for implementing AI systems. For addressing these potential roadblocks, various brain inspired memristor-based neuromorphic computing systems have been proposed which can adequately emulate synaptic responses. Although, the learning mechanism of human brain is not fully comprehended but the constant advancements in neurobiology have shed light on some of the operational principles behind the working of neurons (CPU) and synapses (memory). Figure 1.2 highlights the analogy between human brain operation and an artificial neural network.[10]

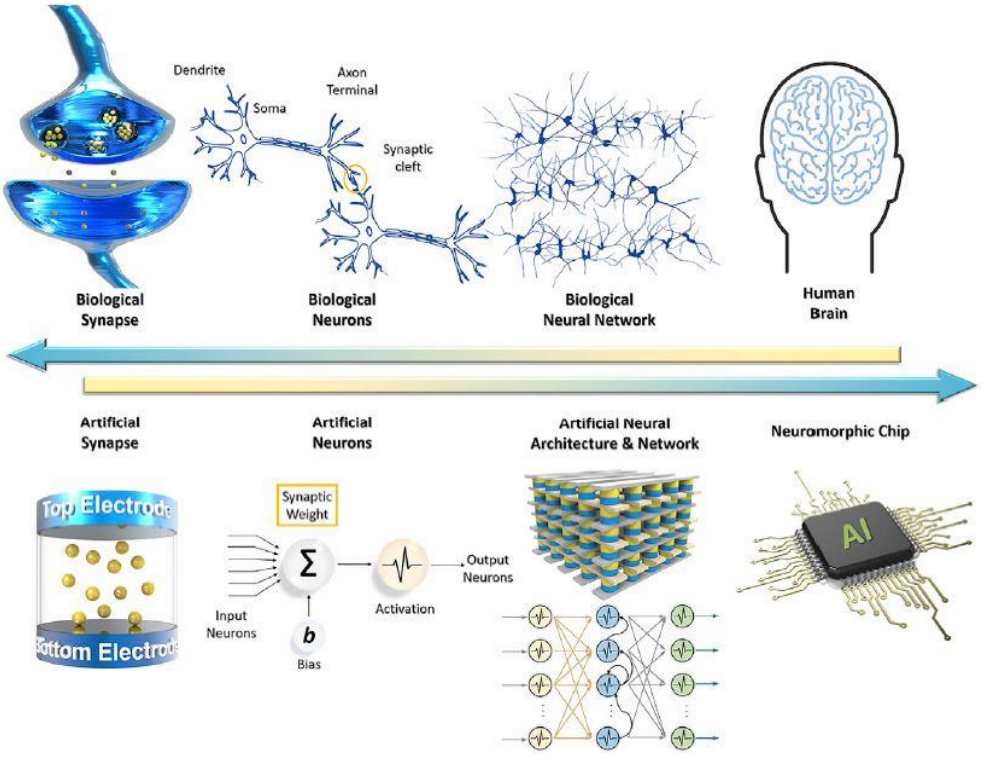

Figure 1.2. Comparative analysis of human brain operation and artificial neural network.

In contrast to the conventional CMOS computing architecture which follows Boolean data operations of saving data as either '0' or '1', human brain can save diversified states in individual synapse intelligently by modulating the synaptic weights.[10] Various types of non-volatile memories (NVM) have been investigated which can accommodate the mentioned features by changing their resistive states (*I-V* behavior) as per system requirement, in response to the applied voltage bias, thereby displaying synaptic plasticity.[11,12] Moreover, these memristive devices can be conveniently integrated in a X-point array, eventually into a 3D structure reducing the footprint to $4F^2$.[13,14] The comprehensive learning algorithms for neuromorphic computing are out-of-scope for this dissertation, and thus will not be discussed.

In the last decade, numerous neuromorphic computing systems were proposed, and IBM's TrueNorth (Figure 1.3)[15] stands out as the best-case model for utilizing a highly energy-efficient (20 mW/cm^2) X-point architecture to emulate synaptic behavior.[16] But this architecture suffered from a major drawback of volatile synaptic weights (*e.g.* SRAM or capacitive memory) *i.e.*, when power is turned off, all the data stored in synaptic weights is lost, accentuating the urgent necessity of emerging NVMs to be implemented in X-point array architecture for brain-inspired computing technology.

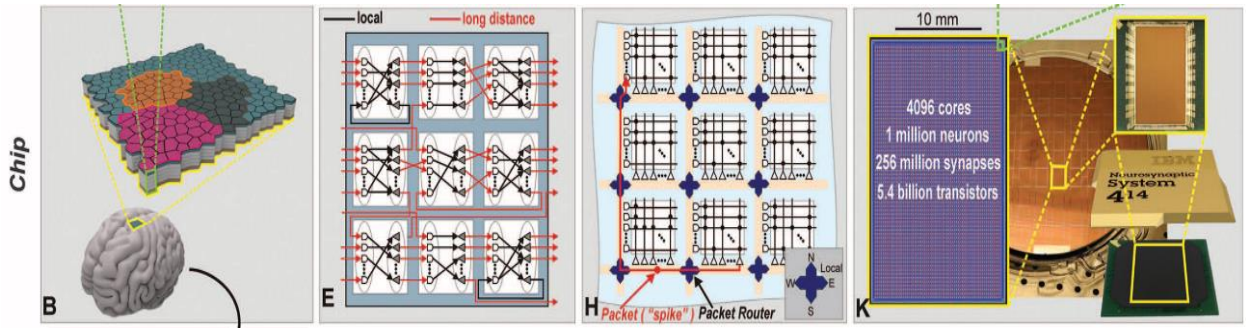

Figure 1.3. IBM's TrueNorth architecture; a neuromorphic CMOS integrated circuit developed by IBM.

1.3 Synopsis of Emerging Non-Volatile Memory (NVM) Devices

As previously discussed, 3D X-point architecture has the capability to perform massive parallel computing thus being a potential candidate for brain-inspired neuromorphic computing. Memristive devices whose conductivity/resistance levels can be adjusted when subjected to electrical stimuli, meeting the stringent requirements of area-efficient and energy-efficient information processing, are quite attractive for brain-inspired computing. Alternatively, a memory device that can attain multiple resistance or conductance states rather than just exhibiting binary operation, is required for enabling futuristic neuromorphic computing.[17]

The ultimate vision for large-scale X-point architecture is having a 3D stackable array, and individual cell addressability with minimum memory peripheral footprint of $4F^2$. The aggressive advancements in field of logic and memory devices, led to the evolution of FinFET, V-NAND etc. opening channels for emerging NVMs. Emerging NVMs or storage class memory breaks the 'memory wall' barrier having the computing functionality to store and process data simultaneously.[18] Resistive RAMs (ReRAM)[19,20] based on the concept of ionic migration, phase-change memory (PCM)[21,22] based on chalcogenide materials, and ferroelectric memories (FeRAM),[10] are some examples of representative emerging NVMs. Figure 1.4 shows classification of some of the most sophisticated memory technologies, highlighting their underlying device physics, operational principles and electrical characteristics (current-voltage or resistance voltage hysteresis).[10] Emerging memories find an easy applicability in 3D X-point architecture owing to their simple two-terminal structure,[23] where the switching layer (SL) is medially inserted in the bottom and top electrodes, enabling resistance to be reversibly switched amongst two or more states.[24] Figure 1.5 displays the list of various emerging NVMs with their performance matrices.[17]

	eSRAM	eDRAM	eFLASH	STT-MRAM	FeRAM	FeFET	PCRAM	RRAM	Vertical RRAM	Crossbar RRAM
	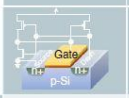					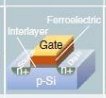	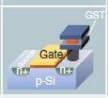	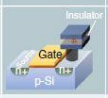	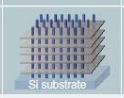	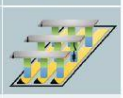
Cell size	120–150 F^2	10–30 F^2	10–30 F^2	10–30 F^2	10–30 F^2	10–30 F^2	10–30 F^2	10–30 F^2	4 F^2/N	4 F^2/N
Cell structure	6T	1T–1C	1T	1T–1MTJ	1T–1C	1T	1T–1PCM	1T–1R	1S–1R	1S–1R
Non-volatility	No	No	Yes	Yes	Yes	Yes	Yes	Yes	Yes	Yes
Write voltage	<1 V	<1 V	~10 V	<1.5 V	<3 V	<4 V	<3 V	<3 V	<4 V	<3 V
Write energy	~fJ	~10 fJ	~100 pJ	~1 pJ	~0.1 pJ	~0.1 pJ	~10 pJ	~1 pJ	~10 pJ	~1 pJ
Standby power	High	Medium	Low	Low	Low	Low	Low	Low	Low	Low
Write speed	~1 ns	~10 ns	0.1–1 ms	~5 ns	~10 ns	~10 ns	~10 ns	~10 ns	~100 ns	~50 ns
Read speed	~1 ns	~3 ns	~10 ns	~5 ns	~10 ns	~10 ns	~10 ns	~10 ns	~1 µs	~50 ns
Endurance	10^{16}	10^{16}	10^4–10^6	10^{15}	10^{14}	$>10^5$	$>10^{12}$	$>10^7$	$>10^7$	$>10^8$

Figure 1.4. Key emerging NVM device parameters with performance metrics.

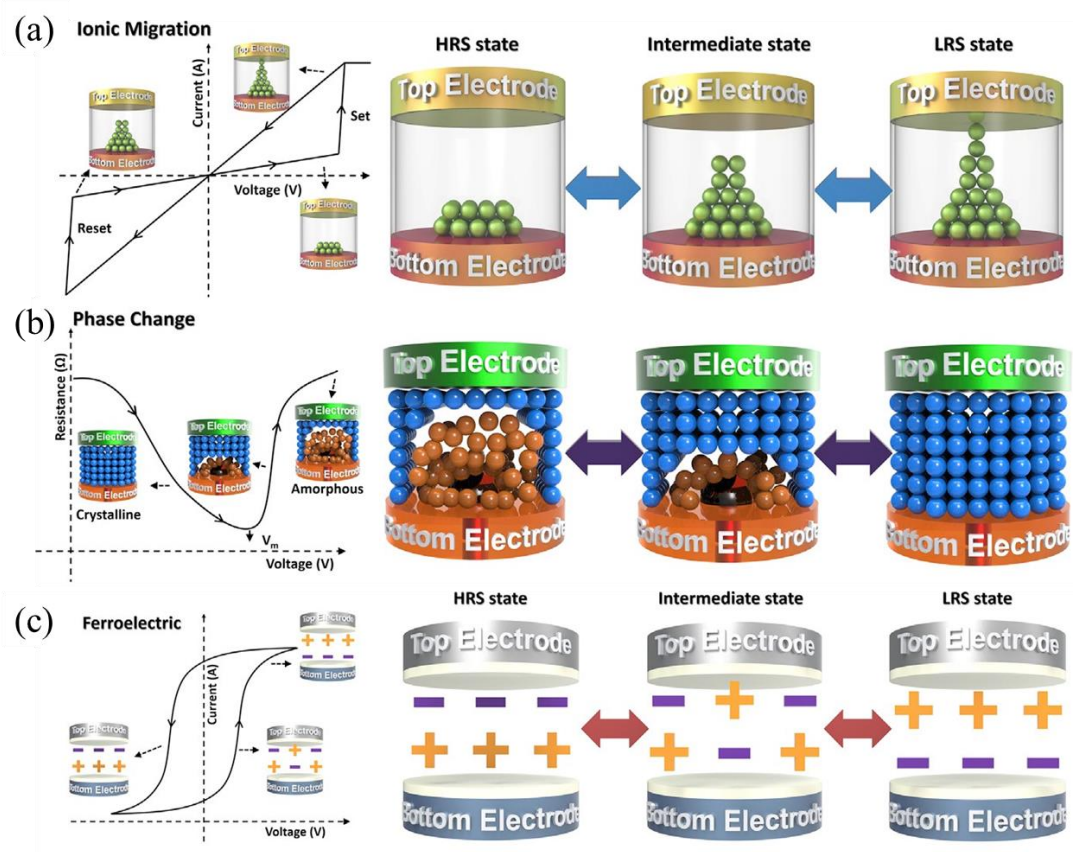

Figure 1.5. Operational principles and electrical characteristics of (a) Ionic migration-based memory devices, (b) Phase-change memory, and (c) Ferroelectric memory.

The aforementioned memristive devices typically have a metal/insulator/metal (MIM) stack, where a nonvolatile resistance change happens with application of external bias, leading to ionic movements due to local redox reactions. Figure 1.6 displays an exemplary *I-V* plot of a bipolar RRAM memory device.[25] In non-volatile memories, the ionic defects motion and local reduction-oxidation reactions are the driving forces behind resistance change. There are three different recognized mechanisms *i.e.*, – electrochemical metallization (ECM) found in conductive bridge random access memory (CBRAM) or metal-filament type switches; valence change mechanism (VCM); and finally the thermochemical mechanism (TCM).[26] ECM/VCM based devices involve cation/oxygen defects motion, and thus referred to as cationic/anionic.[26] This dissertation is only focused on the bipolar switching operations, hence TCM being unipolar operation mode is out-of-scope and will not be discussed here. The device physics for cation-based ECM and anion-based VCM will be discussed in the following subsection.

The ECM cell stack (MIM) conventionally constitutes of an active metal electrode (*e.g.*, Cu or Ag), a switching layer, and a counter top electrode (inert).[26] The switching or ion-conducting layer serves as the primary solid electrolyte or a secondary solid electrolyte. Figure 1.7 illustrates

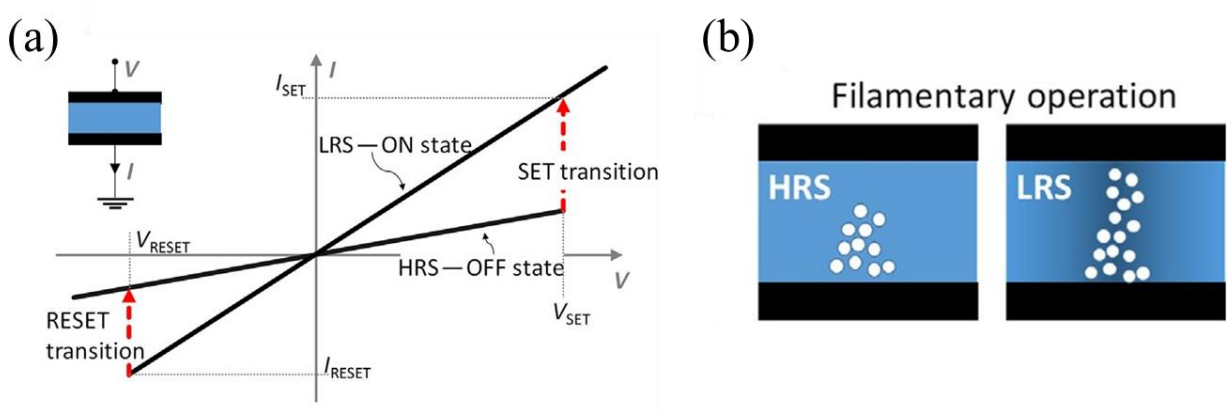

Figure 1.4. (a) *I-V* characteristics of a bidirectional memristive device, (b) switching phenomenon showing filamentary growth operation.

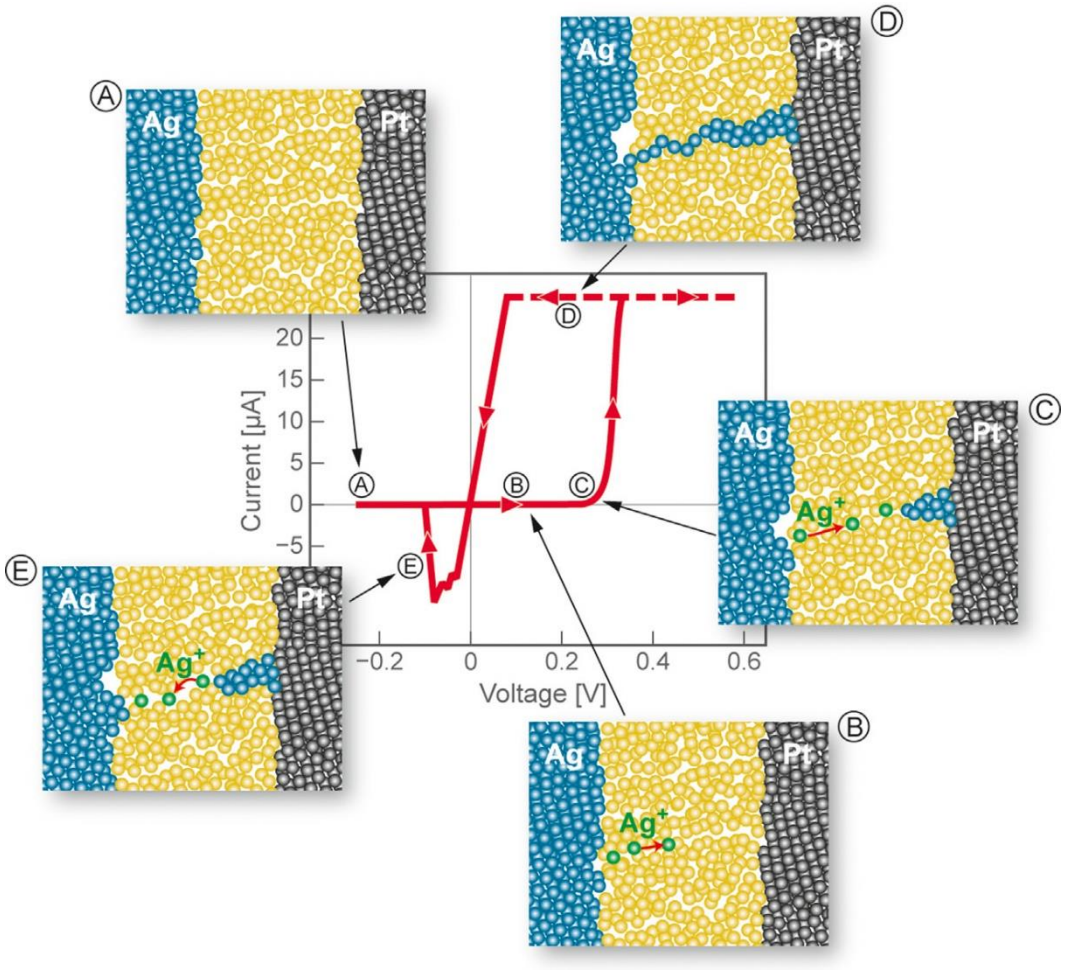

Figure 1.5. (A)-(D) SET, and (E) RESET process operations of an ECM device. In the shown figures, Pt acts as the bottom electrode (BE) which is grounded, and Ag serves as the top electrode (TE) where voltage bias is applied.

the typical *I-V* curves along with the electrochemical and physical events taking place in an ECM device.[27] During SET operation, a voltage (positive bias) is given to the active Ag electrode (Figure 1.7A). This oxidizes the electrode, leading to anodic reaction of $Ag \rightarrow Ag^{+} + e^{-}$, injecting Ag cations into the electrolyte layer (Figure 1.7B). These Ag cations then drift under the effect of electric field towards the cathode where a reduction reaction takes place, $Ag^{+} + e^{-} \rightarrow Ag$, and they get reduced to metallic Ag. Figure 1.7C shows the growth of Ag conductive filament (CF) towards the anode once a stable nucleus is formed. The device resistance drops significantly once the CF

touches the anode and electron tunneling comes into operation (Figure 1.7D). This configuration states the device is in low resistance state (LRS) and undergoes metallic conduction. The electrodeposition current density '*i*' is given by Faradays law, $i=zeR/V_M$. Assuming a cylindrical growth of CF, the time (t_{SET}) required to make the galvanic contact can be provided with following expression,[26]

$$t_{SET} = \frac{zqd\pi r_f^2}{V_M I_f}$$

where *z* corresponds to charge of cations, *q*–charge on electron, *d*–solid electrolyte thickness, r_f – CF radius, V_M – atomic volume of metal, and I_f being the growth current. Since, it is very challenging to precisely define these parameters, hence a more empirical version of this law has been proposed, according to which the time (t_1) required for CF formation at an applied bias of V_C is given by the following expression,[28] where β and t_0 represents the fitting constants, *k*–Boltzmann's constant, and *T*– temperature (°K).

$$t_1 = t_0 e^{-\beta \frac{qV_C}{kT}}$$

This implicates that there is exponential increase in programming speed with voltage, thus complies with the first-order approximation studies which points towards ionic migrations being responsible for CF formation. In the case of radial growth of cylindrical CF, the overall cell resistance (R_C) is expressed as,[28]

$$\frac{1}{dt}\frac{dR_C}{R_C} = \frac{dR_{C,norm}}{dt} \approx \frac{4\alpha}{D_0} e^{-\frac{E_a}{kT}} e^{\beta \frac{qV_c}{kT}}$$

where α represents an arbitrary constant, D_0–CF diameter at the formation time (*i.e.*, $t=t_1$), and E_a–ion hopping activation energy. Now, a high negative bias on Ag electrode is needed to RESET the device *i.e.*, electrochemical dissolution of the CF. All the ionic and electrochemical process tend

to reverse if the tunneling gap persists after SET operation, leading to filament dissolution (Figure 1.7E). This represents a very traditional filamentary growth model where the growth mode can be easily altered based on the reduction/oxidation rate,[29] which could potentially be helpful in controlling the threshold and hold voltages in switching devices.

A key thing to note here is that all the models discussed above, assumes that filament growth is cylindrical. So various *in-situ* characterizations were then performed to identify the actual morphology of filamentary formation. Interestingly, not just one but many filament morpholgies were discerned, such as chain of nanoparticles (Figure 1.8a),[30] inverted triangle shape (Figure 1.8b-c),[31,32] and dendritical structure (Figure 1.8d),[33] making it unclear to understand.

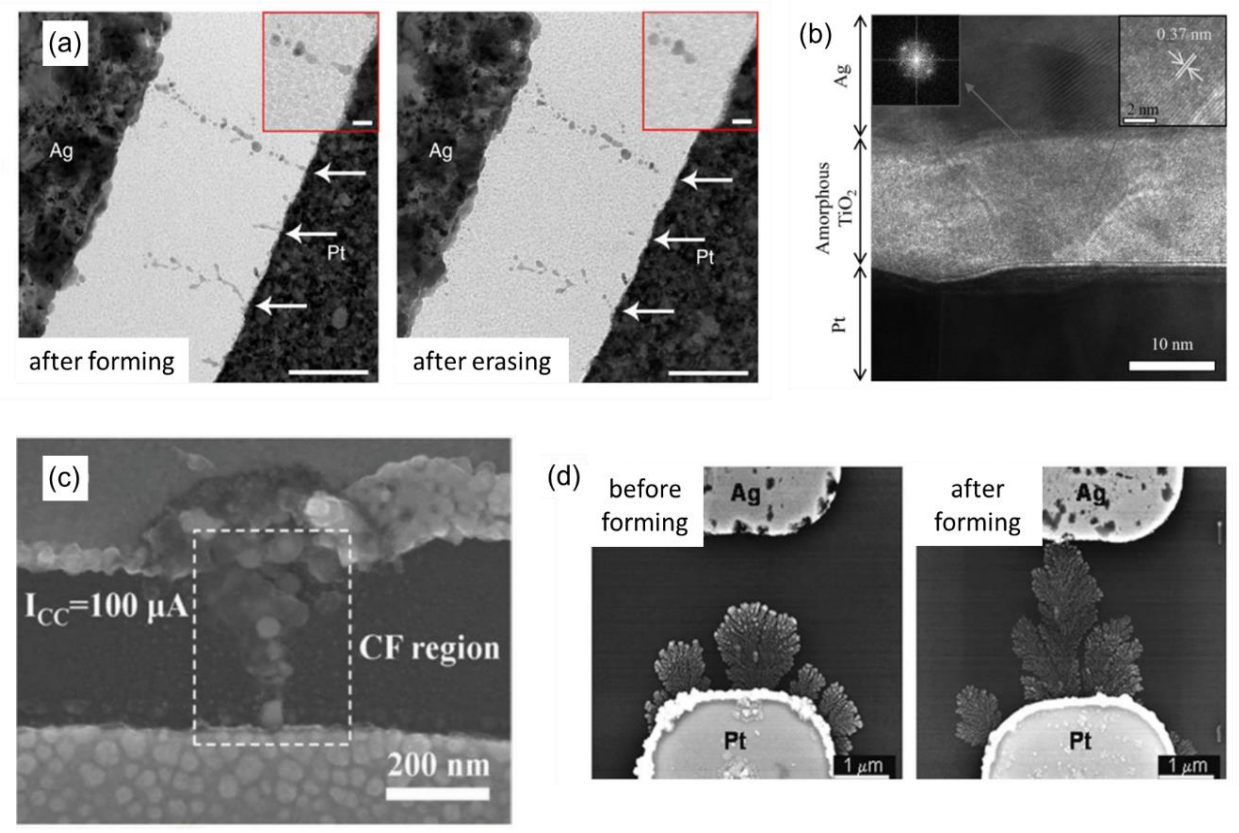

Figure 1.6. CBRAM cell in-situ characterizations to observe filament formation. Filament morphology observed, (a) nanoparticles, (b) and (c) inverted crystalline triangles, respectively. (d) dendritical morphology.

Moreover, it is not just that the filament morphology is diverse and hard to apprehend but it is incredibly challenging to capture the exact moment of CF formation using conventional *in-situ* characterization techniques because of the spatiotemporal tool resolution limit.

Although, CBRAM operating mechanisms have not be fully understood but in spite of that, recent research work highlights many interesting aspects of CBRAM devices. CBRAM functionality has been stated to be resembling the Ca^{2+} synaptic behavior displaying short-term and long-term plasticity, thus finding a direct application in neuromorphic computing networks.[34] As CBRAM contains electrochemically active metals (*e.g.*, Cu or Ag), they are also known as "diffusive or metal-filament type memristors". Device scaling in CBRAM has been investigated to cause significant enhancements in the switching characteristics, such as higher reproducibility, reduced cycle-to-cycle device variance, and lower probability for complete device failures as trimming down the device size leads to minimized joule heating in the vicinity of CF.[35] Possessing these attributes make CBRAM devices worthy candidates for high-density 3D X-point arrays.

1.4 Synopsis of Selector Devices

The technological restraints put by device scaling led to the development of emerging NVMs for novel parallel computational schemes beyond von Neumann, aiming brain-inspired neuromorphic computing. But development in NVMs alone does not imply successful implementation of 3D X-point arrays for neuromorphic computations. In a X-point array operation, whenever a cell is tried to be accessed, a voltage drop happens on that specific cell and in ideal conditions it is not expected to interfere with any other cells. When a voltage bias is applied to specific word-lines or bit-lines containing our target cell, it is expected to have a net voltage drop only on the desired cell, which then can be used to read, write/program or erase date from

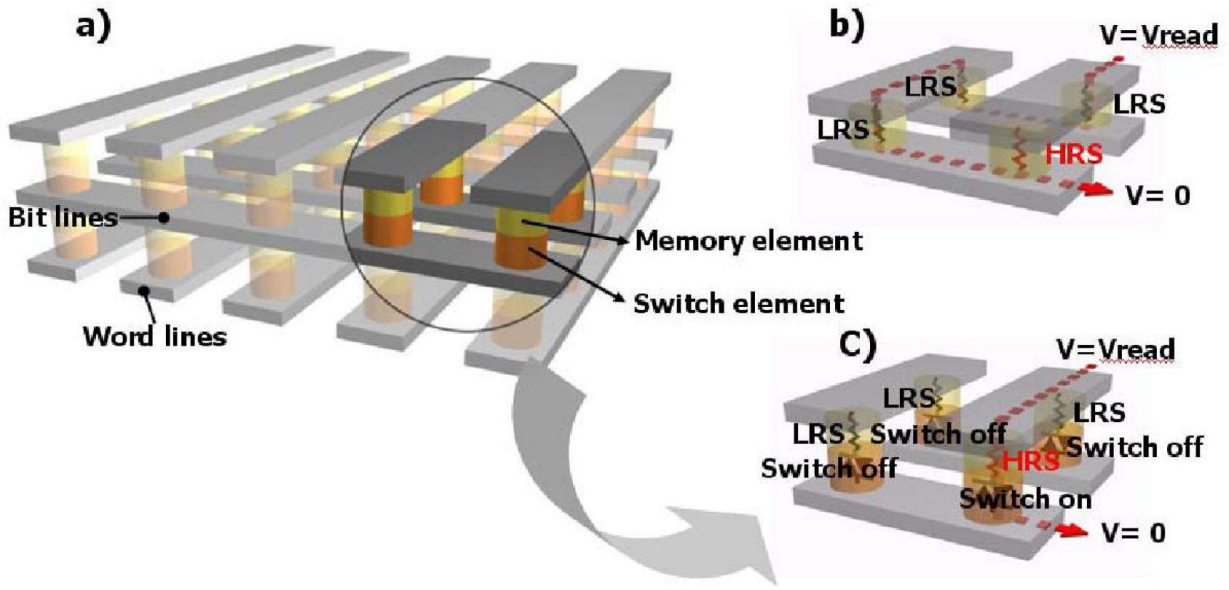

Figure 1.7. (a) Generalized 3D X-point memory array having a memory device and a switch i.e., selector device. (b) Read error/interference in the array without the selector device. (c) Rectified reading operation with selector device included in the circuit.

that cell. But intrinsic drawbacks of passive 3D X-point arrays involve parasitic current leakage in unselected/half-selected cells and series resistance comprised by interconnects. Therefore, access devices namely selectors are required to suppress parasitic leakages by adding them to the cross-point regions of a X-point architecture (Figure 1.9).[36] One solution is to use a transitor in series with a memory element. CMOS transistors can efficeintly serve purpose of a selector device by blocking the unwanted current leakage but the scaling limits of a transistor pose a challenge in achieving high scalability, due to their three-terminal structure, which is a must for ultra-high density 3D X-point arrays. *p-n* diodes can rectify the current flow but their unidirectional operation makes them unfit to be implemented with bipolar memories. Therefore, various kinds of novel selection devices, such as mixed ionic–electronic conduction (MIEC) device,[37,38] ovonic threshold switching (OTS),[39–41] insulator–metal transition (IMT),[42,43] and conductive bridging RAM (CBRAM)/metal-filament type selectors,[44–47] have been proposed. Having a simple two-terminal

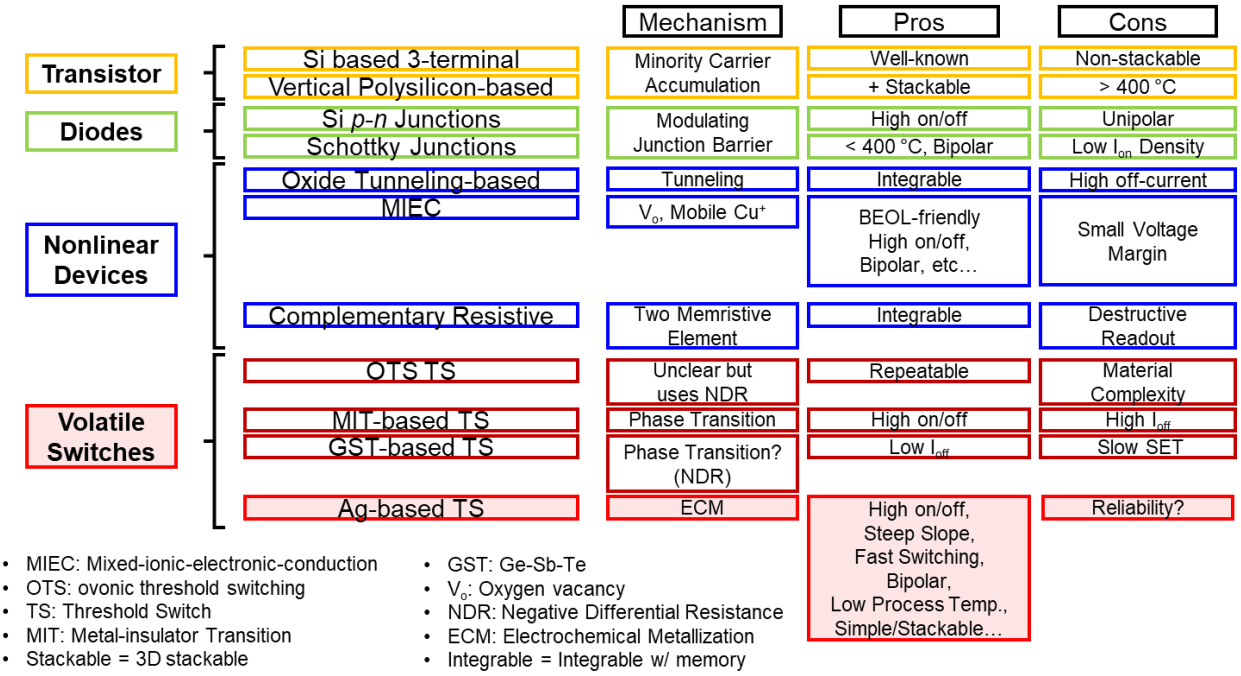

Figure 1.8. Memory selector devices' taxonomy and underlying mechanisms. Benefits and shortcomings for each case have also been summarized.

structure makes them potential selection devices meeting $4F^2$ footprint criterion. A comprehensive taxonomy of the selector devices has been summarized in the Figure 1.10, covering their detailed specifications and process parameters.[48–50]

Typical *I-V* characteristics of MIEC, IMT, OTS, and CBRAM-type selectors has been shown in Figure 1.11.[37,39,42,46,51] MIEC is an example of nonlinear selector devices, where the *I-V* characteristics resembles to that of the *p-n* junction diode and device operation is based on Cu-ionic migration and oxygen defect vacancies.[51] Despite of having a lot of excellent switching features, low on-current density, gradual subthreshold swing, low cycling endurance, and narrow voltage margin, makes MIEC selectors less desirable than that of thresholding selection devices, such as OTS, IMT, and CBRAM-type selectors. VO_2 is a classic example of representative IMT selector where the changes in electrical conductivity are observed when its crystal structure shows

rearrangement referred to as Mott-Peierls transition.[42] IMT caught a great attention of researchers due to its high ON current density, lower cycle-to-cycle variance but suffers from the flaw of

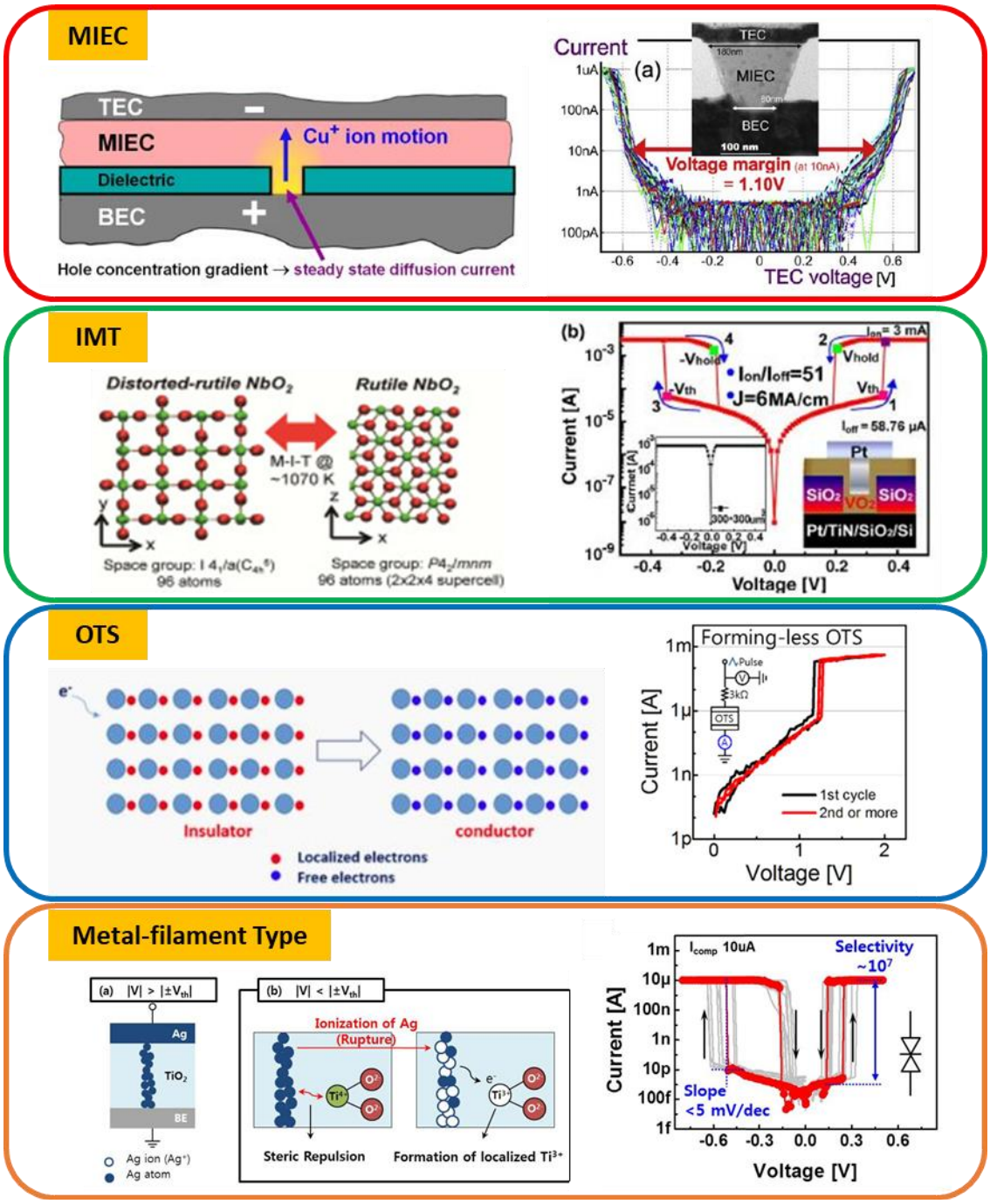

Figure 1.9. MIEC, IMT, OTS, and Metal-filament type selectors summarized with schematic switching mechanism and their typical I-V behavior.

having a high OFF-state (I_{Off}) current and a complex stoichiometry requirement thus leading to reproducibility issues.[42] Till date, OTS has been widely acknowledged as the most acceptable selector device for X-point applications. As previously mentioned in section 1.1 (Figure 1.1b), a 3D X-point memory is commercially available by Intel, called "Optane".[40] It consisted of PCM memory cells integrated in series with OTS selector device. OTS offers many advantages due to their favorable switching behavior which fulfill the criteria for ideal selector prerequisites, such as abrupt TS slope (<1 mV/decade),[52] high cycling endurance (>10^{11} cycles),[53] fast turn-on speed (<2 ns) and delay time (<8 ns),[54] and the newly reported binary telluride based OTS devices has good thermal stability (>450 °C) that contains C and B as constituting elements,[55] enabling them to survive back-end-of-line (BEOL) integration process. Additionally, in the stress measurements, OTS shows very stable ON and OFF states making it a robust candidate for selection process in a circuit. Following the discovery of threshold switching operation in amorphous chalcogenide glass materials by Ovshinsky in 1968,[56] OTS became a widely studied topic and many theoretical models were put forward to provide understanding on its switching operation but still the OTS phenomenon remains partially proven. The material complexity of OTS *e.g.,* TeAsGeSiSe, $Ge_2Sb_2Te_5$, or AsTeGeSiN, has always remained a downside of its selection device application. Although, some recent breakthrough was made regarding the material complexity by H. Hwang's group at POSTECH developing a much simpler binary OTS composition, but the persisting high OFF-state current leakage still hinders its successful application in ultrahigh density applications.

A typical selection device is ideally expected to satisfy a certain parameter requirement criterion for its practical implementation. An ideal selector should exhibit extremely low OFF-state leakage current (I_{off}), enabling a bigger sense margin in a X-point array that can provide

system functionality at a lower power budget. It is propsoed to have a high ON-state current density for a selector, so as to deliver sufficient current to the co-integrated memory cell in order read/write operations can be carried out. For this reason, a high selectivity ratio (I_{on}/I_{off} *i.e.*, high nonlinearity, NL) is desirable. Additionally, an ideal selector should have a simple two-terminal structure, a stable AC endurance, fast switching speed, superior device uniformity, broad voltage margin between ON and OFF states, memory device compatibility, high thermal stability, low temperature fabrication, and 3D stackability.[48–50] Table 1.1 summarizes all the detailed specifications necessitated for a selector.

Table 1.1. A summary of requisite characteristics for an ideal selector device.

FEATURES	**TARGET parameters**
Selectivity ratio (I_{on}/I_{off})	~ 10^8
On-state current density, J_{on}	≥ 1 MA/cm^2
Switching slope (subthreshold swing, SS)	< 10 mV/decade
Switching speed (turn-on and dissolution)	≤ 100 ns
Thermal budget	≤ 400 °C
Device uniformity (variances)	ΔNL, ΔJ_{ON}, ΔSS, ΔV_{th} < 5%
AC endurance	≥ 10^{10}
Thermal stability	≥ 85 °C
Bipolar operation	Yes
V_{th} & V_h tunability	Desired
Memory collocation	Yes

1.5 Synopsis of Silver-based Metal-filament Type Selector Devices

Metal-filament (CBRAM) type threshold switching (TS) selector devices represents another class of selection devices where thresholding properties are based on the instability of the metallic CF. At first, a voltage bias at low compliance current is applied to the CBRAM, which tends to form an unstable filament, programming the device. This phenomenon of weak and permanent filament formation is called as electroforming (EF). To implement this device for threshold switching operation, the property of spontaneous self-rupturing of unstable CF on removal of applied bias, is exploited. The underlying device physics for metal-filament type TS devices is very similar to that of CBRAM-type memory devices (Section 1.3). Figure 1.12 schematically shows the difference between filament formation process of a CBRAM-type memory *i.e.*, non-volatile switching (memory switching) and metal-filament type TS device *i.e.*, volatile switching (threshold switching).[25] Metal-filament type selector operation can be alternatively achieved if there is only a limited passage of current through the selector device giving rise to a laterally narrow and unstable filament. *In-situ* TEM characterization clarifies the

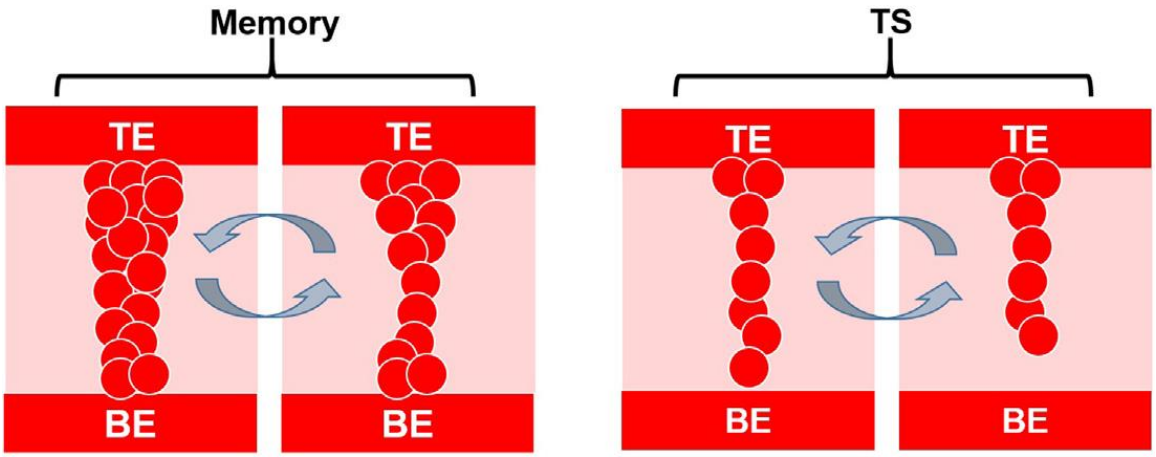

Figure 1.10. Schematic comparison between CBRAM-type memory operation (left) and TS device (right). As shown, TS happens when weak and unstable filament ruptures after removing external bias.

morphological difference between the filament formation (Figure 1.13),[31] showing that the thick and stable filament formation is the origin of non-volatile memory switching, whereas in the case of volatile TS, a thin and unstable filament is formed. Shukla *et al.*[57] recently reported the first-

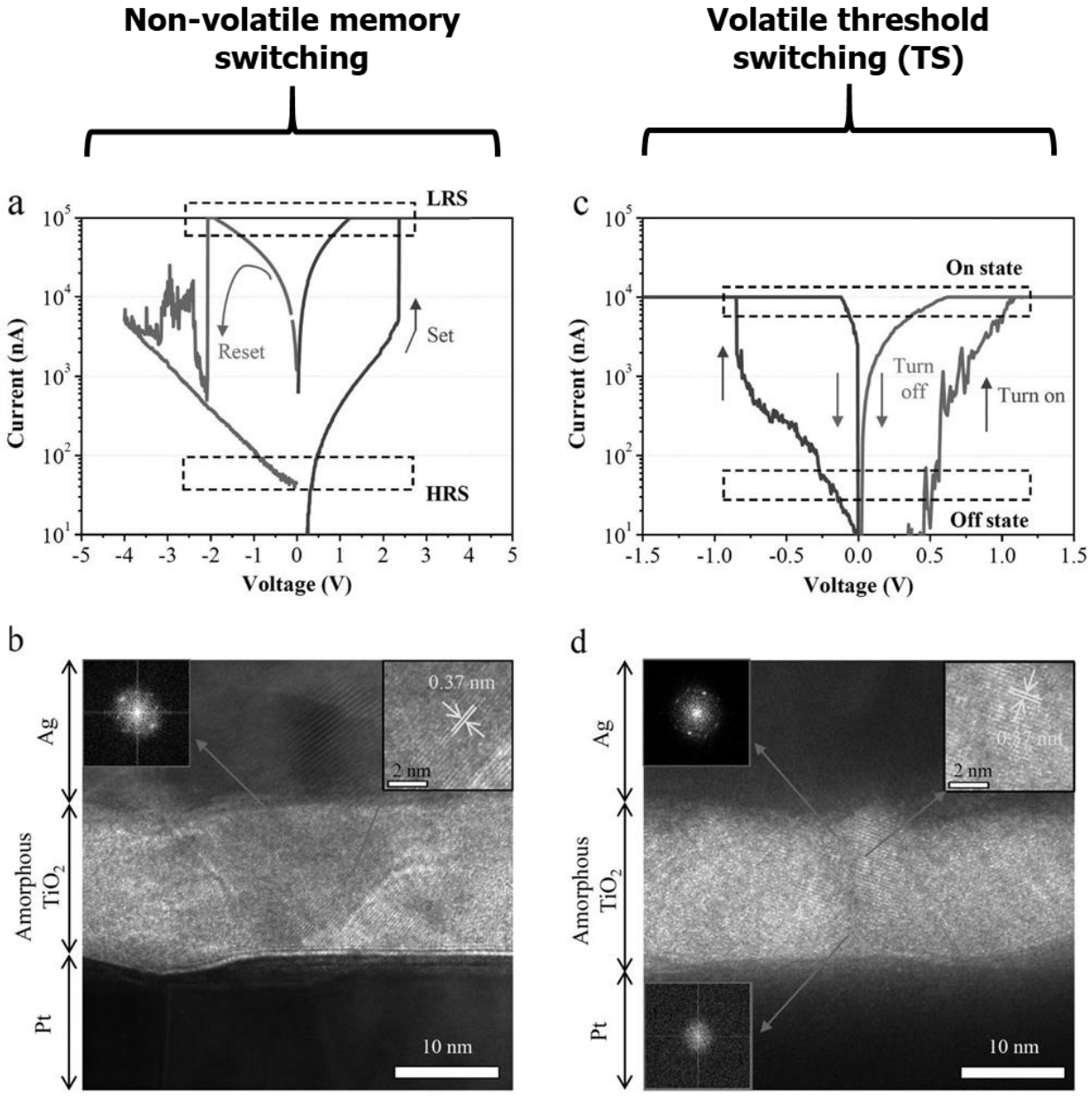

Figure 1.11. (a)-(b) respectively show *I-V* behavior and TEM, for a non-volatile memory switching at a high compliance current. (c)-(d) show *I-V* behavior and TEM, for the volatile TS at a low compliance current, respectively.

principle calculations of TS characteristics of several metal-filament type selector devices. For understanding the cause of memory switching and TS operation, a quantitative analysis was performed on the energy of formation, between cluster configuration at HRS, high-resistance state and filament configuration at LRS, low-resistance state, as shown in Figure 1.14a.[57] It was

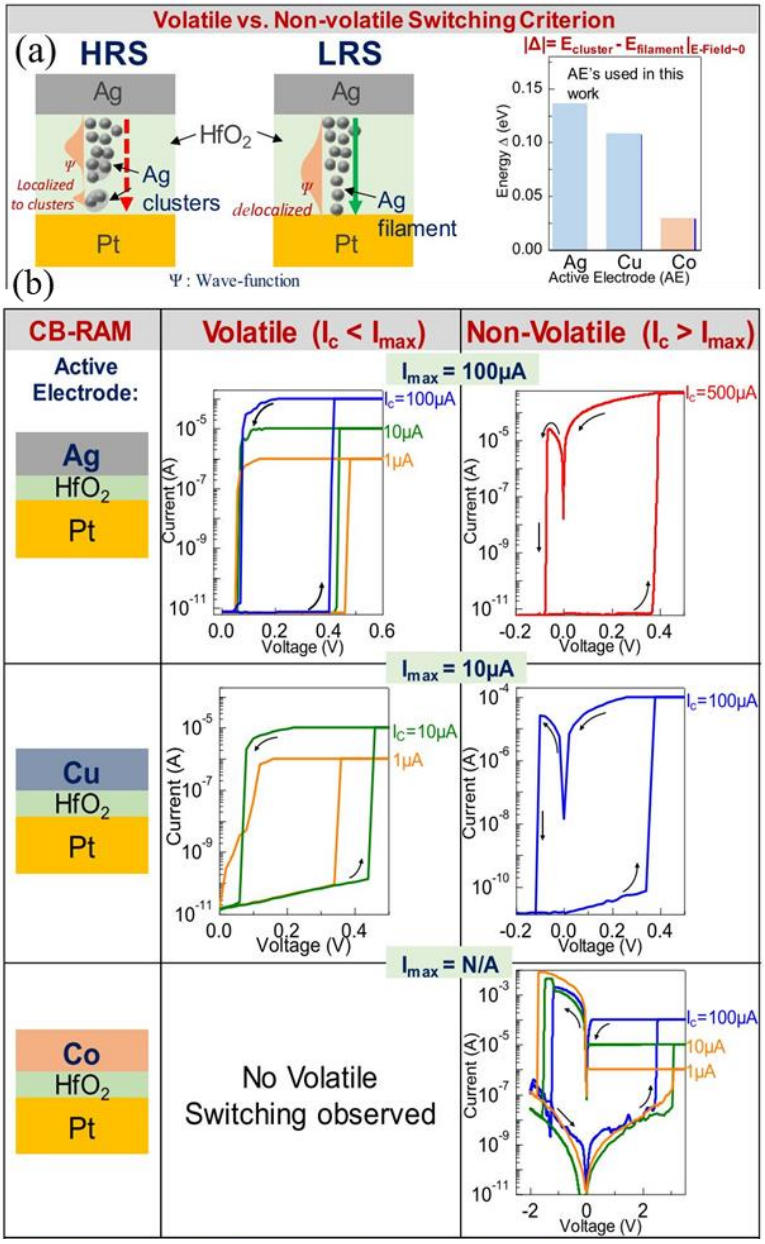

Figure 1.12. (a) Formation energy calculations and quantitative criteria for volatile and non-volatile (memory) switching. (b) Experimental I-V behavior for switching characteristics of Ag, Cu, and Co active electrodes.

concluded that spontaneous rupturing happens when the formation energy difference is large. Ag, Cu, and Co as active reservoir electrodes (Figure 1.14b)[57] were evaluated for this quantitative analysis. This study provided an understanding that Ag could be a better choice for electrode material for implementing TS behavior.

A theoretical explanation has been suggested to elaborate on the spontaneous self-rupture process of the unstable CF when voltage bias is removed (Figure 1.15).[58] As per this theory, the filament is believed to grow in a spheroid manner where the growth radius is given by, $R_{sph} = \alpha R_0$, α being the geometric factor.[59] The net nucleation barrier energy W(E) with respect to E, electric field is equated as per the following relationship.

$$W(E) = \frac{W_0 \alpha^{3/2} E_0}{E} = \frac{W_0 \alpha^{3/2} dE_0}{V}$$

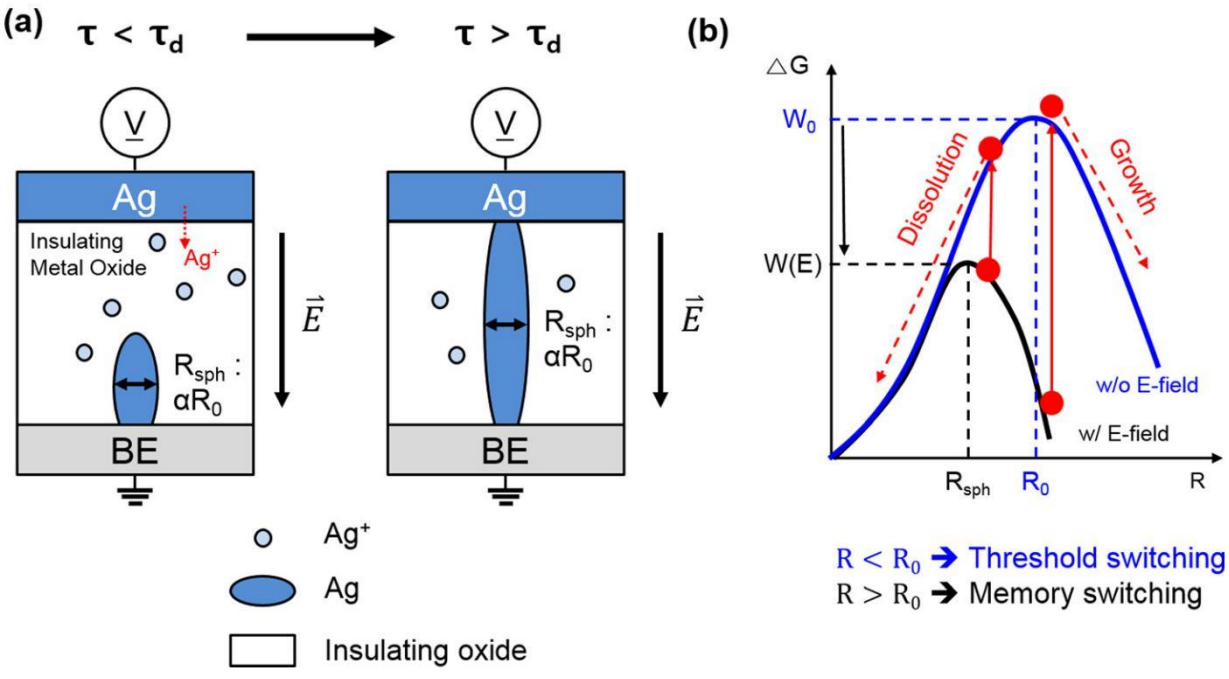

Figure 1.13. Physical explanation for the distinction between non-volatile memory, and volatile threshold switching characteristics considering theory of field-induced nucleation.

where W_0–represents the zero-field nucleation barrier energy and E_0 represents the factor for voltage acceleration which is independent from any external temperature/field. E_0 typically has a value of 1 MV/cm, *d* and *V* represents switching layer (SL) thickness and applied voltage, respectively. This theory states that when the filament radius is smaller than the nucleation barrier R_0, then filament will rupture spontaneously, resulting in threshold switching. For the case when filament continues to grow laterally resulting in a thick and stable filament, exceeding R_0, then memory switching is observed (Figure 1.15b). For the switching behavior of aforementioned metal-filament type selector, delay-time, τ_d, as per the given square pulse, can be represented by following equation.[58]

$$\tau_d = \tau_0 exp\left(\frac{W(E)}{kT}\right) = \tau_0 exp\left(\frac{W_0 \alpha^{3/2} E_0 d}{kTV}\right)$$

In the above equation, τ_d stands for the point of abrupt increase in the output current in response to the input voltage, *k*–Boltzmann constant, *T*–temperature (°K). Figure 1.15a shows the schematic and qualitative description of the field-induced nucleation theory.

Wang *et al.*[60] has reported a summary of the various selector structures and materials investigated over time, that demonstrated metal-filament type threshold switching behavior. Metal-filament type TS selectors have garnered a lot of attention for their figure-of-merit over its other competitors, such as extreme-low off current (<1 pA), ultra-steep subthreshold swing (<10 mV/decade), high ON-state current density (>1 MA/cm^2), high selectivity ratio (> 10^7), and fast switching (turn-on and dissolution) speed (< 100 ns). During the switching operation, under continuous formation and rupturing of the CF during the application and removal of external bias,

there is no electrical breakdown of switching layer, thus it helps in maintaining a low leakage current under DC/AC cycling.[25]

However, metal-filament type selectors suffer from two major drawbacks of (a) large switching parameter variability, specifically threshold voltage (V_{th}) variances, and (b) lousy cycling endurance (Figure 1.16a).[61] Device-to-device (d2d) and cycle-to-cycle (c2c) ΔV_{th} shifts are some inevitable issues that are primarily observed in various CBRAM-type devices along with metal-filament type selector devices. These switching parameter variabilities are ascribed to the non-uniform SL composition along its thickness, and the surface roughness at the cathode interface, which drives the metallization process on energetically favorable sites rather than allowing uniform deposition on the cathodic surface.[28] Also, the metallic filament formation by

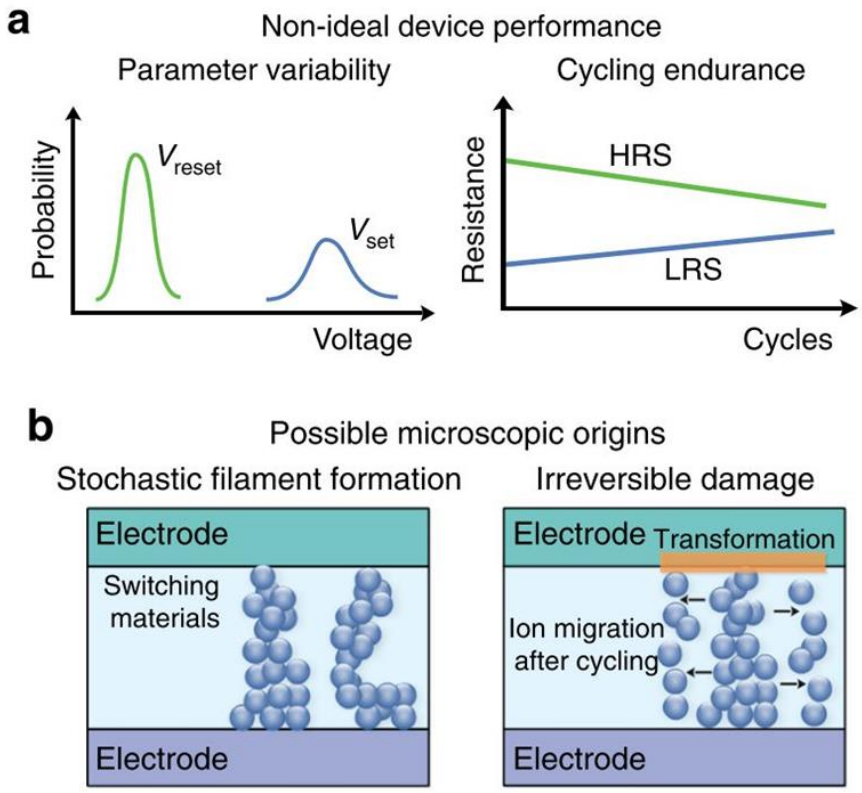

Figure 1.14. (a) Metal-filament type selector devices common drawback. (b) Possible microscopic origins for the stochasticity.

the active reservoir electrode is a stochastic process, giving rise to intrinsic variabilities (Figure 1.16b).[26,61]

As previously discussed, (Figures 1.12, 1.13, and 1.15), TS behavior fades away and the devices go into memory switching mode when there is laterally thick and stable filament formation. This ultimately leads to permanent filament formation, where the filament does not rupture when the applied voltage bias is removed. This is referred to as stuck-ON state (OFF-failure) *i.e.*, continuous low-resistance state (LRS). Additionally, the uncatered supply of Ag metal ions to the switching layer could also contribute to unrestricted radial filament growth. In conclusion, the radially thick and stable filament becomes the bottleneck for endurance operation. So further research to rectify the shortcomings such as switching device uniformity, reliability, and endurance is mandatory.

1.6 Dissertation Outline

CHAPTER 1 provides background information on the benefits and challenges of realizing a 3D X-point memory architecture, emerging non-volatile memories (NVMs) proposed for X-point arrays, various selector devices investigate till date, and specifically Ag-based metal-filament type selector devices. It has been discussed that how Ag-based metal-filament type selectors hold the potential to satisfy ideal selector requirements, as compared to its competitors, but still suffer from variability and endurance issues. This dissertation is focused on developing a reliable and robust threshold switching selection device with enhanced performance, having reduced variances and improved cycling endurance and reproducibility, whilst maintaining all other figure-of-merits.

CHAPTER 2 provides a description of the experimental procedures, thin film deposition methods/techniques, electrical and material characterizations, performed in this dissertation.

CHAPTER 3 discusses the "super-cycle ALD" technique for selector device fabrication. Alternating ZnO ALD and Ag metal ALD were employed in this method for delta/layered doping ZnO with Ag. Our first fabrication approach of ECD has also been briefly discussed here.

CHAPTER 4 focusses on the final fabrication technique evaluated in this dissertation for selector fabrication *i.e.*, RF magnetron co-sputtering. Although ECD and ALD processes gave reasonable selector device performance but the shortcomings of both the ECD and ALD processes, demanded another method to be investigated for fabricating TS selector devices. Co-sputtering process confirmed outstanding TS behavior with remarkable switching parameters which were found to exceed our targeted results discussed in Chapter 1.

All the findings discussed in Chapters 3 – 4 collectively aims at improving the selector device variances and cycling endurance issues realized in conventional active electrode-based structure by exploiting a novel doping-based approach. Though this dissertation mentions three different deposition techniques, but all the process outcomes can be conclusively summarized as; doping the ZnO switching layer curtails the accessible influx of Ag ions to selector medium, and crystalline ZnO growth in preferred (002) orientation favors anisotropic Ag ion diffusion in the wurtzite ZnO matrix, both resulting in parameter variance and device endurance augmentation. Results and shortcomings of every deposition method have also been examined.

CHAPTER 5 concludes this dissertation and provides insights to the potential ideas that could bring innovation in selector implementation in a 3D X-point array such as ferroelectric X-point array (1F1S) for future neuromorphic computing studies.

Furthermore, I have submitted many original research papers in various journals, on the discussed deposition techniques during the course of writing my dissertation and will be reflected accordingly in the respective chapters.

CHAPTER 2

EXPERIMENTAL PROCEDURE

2.1 Deposition Techniques

2.1.1 Electrochemical Deposition (ECD)

Thin films play a crucial role for electrochemical studies and their applications. The thin film (<1 µm) behavior typically relies on the electrode surface morphology. There are many prevalent deposition techniques for thin film deposition for instance chemical vapor deposition (CVD),[62,63] chemical bath deposition,[64,65] electrochemical deposition (ECD)[66] etc. Amongst them, ECD process is quite popular as it is a fairly cost effective, easy, and efficient method for fabricating a variety of thin films. ECD can be used for depositing metals, metal oxides/alloys and

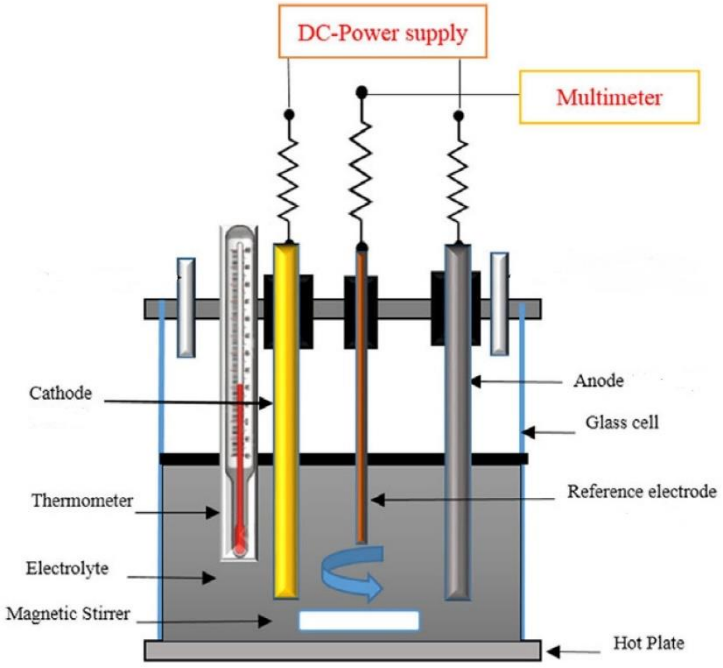

Figure 2.1. Schematic for three-electrode based ECD setup.

other hybrid materials.[67–70] The basic process of electrochemical deposition involves the migration of metallic ions in electrolytic solution, towards the cathode, when an external electric field is applied. There is an occurrence of a redox reaction where ions either accept or lose an electron and get deposited on cathode or anode, respectively. Figure 2.1 shows the schematic setup for small scale electrochemical deposition.[71]

ECD process can be carried out with a two-electrode system or a three-electrode system. Two-electrode system proves advantageous in terms of process simplification with excluding any possible chances of contamination from the reference electrode (RE). However, the drawback of two-electrode ECD setup lies in fluctuating potential between the counter electrode (CE) and, working electrode (WE), which intensifies with film thickness growth during the deposition process. On contrary, the three-electrode system is quite immune to fluctuations in the potential as it measures the WE and RE potential difference, while measuring the current flow between CE and WE, thus minimizing fluctuations during the deposition process. There are many other factors that can adversely influence the ECD process such as solute/solvent purity, deposition temperature, current density, pH of the electrolyte, deposition time etc.[72] Although, ECD has a strong advantage of fabricating doped films with extreme control over the dopant concentration, but the downside of the process lies in unwanted extrinsic doping by electrodes, fluctuating current density during deposition process, non-uniform and non-conformal film growth.[72]

We previously reported the ECD process for verifying our proof-of-concept of doping the switching layer in threshold switching selector instead of implementing an active reservoir electrode. Kim *et al.*,[47] has discussed in detail the volatile switching behavior per doping for the

metal-filament type TS selector devices fabricated *via* ECD process. Figure 2.2 shows the ECD setup used by our group already discussed in detail elsewhere.[47]

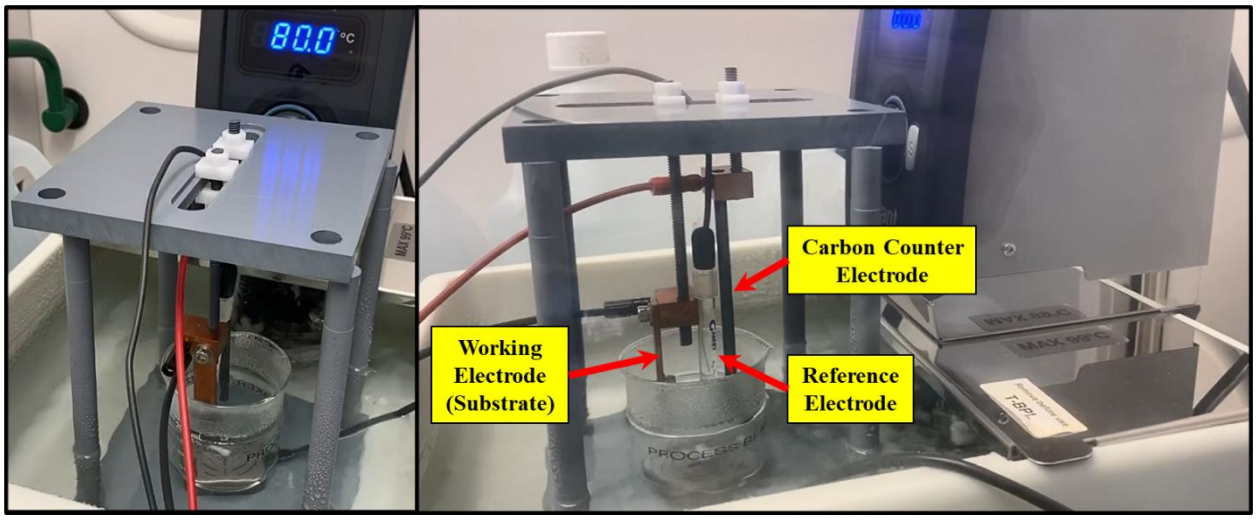

Figure 2.2. A three-electrode ECD process setup used in this work.

2.1.2 Atomic Layer Deposition (ALD)

Atomic Layer Deposition, which falls under the chemical vapor deposition category, is a vapor phase technique used extensively for fabricating thin films. ALD offers many potential advantages over other existing deposition methods because of its excellent control over film conformality, thickness and composition.[73] Figure 2.3 illustrates a general ALD process.[74] The deposition process comprise of sequential alternating gaseous chemical precursor pulses reacting with the given substrate. The entire material synthesis process is split into 'half-reactions' which involves individual gas-surface reactions. Every half-reaction process includes pulsing of the precursor into the vacuum chamber for a definite time allowing ample time for the precursor to completely react with the substrate through a self-limiting reaction. Any unreacted precursor or

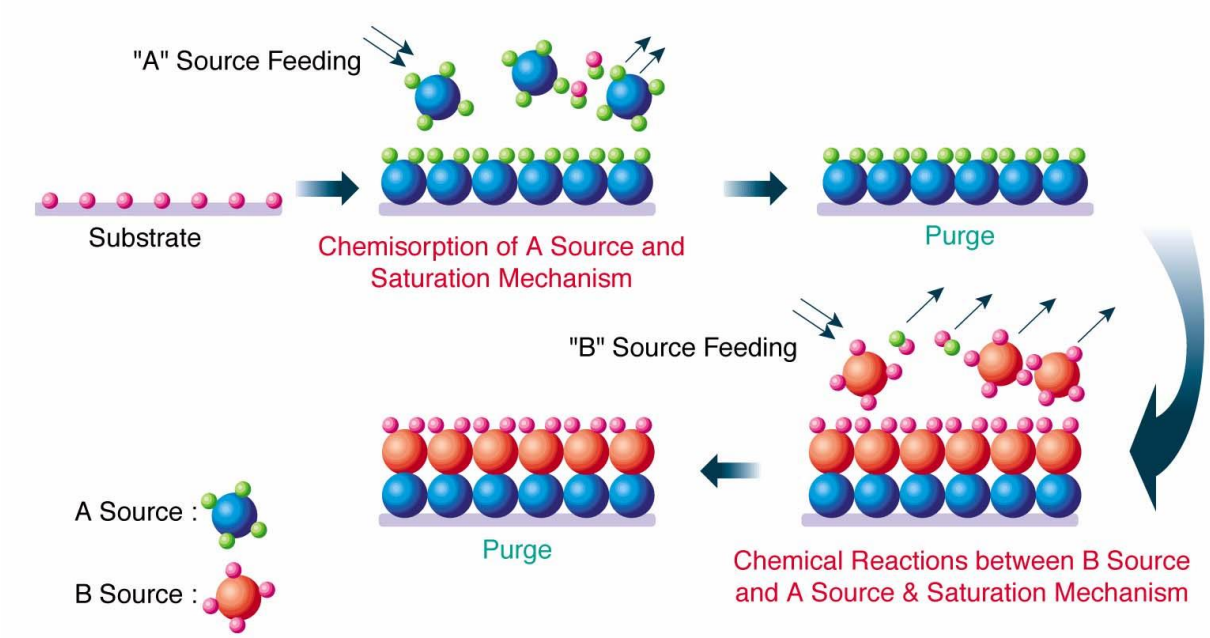

Figure 2.3. Schematic illustration of one full cycle of ALD deposition process.

by-products of the reaction are then purged out by flowing an inert Ar or N_2 carrier gas. Purge process is then followed by a second precursor pulse of the counter-reactant again trailed immediately by purging, thus creating a monolayer of the desired material. This whole process is then repeated continuously until the desired thickness level is attained. Therefore, ALD process can offer atomic thickness controllability by tuning the number of deposition cycles. This is an extremely desirable feature for scaling down the transistor device dimensions for highly complex device architectures.[75,76]

In this dissertation, the ALD deposition technique was investigated to elucidate the fundamental understanding of polycrystalline ZnO material properties as a switching layer for TS selectors. In the design of experiments, ALD ZnO along with Ag doping has been evaluated for its operation as a volatile switching layer. The Zn precursor – Diethylzinc (DEZ), Ag precursor – Silver hexafluoropentanedionate trimethylphosphine complex, $C_8H_{11}AgF_6O_2P$, high-

concentration ozone (O_3, 400 g/m^3), and deionized water (H_2O) were used in the discussed ALD process. The carrier gas and the purge gas functionalities were both performed by high purity (99.9999%) BIP grade inert gas – Ar or N_2. The elaborate details on experimental process of TS selectors fabricated *via* ALD are discussed in CHAPTER 3.

Figure 2.4 displays the Cambridge Nanotech/Ultratech Savannah S100 (CNT) crossflow ALD reactor used for thin film deposition in this dissertation. CNT tool was used to deposit TiO_2 layers discussed at CHAPTER 4. Figure 2.5 displays the NCD D100 crossflow ALD reactor installed in our laboratory which is equipped with (hfac)Ag(PMe_3), DEZ, O_3, and H_2O. NCD D100

Figure 2.4. Cambridge Nanotech/Ultratech Savannah S100 (CNT) ALD reactor.

ALD reactor tool was used for depositing Ag doped O_3-based ZnO volatile switching layer by 'supercycle' ALD method discussed at CHAPTER 4. The aforementioned ALD reactors employed in this thesis were decked with an ozone generator catered by Toshiba-Mitsubishi-Electric Industrial Systems Corporation.

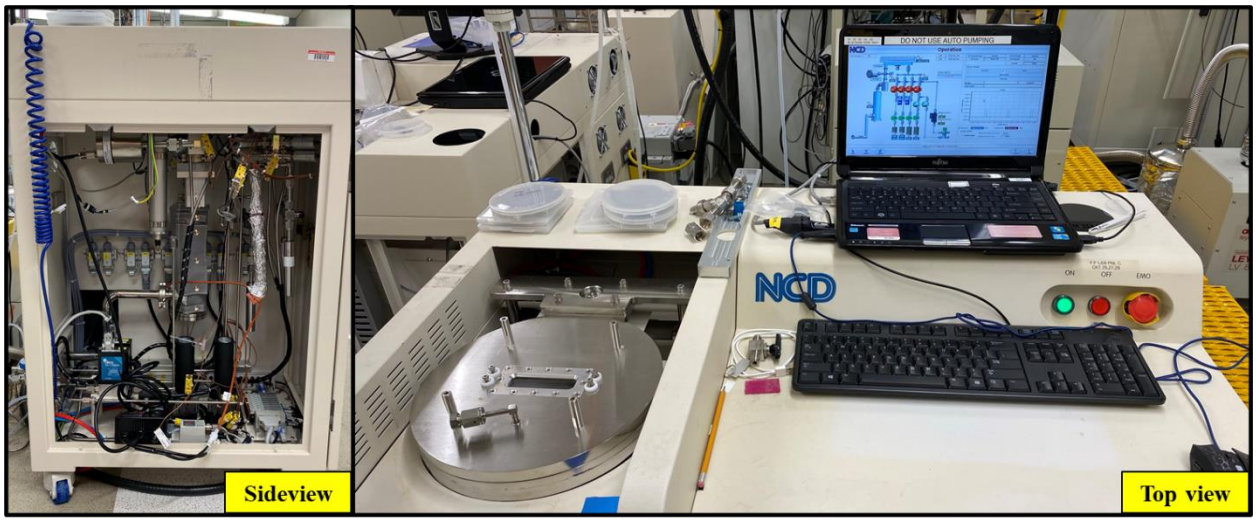

Figure 2.5. NCD D100 ALD reactor equipped with ZnO and AgOx, employed for 'super-cycle' ALD process.

2.1.3 Sputter Deposition

Sputter deposition method is an extensively used physical vapor deposition (PVD) technique presenting several advantages over other prevalent techniques like molecular beam epitaxy or pulsed laser deposition when large-scale films need to be deposited. PVD technique allows atom by atom coating growth on the substrate by atomization of material from a solid source, called as target.[77] It enables to deposit extremely high-quality epitaxial thin films and complex oxide materials superlattices at a significantly cost effective rate when compared to other methods.[78,79] The overall adaptability and flexibility of the PVD processes led to the development of varied processes and thus several variants have originated over a period of time as shown in the

Figure 2.6.[77] In this dissertation, sputtering via only radio frequency and direct current methods have been investigated, discussed in detail at CHAPTER 4.

The sputtering process depends on the generation of plasma through electrical discharge

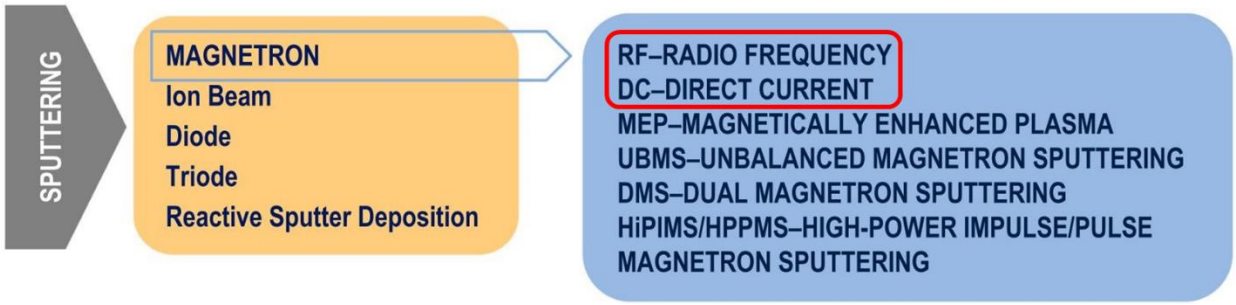

Figure 2.6. Physical vapor deposition methods segmentation for various coating techniques.

and acceleration of energetic ions (*e.g.*, Ar^+) towards the desired target to be deposited (ZnO, Ag or Ag-doped ZnO, in this work) which is biased as cathode terminal in an electrically grounded vacuum chamber. Figure 2.7 shows an illustration of sputter/co-sputter deposition setup. The

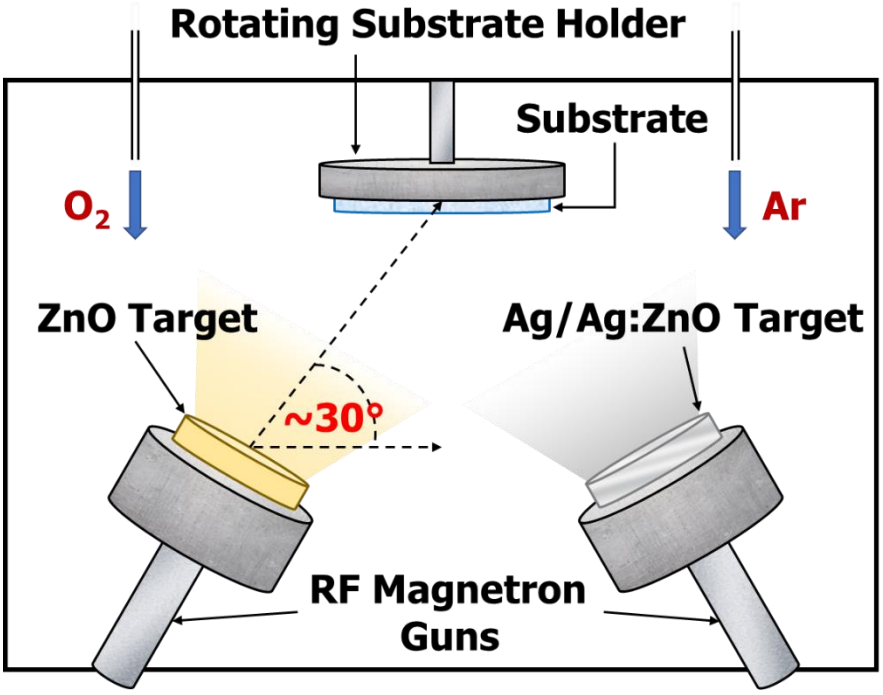

Figure 2.7. Diagram of the sputter/co-sputter deposition process.

accelerated high energy ions are bombarded on the target surface causing sequential collisions with the exposed atoms of the target. These continuous collisions provide outward momentum to the atoms thus ejecting them from the surface. These ejected atoms finally get deposited on substrate surface creating a thin film. Now the utilization of magnetron sputtering greatly enhances the process yield by confining the charged particles of plasma closer to the target surface. The magnetron process is based on a combined principle of exploiting the effect of electric field working in the sputter process and magnetic field acting behind the target, which together helps in trapping electrons in helical trap paths surrounding the vicinity of the target. The sputter process sequence involves – ramp up, etching/conditioning, coating, and ramp downstage, shown in Figure 2.8.[77]

In this dissertation, sputter/co-sputter deposition techniques have been employed to fabricate volatile switching layer for the metal-filament type TS selector devices discussed at CHAPTER 4. ZnO, Ag and Ag-doped ZnO (Ag:ZnO) targets have been individually sputtered or

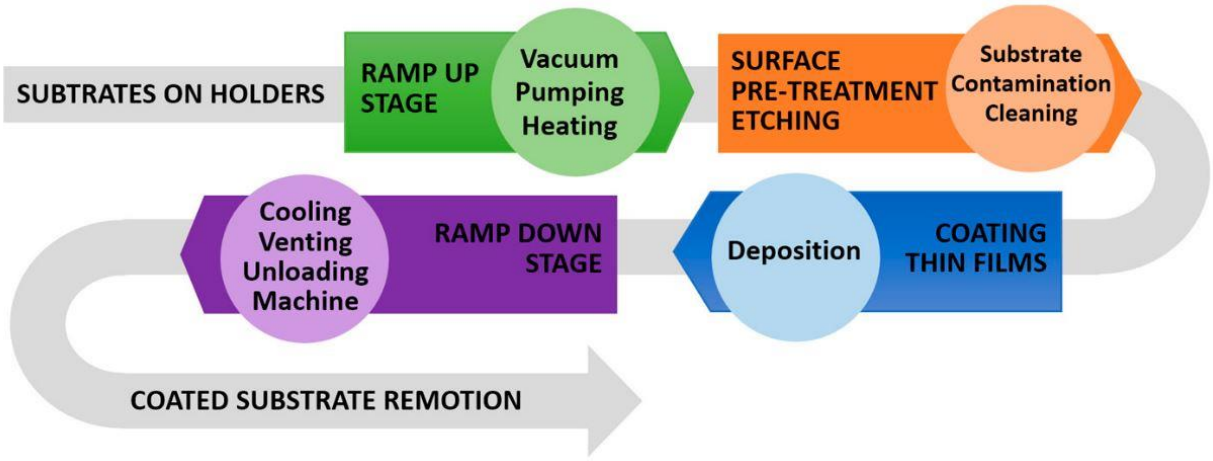

Figure 2.6. Schematic process flow for the sputtering deposition.

co-sputtered as per the design of experiment to deposit ZnO or Ag-doped ZnO thin films. Figure 2.9 displays the ATC Orion sputter deposition system (AJA International) used in this work.

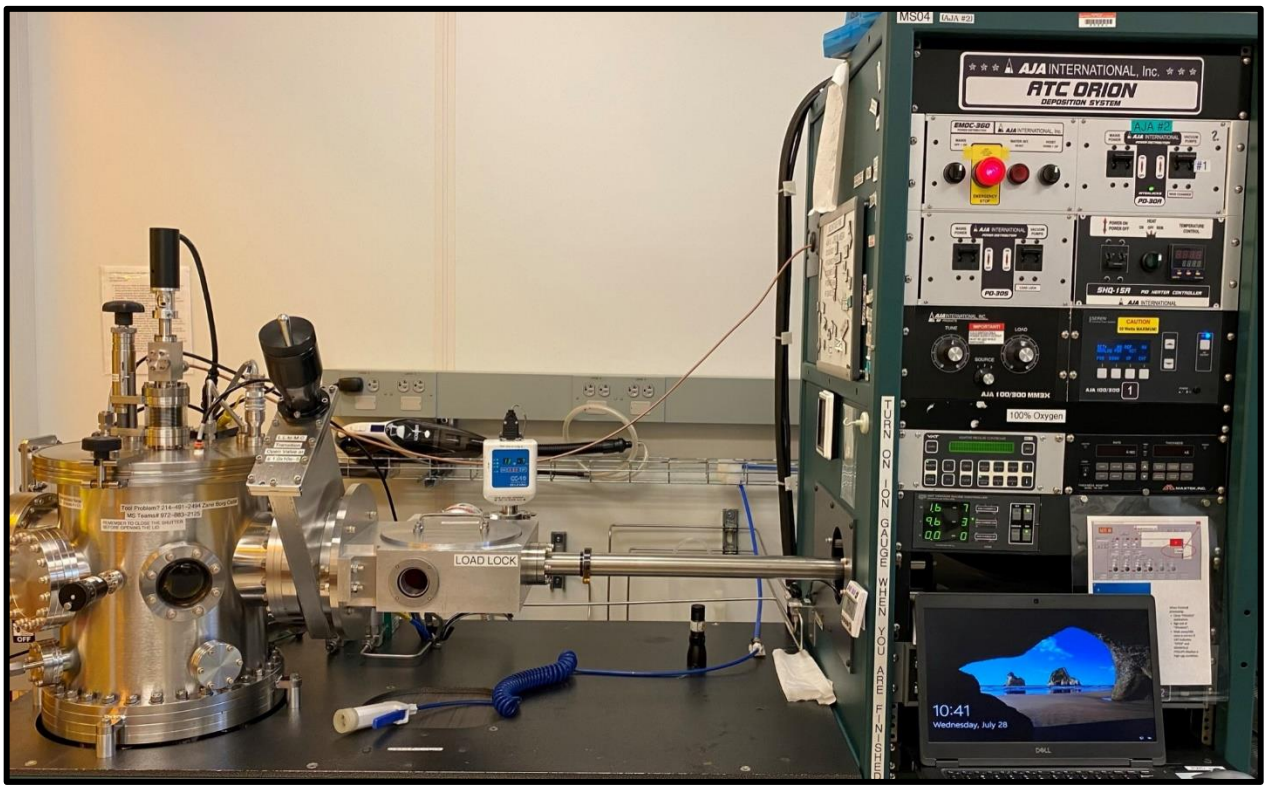

Figure 2.7. ATC Orion Magnetron sputter deposition system by AJA International.

2.2 Electron Beam Lithography

Electron beam lithography, EBL, is a technique of forging nanoscale patterns in integrated circuits. EBL process involves transferring an intended pattern onto the substrate surface by first scanning a thin organic film layer *i.e.*, resist, by exposure from a narrow and precisely focused electron beam and then removal of the particular resist regions- exposed/non-exposed, in a developing solvent.[80,81] Figure 2.10 shows an illustrative diagram of the EBL process,[82] where Figure 2.10b displays the top view of fabricated nanohole structure discussed in CHAPTER 4.

EBL tools comprise of three main parts: electron gun, vacuum, and control system. A filament tip emits electrons which are attracted by an anode terminal. The spot size diameter of

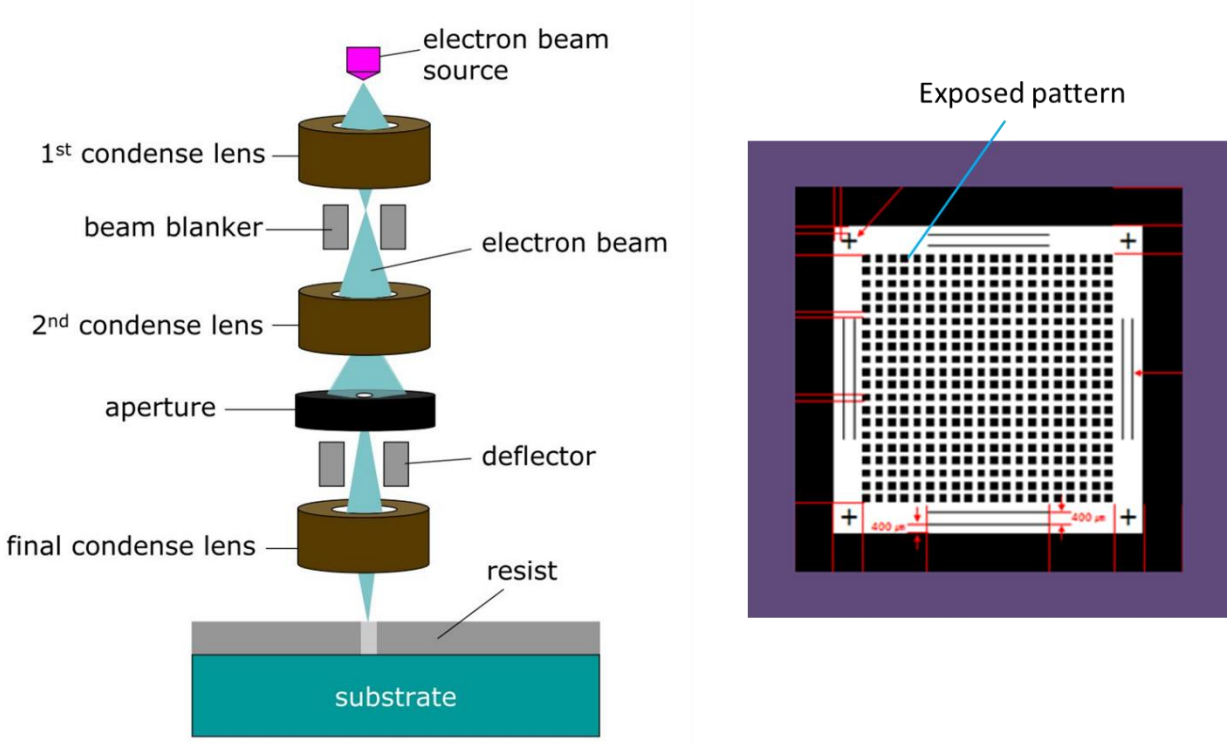

Figure 2.8. An illustration diagram of the electron beam lithography technique. A focused e-beam is projected on the organic resist layer for creating a pattern by dot-by-dot exposure: (a) EBL setup- side view; (b) top view of the nanohole selector structure used in this dissertation.

the beam is defined by focusing the emitted electrons using electromagnetic lenses. The vacuum system plays role in cutting any outer interference by isolating the beam. The final pattern is then created using a computer aided software. Figure 2.11 shows the image of the EBL system (Raith 150^{TWO}) used in this work.

Figure 2.9. Raith 150TWO e-beam lithography system used in this work.

2.3 Electrical Characterization Methods and Tools

2.3.1 Four-point Probe

The four-point probe is generally utilized for measuring surface conductivity of nanoscale thin films and any semiconductor material. It can measure either of the bulk or thin films, depending on the measuring tip structure using a different mathematical expression. The usual four-point setup comprise of four equally spaced tungsten (W) metal tips with known radius, though other probe spacing configurations are also utilized in some cases. It was first used in 1915 by Wenner [83] for avoiding contact resistance. The four-point probe has an auto-mechanical stage that contains the four metal tips which move up and down while measuring. The two outer metal probes deliver current supplied by a high impedance current source, while a voltmeter is used to

(a) (b)

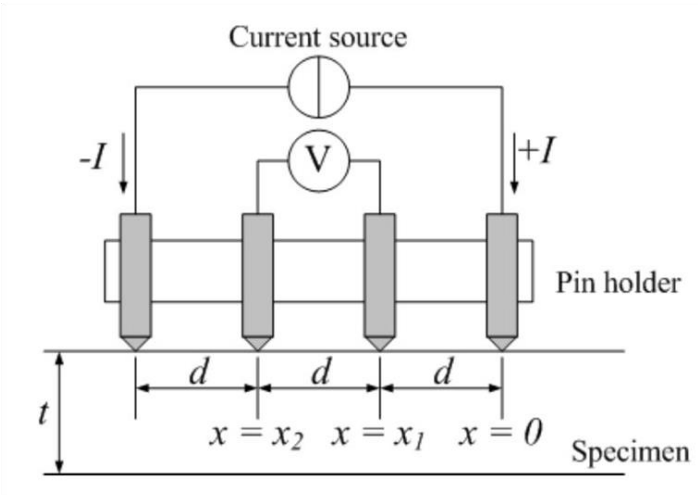

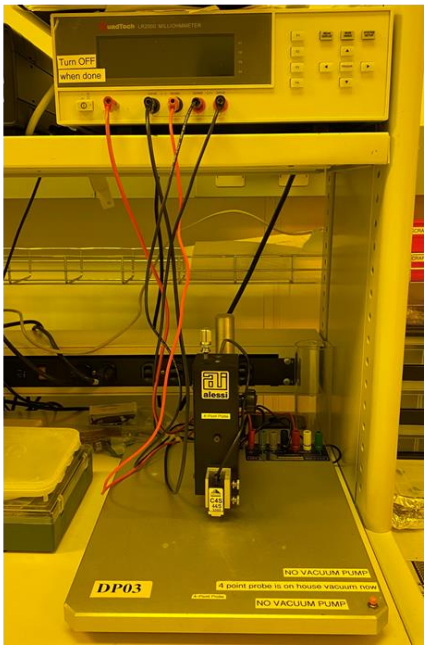

Figure 2.10. (a) Schematic illustration of the four-point probe system, (b) An image of Alessi four-point system.

measure the voltage across the two inner metal probes for determining the resistivity of the wafer under test, as shown in Figure 2.12a [84]. The resistivity measured by a four-point probe, ρ, can be expressed by

$$\rho = 2\pi s\frac{V}{I}$$

Figure 2.12b displays the Alessi four-point probe system employed in this dissertation to determine ZnO thin film conductivity. The Alessi tool uses Cascade C4S probe head that has tungsten carbide probe tips with 1mm of equal spacing between them.

2.3.2 Cascade Probe Station

The cascade probe station is generally used for performing device characterization measurements. All the devices that need to be protected from electromagnetic interference and light, can be conveniently measured using the cascade probe station as it provides shielding to the

chuck from above mentioned effects. This system allows fA-level current measurements as the chuck here is electrically guarded.

Figure 2.13 shows an image of the Cascade probe station integrated with semiconductor parameter

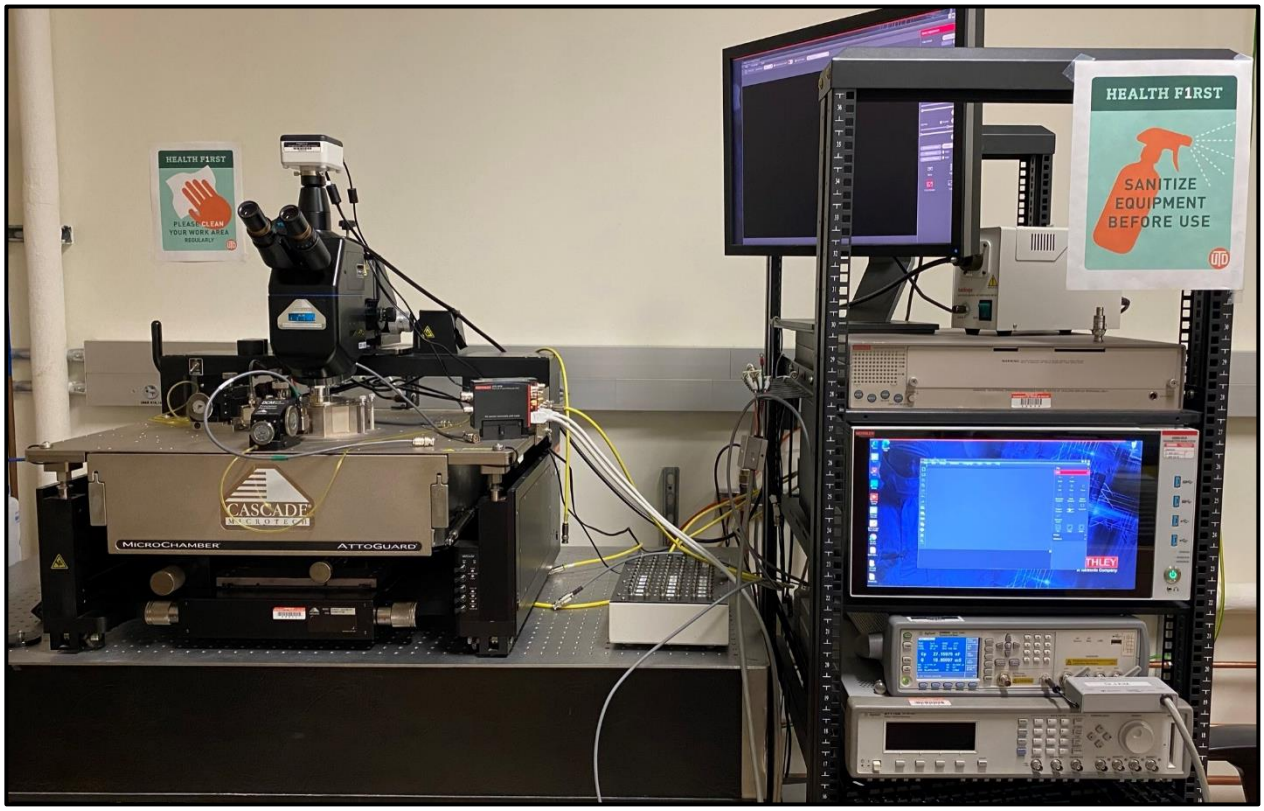

Figure 2.11. Cascade probe station decked with Keithley 4200 semiconductor parameter analyzer, and HP 4284 LCR in Prof. Chadwin Young's eCOMETS lab.

analyzer – Keithley 4200and HP 4284 LCR meter, extensively used in this dissertation for deriving current-voltage characteristics (*I*-*V*) of selector devices fabricated via various fabrication methods. The selector devices were clamped on the chuck, held by vacuum, and measurements were performed in dark environment. All the measurements discussed in this dissertation were acquired at room temperature, though the tool had the capability to be heated up to 200 °C chuck temperature for any temperature-dependent measurements.

2.3.3 Semiconductor Parameter Analyzer

The semiconductor (or device) parameter analyzer is a testing tool utilized for performing high accuracy electrical measurements like capacitance–voltage (*CV*), capacitance–time (*C-t*), capacitance–frequency (*C-f*), and current–voltage (*IV*) measurements. Figure 2.14 shows an exemplary DC sweep cycle diagram. The entire DC sweep has been divided into four parts for understanding purposes. First, at the beginning of each sweep, a hold time (HT) is added for measurement stabilization, followed by a pre-programmed default delay. This delay factor can either be limited auto or best fixed, depending on the measurement requirement, which is typically the time that SMU waits before initializing next measurement whenever a voltage is applied to device under test (DUT). Next component is the sweep delay (SD) which is an extra time added before the actual measurement begins, and finally the measurement time (MT), which is the time taken for measuring current in the given DUT. In this work, the measurement setup has been frequently varied as per experimental design requirements *e.g.*, measurements at fast integration time were performed whenever hundreds of DC-*IV* cycles were required to be swept and recorded whereas, slow integration time measurements were conducted when the priority was to record ultra-low leakage currents.

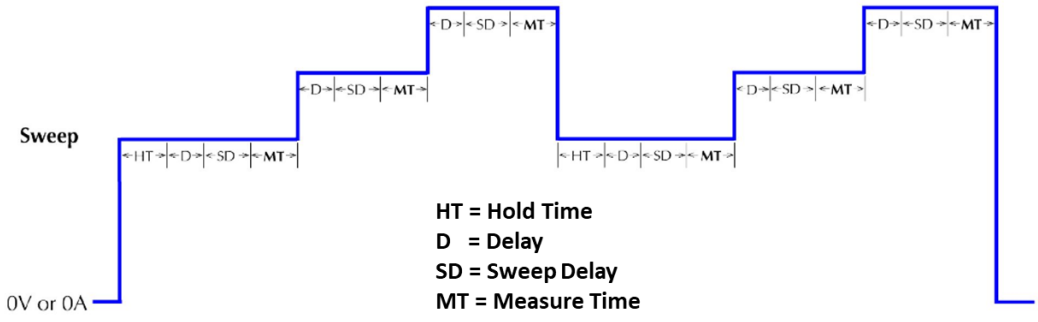

Figure 2.12. An exemplary DC sweep sequence.

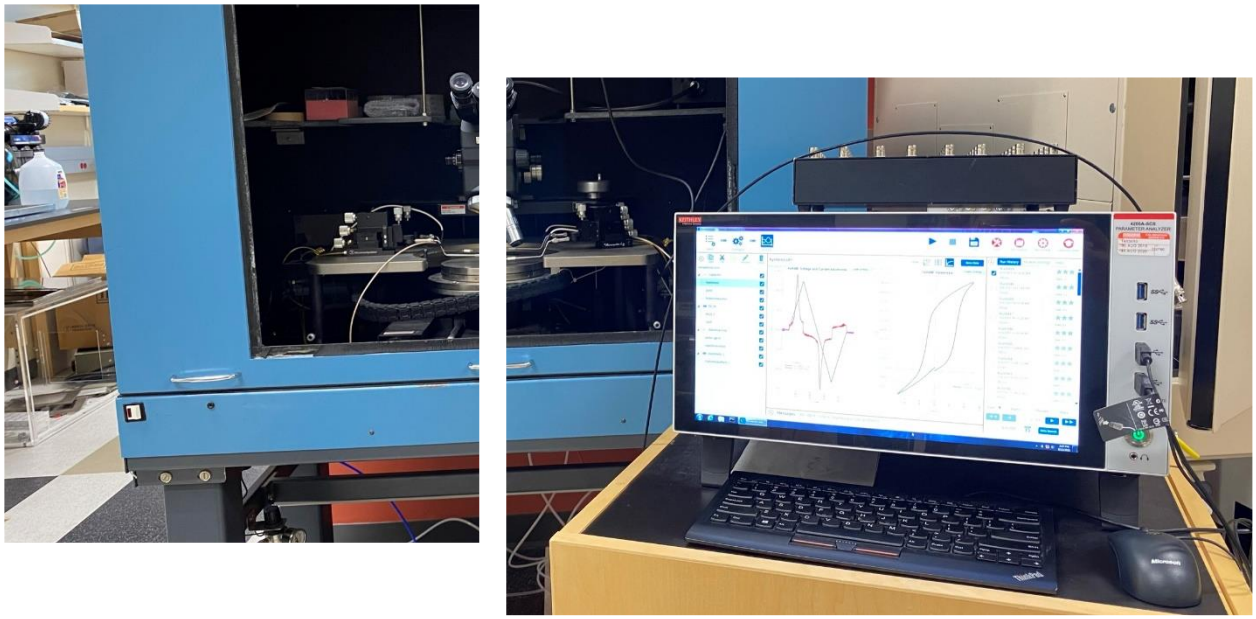

Figure 2.13. Semiconductor parameter analyzer – Keithley 4200A-SCS, connected to a probe station in Prof. J. Kim's lab.

Figure 2.15 displays the Keithley 4200A-SCS semiconductor parameter analyzer which was used in this dissertation additionally to the Cascade probe station discussed in previous section. Also, AC transient measurements were performed using the same setup but utilizing LabView program, designed by Mr. Mohamed Abrar Sait.

2.4 Material Characterization Methods and Tools

2.4.1 X-ray Diffraction (XRD) Analysis

Max von Laue discovered in 1912 the phenomenon of X-ray diffraction using crystalline materials. In 1915, Lawrence Bragg and his father explained the X-ray diffraction process. XRD now has become a very common method for studying crystallographic structures and atomic spacings. The basic principle of XRD exploits the advantage of constructive interference of the monochromatic X-rays after suffering diffractions when incident on the crystalline sample. X-rays

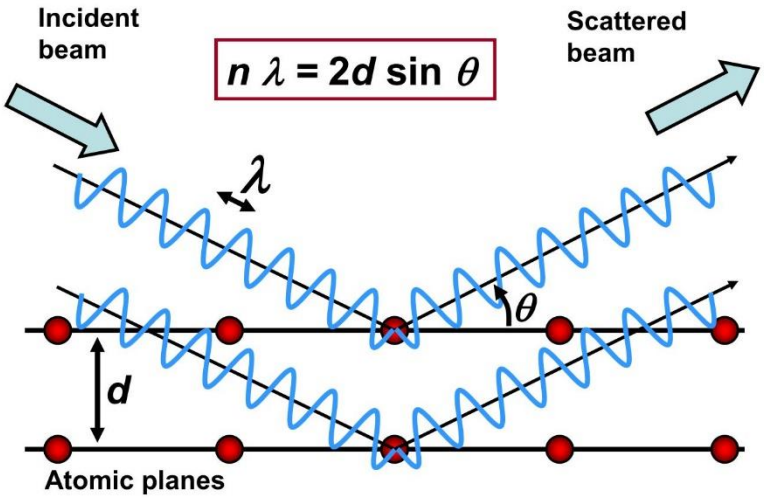

Figure 2.14. A schematic illustration of X-ray Diffraction principle.

are an appropriate choice for this study as their wavelength is typically of the same magnitude order as the crystal spacing. When X-rays are incident on the sample, it produces constructive interference if it meets the Bragg's Law condition of $n\lambda=2d\sin\theta$ (Figure 2.16) [85]. The diffracted X-rays are then spotted by the sensing detector, processed, and finally counted to tell the intensity. The captured diffraction peaks are then converted to d-spacings, compared with reference patterns, and interpreted to identify the crystal structure of given specimen.

The conventional scanning mode in XRD is out-of-plane $\theta/2\theta$ but if the crystal sample has ultrathin thickness of <20 nm, $\theta/2\theta$ scanning mode fails to provide any meaningful data due to weak specimen signal as compared to stronger substrate signal, thereby making it difficult to acquire crystalline diffraction peaks. [86] To resolve this issue, grazing incidence X-ray diffraction (GIXRD, 2θ scanning mode) is employed to enhance the surface sensitivity by avoiding intense signals from the substrate. Here the fixed angle is usually set a little higher than total reflection's critical angle in order for the substrate to show total external reflection.[87]

Figure 2.15. Rigaku SmartLab X-ray diffractometer system.

Figure 2.17 displays the Rigaku SmartLab X-ray diffractometer system used in this dissertation, which is decked with 0.1542 nm wavelength Cu kα X-ray source. In this work, scanning modes of *2θ* and *θ/2θ* have been exploited to understand crystal structure and phase of the nano-polycrystalline ZnO.

2.4.2 X-ray Photoelectron Spectroscopy (XPS)

X-ray photoelectron spectroscopy, XPS, is a computable method employed for determining the surface-sensitive composition of elements in a material as well as can identify the binding states of the constituent elements, by exploiting the principle of photoelectric effect. The usual probing depth of XPS is 10 nm and utilizes photoelectrons possessing kinetic energy (KE) in 300–1500 eV range for surface analysis. When photoelectrons are emitted from the surface material,

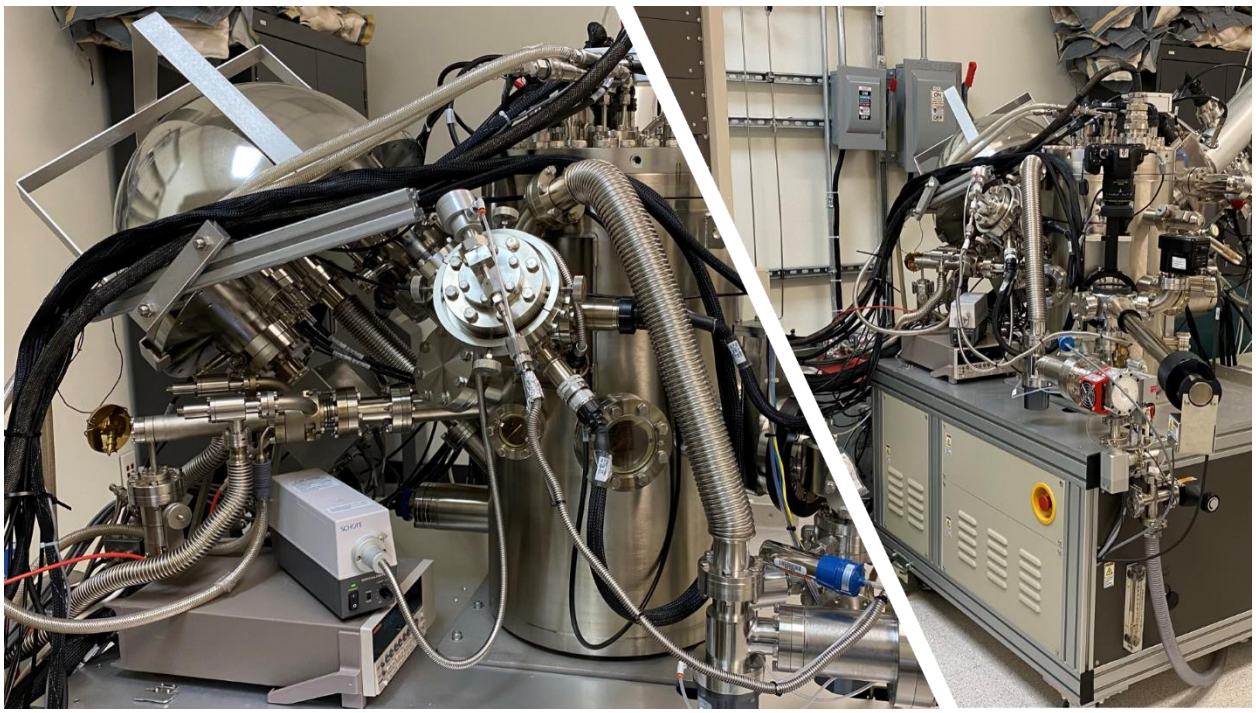

Figure 2.16. Versa Probe II scanning X-ray Photoelectron Spectroscopy system.

their energy corresponds to a specific element characteristic. The expression for calculating the binding energy (BE) of ejected electrons from KE is given by,

$$BE = h\nu - KE - \Phi_s$$

where BE indicates binding energy of core electrons, $h\nu$ – photon energy of X-ray, KE – ejected photoelectrons kinetic energy, and Φ_s – represents the work function.

Figure 2.18 shows the Versa Probe II scanning XPS system used in this work, which is decked with an Al kα monochromatic X-ray source having 1486.6 eV photon energy. In this dissertation, XPS analysis was extensively performed for determining elemental composition, oxidation states and binding energies of fabricated Ag-doped ZnO thin films for evaluating doping concentrations as per the experimental design as well as the film's overall stoichiometry for varied deposition conditions.

2.4.3 Atomic Force Microscopy (AFM)

Atomic force microscopy (AFM)[88–90] is a distinguished kind of the scanning probe microscopy having a nanometer order resolution. AFM tool acquires data by measuring the force sensed by probe atoms and the ones in sample. This is performed by a cantilever having a sharp tip made typically of silicon or silicon nitride, which picks any deflections and convert them into data. As the topography of the given specimen changes, the interaction between the cantilever and specimen surface also changes, thus producing deflections which are mapped as a topographic image. Figure 2.19a shows the schematic diagram of AFM working principle.[91] AFM can be used in two different image modes – dynamic (tapping/non-contact) and static (contact) as per user requirement. In general, dynamic mode has advantages over the static mode, due to its capability to scan the samples more gently. This involves probe tip oscillations at a fixed frequency where the oscillation amplitude changes accordingly with the interactions between cantilever tip and the material surface.

Figure 2.19b displays the Oxford Asylum Research Jupiter XR Atomic Force Microscope system used in this work. Prior to this tool, Veeco Dimension V SPM AFM system had been used

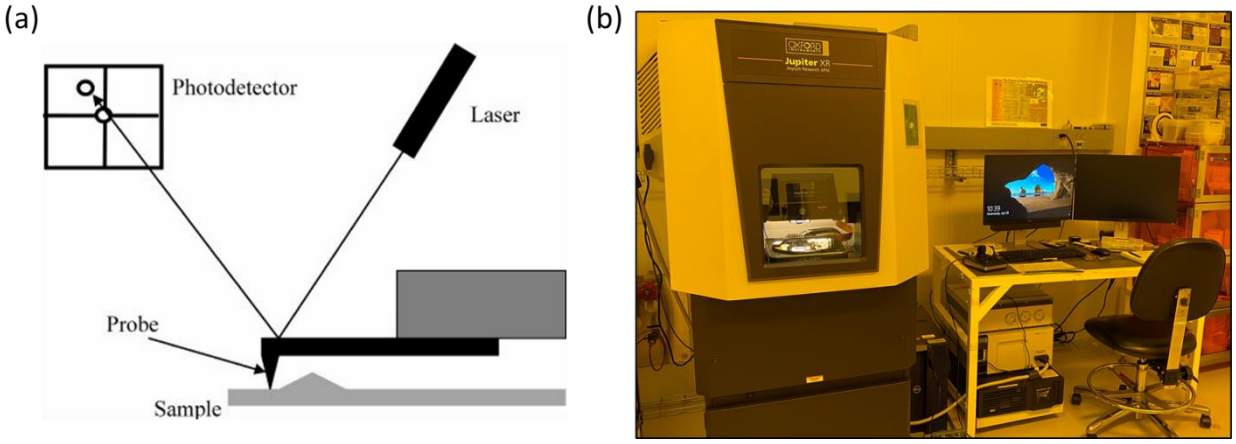

Figure 2.17. (a) Schematic for AFM working principle, (b) An image of Oxford Asylum Research Jupiter XR Atomic Force Microscope system.

for obtaining tapping mode images. The measurements were performed with tool housing on as the AFM image quality can be degraded due to ambient noise as the tool is quite sensitive to any environmental disturbance. In this dissertation, AFM has repeatedly been utilized for confirming the crystallinity of doped/undoped ZnO thin films as well as to estimate the surface average roughness (R_a) to examine any surface damages while deposition and Gwyddion software was used for image analysis.

2.4.4 Scanning Electron Microscopy (SEM)

Scanning electron microscope, SEM, is a prominent electron microscopy subclass utilized for obtaining a high-quality detailed image of a specimen with spatial resolution. A high-energy

Figure 2.18. Zeiss SUPRA 40 scanning electron microscope.

beam is incident on the sample in SEM, which provides information on surface morphology, grain/crystallographic orientation, composition of a material. SEM primarily detects two types of electrons – a) backscattered electrons (BSE), and b) secondary electrons (SE), though X-rays could also be produced. BSE are the ones reflected back following an elastic interaction whereas SE originate from inelastic interaction, between the sample and electron beam. SE originate from superficial surface while BSE come from broad regions in the specimen. SEM can generate 3D surface maps with 50,000x magnification offering extremely-high lateral resolution for >10 nm range, and ability to do energy dispersive X-ray (EDAX) analysis.

Figure 2.20 shows Zeiss SUPRA 40 SEM tool capable of scanning images with 1-2 nm resolution for imaging. In this dissertation, SEM images were captured to image cross-sectional Ag-doped ZnO polycrystalline layer structure as well as to confirm SL crystallinity. Moreover, EDAX analysis feature offered in the SEM tool was also used for determining ZnO film's chemical composition/detection limits to estimate Ag doping levels.

2.4.5 Inductively coupled plasma mass spectrometry (ICP-MS)

Inductively coupled plasma mass spectrometry (ICP-MS)[92] is an analysis method for measuring the elemental trace levels in a specimen. In this technique inductively coupled plasma is used for ionizing the sample, atomizing it, then creating atomic and polyatomic ions, finally sensed by the detector. This technique can detect metals/non-metals in a liquid sample (typically nitric acid), even if present in extremely low concentrations. It can also identify the isotopes of an element thus offering very precise results with great speed and sensitivity. In ICP-MS method, a quadrupole extracts ions from the plasma using a series of cones on the basis of ratio of mass-to-charge of the detected ions. A reference material (standard) is used for calibration first, which is

utilized as a reference scale to estimate the concentration of sample of interest. ICP-MS can be used to determine elemental composition in 7-250 atomic mass range.

Figure 2.21 shows an image of the Perkin-Elmer Sciex Elan 6100 DRC inductively coupled plasma mass spectrometer (ICP-MS) tool, used in this dissertation. We performed ICP-MS analysis to estimate the Ag doping levels in the Ag-doped ZnO thin films when the doping concentration was so low that it could not be determined with either XPS or EDAX analysis. The tool access was provided by Professor Gabriele Meloni from the Chemistry and Biochemistry department and Ms. Rhiza L. Villones aided with the measurements.

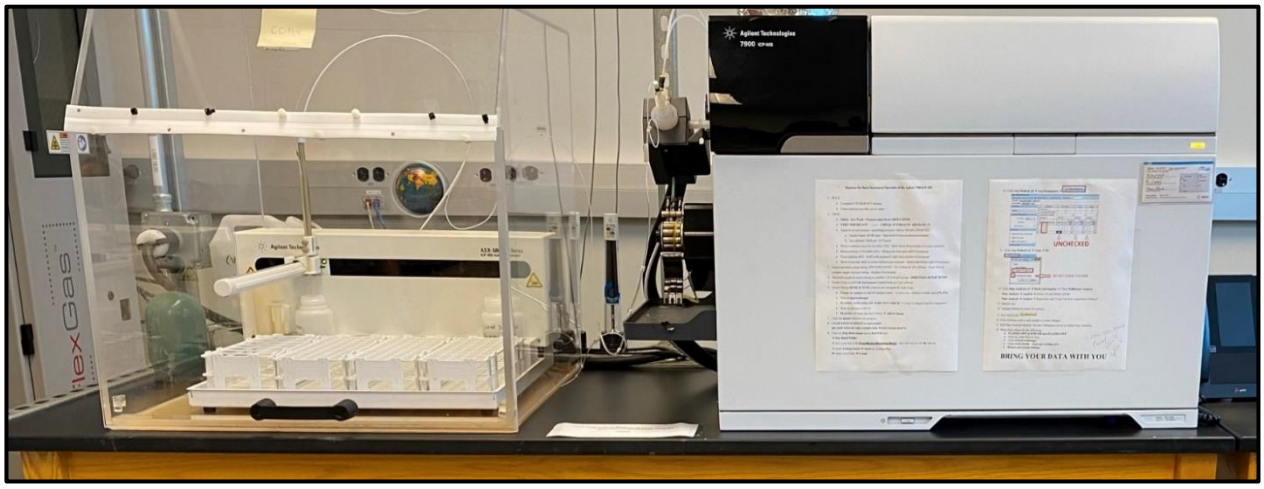

Figure 2.19. Perkin-Elmer Sciex Elan 6100 DRC inductively coupled plasma mass spectrometer.

2.5 Home-made Nanohole Device Fabrication and Mask Layout

In this dissertation, 250×250 nm nanohole structure devices were used as selector devices which were provided by our project collaborators from Pohang University of Science and Technology (POSTECH). Additionally, home-made nanohole devices have been furbished at UTD cleanroom facility situated in Natural Science and Engineering Research Laboratory (NSERL) building.

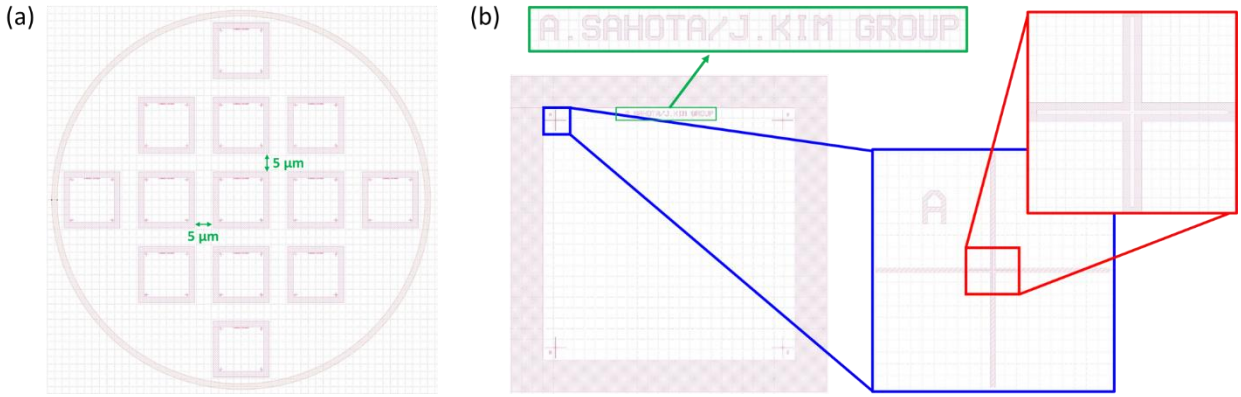

Figure 2.20. Home-made nanohole structures mask layout, (a) Entire 4-inch wafer, and (b) zoomed-in images of single cell design in (a).

Figure 2.22 shows an image of the mask layout designed for fabricating home-made nanohole structures in this work. Varied device sizes were prepared ranging from 50 to 500 nm. Figure 2.22a shows the entire patterned 4-inch wafer, while Figure 2.22b shows the zoomed-in images of various mask layout features. All the TS selector devices discussed in this dissertation were completely or partially fabricated in either the UTD cleanroom facility or Professor Jiyoung Kim's lab.

CHAPTER 3

ULTRA-STEEP SLOPE THRESHOLD SWITCHING SELECTORS REALIZED VIA ATOMIC LAYER DEPOSITION METHOD

Authors – Harrison Sejoon Kim, [a,*] Akshay Sahota, [b,*] Xin Meng, [b] Jaidah Mohan, [a] Yong Chan Jung, [a] Jang-Sik Lee, [c] Si Joon Kim, [d] and Jiyoung Kim [a,b]

[a] Department of Materials Science and Engineering, RL 10
The University of Texas at Dallas
800 West Campbell Road
Richardson, Texas, 75080, USA

[b] Department of Electrical Engineering, EC 33
The University of Texas at Dallas
800 West Campbell Road
Richardson, Texas, 75080, USA

[c] Department of Materials Science and Engineering
Pohang University of Science and Technology (POSTECH)
77 Cheongam-ro,
Pohang 790784, Republic of Korea

[d] Department of Electrical and Electronics Engineering
Kangwon National University
1 Gangwondaehakgil
Chuncheon, Gangwon-do, 24341, Republic of Korea

[*]Equally contributing authors

The contents of this Chapter are partially (or in parts) adapted from a manuscript – *under preparation*, entitled "Novel Approach using Atomic Layer Deposition of Ag Doped O_3-based Crystalline ZnO Films for Ultra-Steep Threshold Switching Selector". The authors are Harrison Sejoon Kim, Akshay Sahota, Xin Meng, Jaidah Mohan, Yong Chan Jung, Jang-Sik Lee, Si Joon Kim, and Jiyoung Kim. I am a co-first author in this manuscript together with Dr. Harrison S. Kim, and contributed towards the experimental execution, device fabrication, electrical characterization in conjunction with manuscript preparation and corrections.

3.1 Preface

For the technological advancement of emerging non-volatile memories (NVM), several selector devices have been investigated for suppressing sneak/leakage current arising in a X-point array framework. Leakage current originating from neighboring unselected cells is a big roadblock for expanding the hardware design to achieve ultrahigh density (*e.g.*, 3-dimensional crossbar architecture). Metal-filament type atomic switches have been proposed as TS selector devices that could enable the realization of ultrahigh density architectures by reducing read/write disturbance and thus controlling unnecessary power dissipation. In this dissertation, the common flaws of Ag active electrode-based TS selectors *i.e.*, cell-to-cell and cycle-to-cycle V_{th} fluctuations and lousy cycling endurance, have been rectified. In order to obtain this functionality, ZnO SL was lightly doped with Ag rather than incorporating Ag active metal layer which acts as the infinite source of Ag ions to the SL. We investigated and evaluated selector performances *i.e.*, threshold switching characteristics fabricated *via* three different methods: ECD, ALD and co-sputtering.

Volatile switching behavior of selector devices in aforementioned three cases has been studied per selector medium structure (*i.e.*, amorphous or crystalline), and per doping level (*i.e.*,

Ag concentration) for the undoped (with active metal layer) and doped (uniform or delta doping) cases. DC *I-V* and transient characteristics were studied to evaluate various electrical properties, in addition with the device failure analysis.

The first fabrication method evaluated by our group for selector fabrication was electrochemical deposition, already discussed in detail elsewhere.[47] ECD was used due to its remarkable controllability on doping concentration. However, due to its tendency to go towards non-conformal film growth and challenges in thickness and roughness control over the deposited films, atomic layer deposition was followed as the second alternative deposition technique.

3.2 Introduction

For the advancements in the information processing, storage class memory (SCM) is needed for cutting-edge computing hardware architecture.[17,24] The newly explored X-point architecture facilitates 3D stackable integration of the two-terminal SCM, thus sidestepping the potential memory wall that came into being due to intensive data processing.[6–9,93–95] The X-point array requires the SCM device to be collocated with the selection device to inhibit any crosstalk between adjacent nodes so as to prevent any degradation of sense margin window as well as keep the net power consumption under check.[96–98] Till date, a variety of two-terminal selection devices have been investigated for X-point operation, such as Schottky junctions,[99–101] poly-Si transistors,[102,103] insulator-metal transition (IMT),[42,104] mixed-ionic electronic conduction device (MIEC),[37,38] field-assisted super-linear threshold (FAST),[105,106] Ovonic threshold switching (OTS),[39–41,107] and electrochemical metallization (ECM)-based steep-slope TS selectors.[34,45,46,108] ECM-based TS selectors have garnered attention because they can meet the selector device requirements due to their abrupt non-linear *I-V* transition.[60] An ECM-based selector device

typically involves diffusion of active metal ions *e.g.*, Ag or Cu facilitated by an active metal electrode under applied bias to form a conductive path, and undergoes spontaneous rupture process of the thin and unstable filament due to steric repulsions originating between metallic atoms.[31,58,109] In broader sense, the formation of multiple filament growth points leads to stochasticity in the filament growth process, thereby making multiple bias channels with different voltage values when a filament is formed. Another encountered challenge is poor cycling endurance (Figure 3.1). In conventional approaches where an active metal electrode is employed, it acts as a source of infinite metal ions that will keep changing the filament morphology and eventually the device will become permanently shorted after repeated cycling due to radially thick and stable filament formation. These random events of multiple filament origin points could be avoided by preventing over-diffusion of active metal ions. This over-diffusion can be prevented by using alloy electrodes,[110–113] highly ordered Ag nanodots,[114] and metal doping.[115–122]

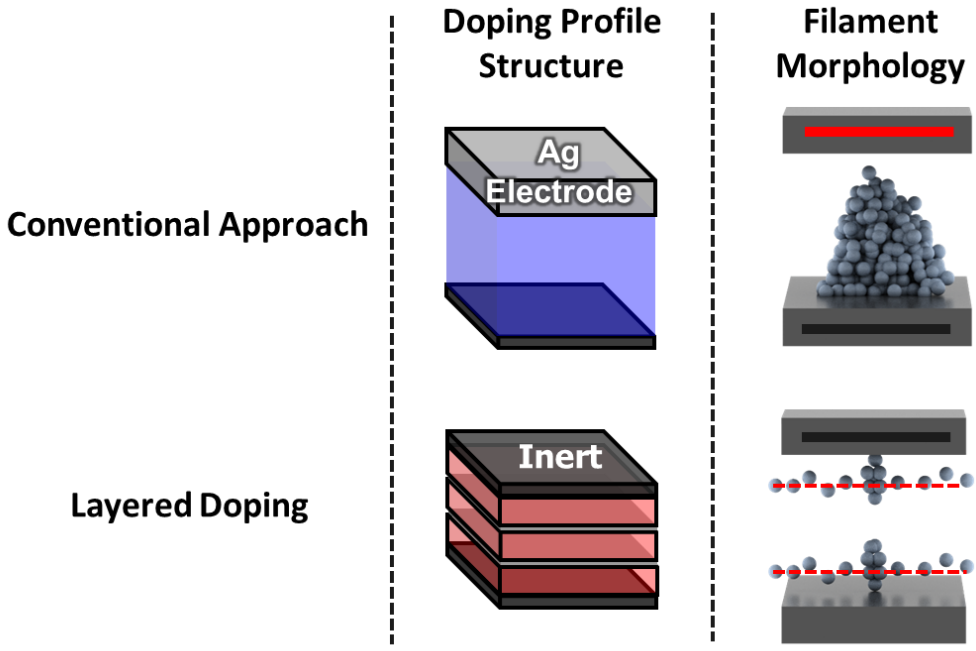

Figure 3.1. Schematic illustration of doping profile structure and filament morphology for conventional selector structures and layered doping in ALD case.

In this chapter, atomic layer deposition (ALD) technique, super-cycle ALD in particular, has been investigated to develop TS selectors as it offers precise control on dopant concentration by allowing to regulate the sequence and pulsing ratio of the dopant. Figure 3.1 shows the schematic of layered doping achievable by ALD process. Restricting the Ag ions concentration in the SL would result in a localized filament formation. In this work, ZnO has been chosen as the SL material which has been doped with Ag as per the design of the experiments. It is expected that the crystalline ZnO (wurtzite) structure allows anisotropic diffusion of Ag ions,[123,124] thereby cutting down the randomness (Brownian motion) involved during isotropic diffusion in conventional amorphous SL structures. Moreover, when Ag is introduced as a dopant in the ZnO matrix, it lowers the leakage current as it acts as a shallow acceptor.[125–128] But ZnO is intrinsically *n*-type,[129–131] so switching is enabled by formation and rupturing of a metallic filament rather than the conduction path formed by the dielectric breakdown. This helps in sustaining a low leakage current under persistent cycling when external voltage is applied to the insulator SL. In this dissertation, ZnO works as the insulator SL which is doped with Ag to derive TS characteristics. Although, previously published articles are available for doped ZnO with super-cycle ALD technique using various dopants,[132] but Ag-doped ZnO has been realized for the first time.

3.3 Experimental Methods

For fabricating the SL, our NCD D100 crossflow ALD reactor had been equipped with deionized water, high-concentration O_3, and DEZ. Silver hexafluoropentanedionate trimethylphosphine complex, was used as Ag precursor as per DOE. Carrier and purge gas functionality was carried out by high purity (BIP grade, 99.9999%) Ar or N_2 inert gas. There was

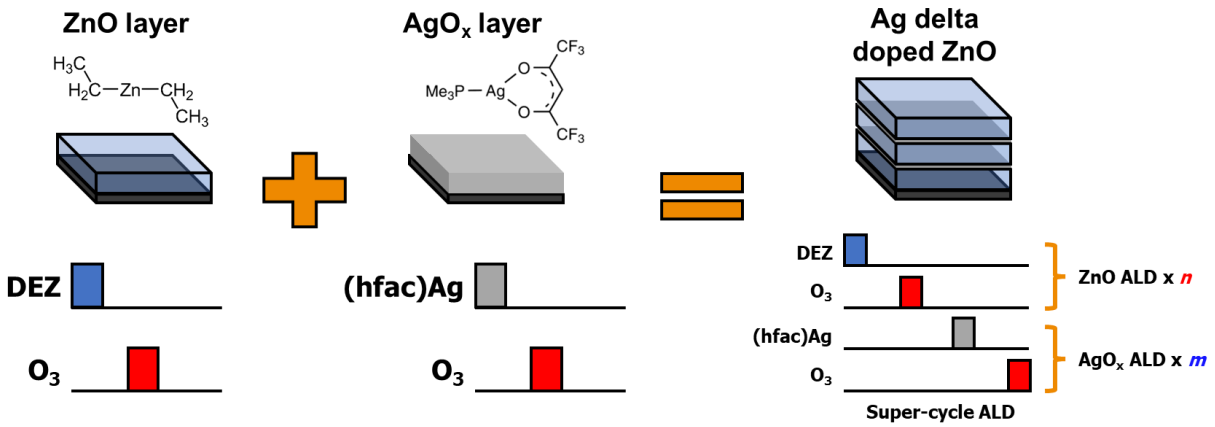

Figure 3.2. Schematic diagram of super-cycle ALD technique showing deposition sequences of ZnO, AgOx, and ZnO/AgOx layers for achieving delta-doping.

a continuous flow of 50 sccm N_2 through the reactor at 150 mtorr working pressure of the ALD system. DEZ (≥52 wt. % Zn basis, Sigma-Aldrich) and 380 [g/m^3] of O_3 served as the Zn precursors and oxidant for O_3-based ZnO ALD process, respectively. One cycle of O_3-based ZnO ALD consisted of 0.1s/15s/0.1s/30s, exposed with DEZ/N_2/O_3/N_2, respectively. We tested 100 °C, 120 °C, 150 °C, and 225 °C deposition temperatures while keeping remaining process parameters as same. The ZnO SL physical thickness was kept as ~5 nanometers.

Layered doping or the Ag delta doping was achieved by alternately depositing Ag and ZnO following a fixed ZnO deposition cycles sequentially inserted with Ag deposition cycles. One Ag-doped ZnO super-cycle comprised of '*n*' ZnO cycles followed by '*m*' silver oxide (AgO_x) cycles, as schematically shown in Figure 3.2.

A two-terminal MIM structure was fabricated for the selector devices consisting of a TE/SL/BE stack. Here Pt served as the BE material deposited via e-beam evaporation process. 5 nm of ALD ZnO served as the SL, while Ag TE was deposited on top of it via e-beam evaporator using a shadow mask of 25 μm radius. For demonstrating the device scaling effect, 250 nm × 250 nm nanohole structures (provided by POSTECH) were used.

Growth per cycle (expressed as nm/cycle) was calculated using ellipsometry (SE, J.A. Woolam, M-2000DI) method. Ohmic correlation check was first performed to make sure that the worst case with Ti/Au (20 nm/80 nm) metal contacts was greater than 0.9990 for a van der Pauw pattern. The carrier concentration was then measured at room temperature with Hall measurement (Lake Shore 8400 Series). The elemental composition was estimated using X-ray photoelectron spectroscopy (XPS, PHI Versa Probe II). The sensitivity factor and peak area were used to extract quantitative information for the SL film stoichiometry,[133] using an Al Kα monochromatic X-ray source of 1486.6 eV. Ar^+ sputtering was done to remove any adventitious surface carbons and surface oxidized species for minimizing the matrix effect of ZnO for conducting XPS study. X-ray diffraction (XRD, Rigaku SmartLab) with 1.5406 Å wavelength, was used to evaluate the crystallinity of the film. Atomic force microscopy (AFM, Veeco Dimension 5000) with the tapping mode was used to scan the surface morphology. Keithley 4200A-SCS semiconductor parameter analyzer was utilized for electrical characterization capturing DC-*IV* data. For all the device measurements, a voltage bias was applied to the TE while keeping the BE grounded.

3.4 Results and Discussion

First, the steep-slope TS behavior has been investigated for O_3-based ALD ZnO for the conventional selector structure containing Ag active electrode as TE for providing metal ions during filament formation. We prepared a simple two-terminal MIM selector structure, as shown in Figure 3.3a. DC-*IV* plots for the varied deposition temperatures *i.e.*, 100 °C, 120 °C, 150 °C, and 225 °C (Figure 3.3b) shows that O_3-based ALD ZnO can act as a volatile SL for selection

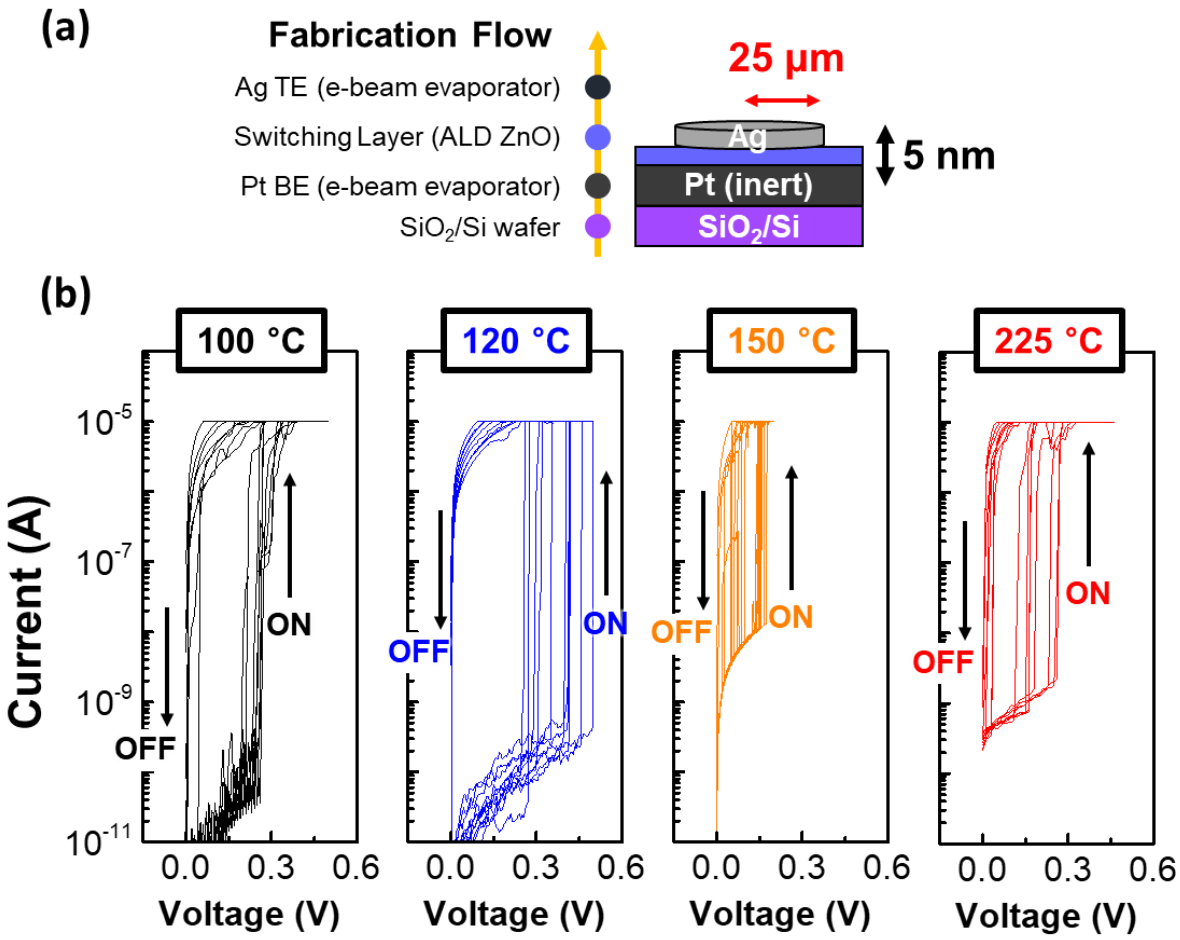

Figure 3.3. (a) Schematic illustration of process flow for selector device fabrication and device structure, (b) DC-*IV* characteristics with varied deposition temperatures.

behavior. It is common that the formation of zinc vacancies (V_{Zn}) happens more readily in O_3-based ALD ZnO, as compared to H_2O-based ALD ZnO,[134] hence V_{Zn} can be formed additionally using O_3 to provide more routes for Ag ion migration.[120] Now this ion migration via vacancy routes might be responsible for metal-filament formation in the ZnO SL, thus facilitating sequential formation of Ag filament at low applied bias.[60] It can be seen in the Figure 3.3b that there is an enhancement in off-state current with the deposition temperatures. This is in accordance with the other literature that discusses the electrical behavior using Hall effect measurement with

temperature change, involving O_3-based ALD ZnO.[135] Figure 3.4 shows the statistical chart analysis for the threshold voltages and off-state current for investigated devices. O_3-based ALD ZnO TS selector devices at 100 °C deposition temperature shows acceptable switching behavior with a decently low off-state current. Here, the off-state current can also be comprehended in terms of Zn/O atomic ratio, meaning when oxygen vacancy (V_O) defects are reduced, then the leakage current tends to reduce too, and a better crystallinity is obtained. It is reported by other groups that V_O leads to free carriers *i.e.*, electrons, in ZnO causing an enhanced off-state current.[134,136] But still it is not easy to specify V_O concentration by XPS or other methods. Usually, carbon impurities also contribute to higher leakage currents, thus a study was conducted to determine C 1s for O_3-based ALD ZnO films *(data not shown here)*, which was found to be under the tool detection limit. Although, it is quite difficult to pinpoint the exact reason behind off-state current increase, but it

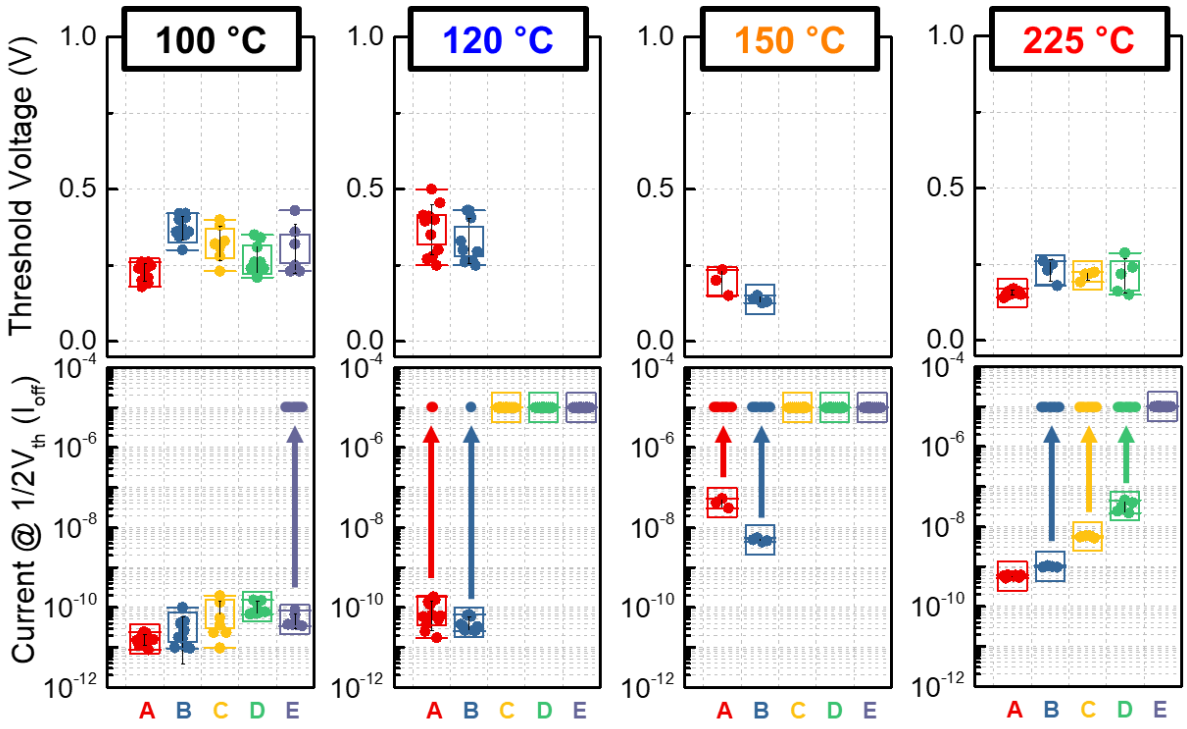

Figure 3.4. Statistical box chart analysis for threshold voltage and off-state current for varied deposition temperatures.

can be safely concluded that an increased V_O gets introduced as the deposition temperature increases, thus leading to an increased leakage current. Figure 3.5a displays the effect of device scaling on electrical properties of the selector device, keeping similar structural layout. As the conductive metal filament is the only entity responsible for entire conduction process when the selector device is in 'on' state, it basically rules out the effect of device size on the on-state current, but the lateral scaling would rather lead to amplification in the current density, J_{ON} for the on-state.

Hence, when the device size is decreased to ~0.06 μm^2 (Figure 3.5b), J_{ON} got amplified to 0.1 MA/cm^2. On contrary, the off-state leakage drops down when the size reduces as it commonly is affected by any change in the device size. These two effects of decreased off-state leakage currents and increased on-state current density when combined together, results in a high selectivity (I_{on}/I_{off}) ratio *i.e.*, ~10^9 in this case. Next, transient behavior has been evaluated for the selector devices to determine the turn-on speed (Figure 3.6a) and the time taken by the conductive filament for

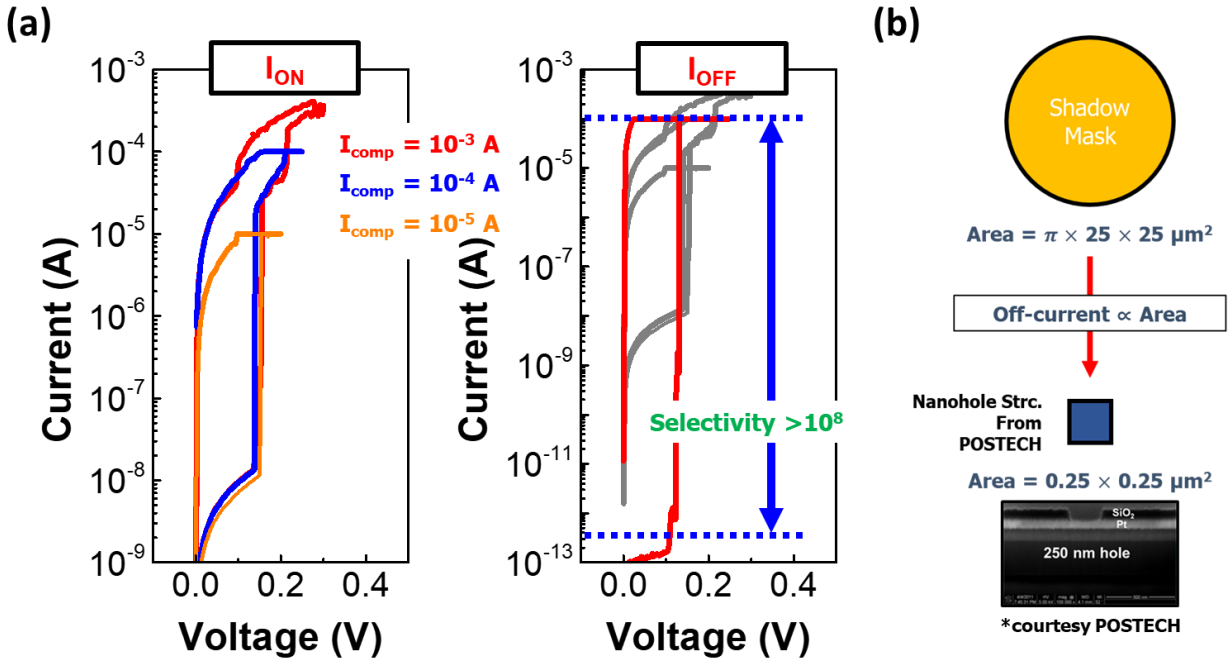

Figure 3.5. (a) Effect of device scaling on the electrical characteristics of the O_3-based ALD ZnO selector, (b) Schematic representation of the used device sizes.

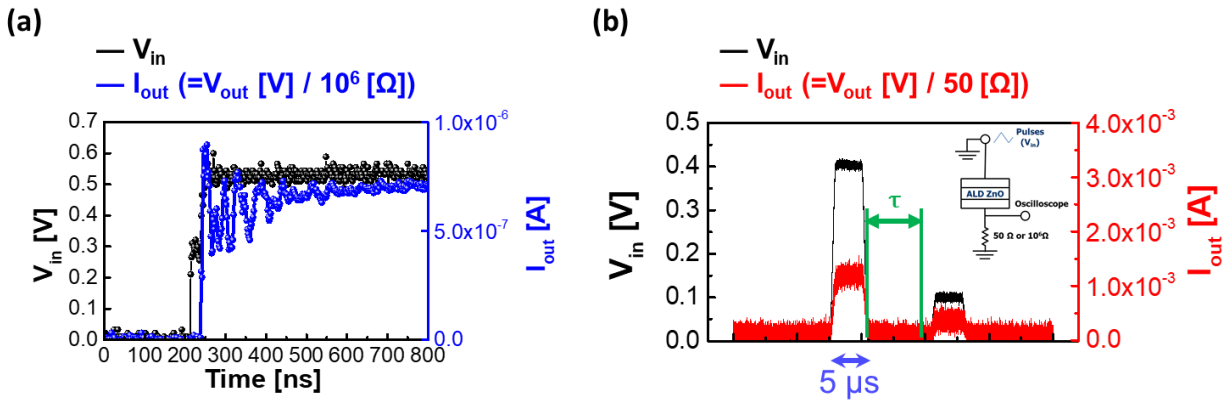

Figure 3.6. Transient behavior of O3-based ALD ZnO selector devices showing (a) Switching speed, and (b) Filament dissolution time.

completely dissolving (Figure 3.6b). A waveform generator serially connected to a shunt resistor of 3 kΩ was used to input a square pulse to the TS selector device (inset image). Turn-on/switching speed represents the time taken by the selector device to exhibit any change in the output voltage oscilloscope channel after the application of the input square pulse, while the dissolution time is dependent on how quickly the metal filament can spontaneously rupture under zero bias in an effort of minimizing steric repulsions.[44,137] O_3-based ALD ZnO selectors showed a switching time of <50 ns (Figure 3.6a) which is decent enough as compared to other prevalent ECM-based TS selectors.[44,45,138] It is available that the ECM-based TS selectors typically show a dissolution time (τ) >10 μs.[58,109,139–142] We also confirmed that the dissolution time in our case of O_3-based ALD ZnO selectors, incorporating an Ag active electrode, display a relaxation time of more than 10 μs (Figure 3.6b).

As discussed in Figure 3.3, O_3-based ALD ZnO selector devices showed an interesting DC-*IV* trend when deposition temperature was increased. So, to further understand this behavior, we investigated the physical and chemical characteristics of the various O_3-based ALD ZnO thin films. The deposition temperature can alter the preferred orientation of the ZnO, thus usually

determines the crystal structure in the ALD ZnO. The crystallization happens in most preferred hexagonal wurtzite phase for the H_2O-based ALD ZnO, even for the relatively low deposition temperature such as ~130 °C.[143] When the deposition temperature is less than 70 °C, there is an observance of a strong preferred *c*-axis orientation for the ZnO films.[144,145] In the 160 – 200 °C deposition temperature range, ZnO grains are found to be oriented in a non-preferred orientation along *a*-axis due to the formation of (100) dominant direction above 70 °C.[146–148] When the deposition temperature is further increased beyond 220 °C, the (002) preferred orientation returns back.[143] But the O_3-based ALD ZnO case is surprisingly different from H_2O-based ALD ZnO. X-ray diffraction (XRD) spectra with $\theta/2\theta$ scanning mode shows an increase in β – integral breadth

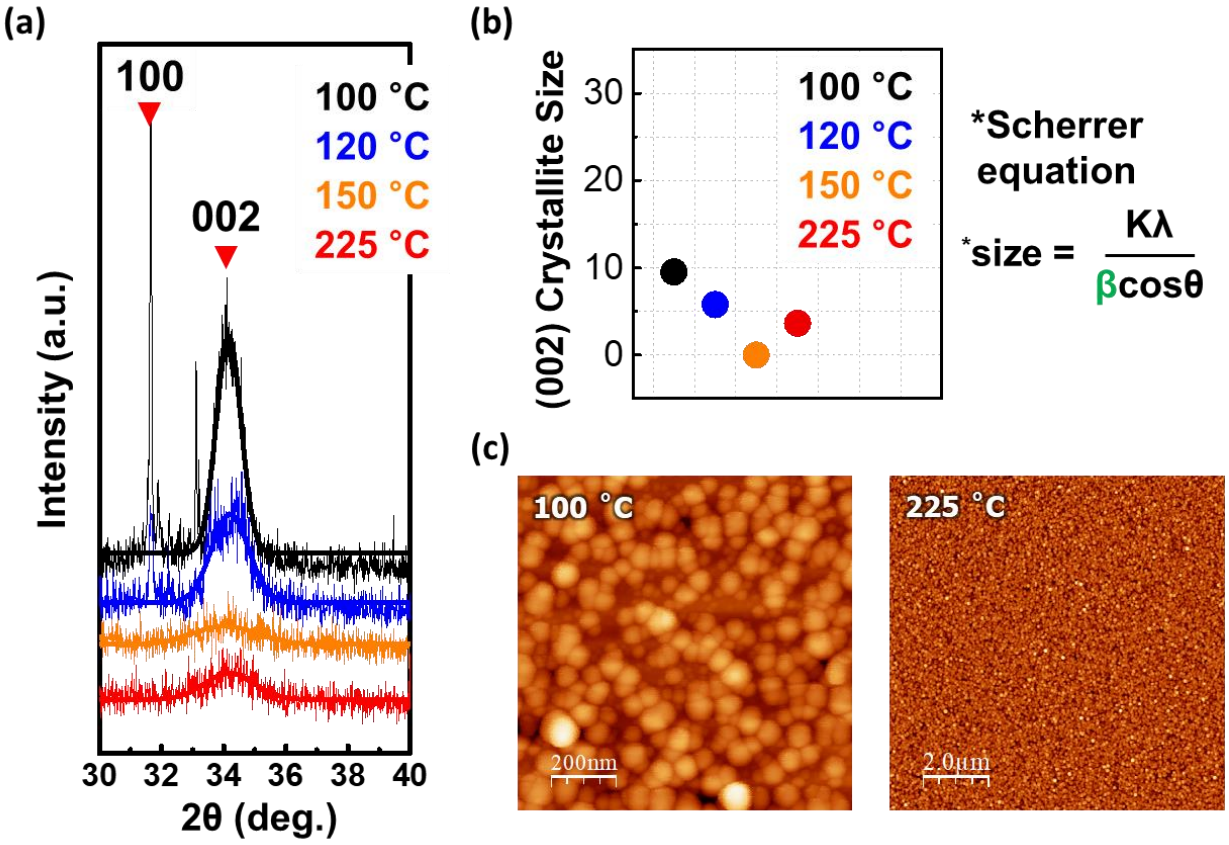

Figure 3.7. (a) X-ray diffraction spectra of O_3-based ALD ZnO thin films at varied deposition temperatures, (b) (002) crystallite sizes as calculated from Scherrer equation, and (c) AFM images of O_3-based ALD ZnO at 100 and 225 °C.

with increasing deposition temperatures (Figure 3.7a). β is normally dependent on the full width at half maximum and can be utilized for crystallite size estimation of the desired plane.[149] This acquired β (in radians) value was then plugged into the Scherrer equation, expressed as – crystallite size = $K\lambda/\beta\cos\theta$, where K denotes correction factor, λ – X-ray wavelength, θ – Bragg's angle,[150] and crystallite sizes of O_3-based ALD ZnO were calculated for (002) plane. Figure 3.7b shows the plot of crystallite size vs deposition temperatures (100 – 225 °C). The plot shows that for the O_3-based ALD ZnO, (002) crystallite size is largest for the lowest deposition temperature of 100 °C. AFM study was then carried out for further verification of the microstructure (Figure 3.7c) for O_3-based ALD ZnO at 100 and 225 °C, which shows an evident morphology difference between the two cases. For the 100 °C case, average grain size turned out to be roughly 20 nm, while it was 10 nm for O_3-based ALD ZnO at 225 °C. This anomaly between the microstructure results obtained by AFM imaging and Scherrer equation are not perfectly consistent because grains do not always consist of a single crystal. However, it visually confirms that for the lower temperature, the grain size will be larger for O_3-based ALD ZnO. This result is quite interesting as H_2O-based ALD ZnO typically shows a complete inverse trend of poorer crystallinity at lower deposition temperature. This could possibly be happening because O_3-based ALD ZnO has dominant nucleation rate regions of heterogeneous nucleation, thus there is a decrease in nucleation sites at lower deposition temperature, resulting in a bigger grain size and thus enhanced crystallinity.

The volatile switching results discussed until now were for the case of Ag active electrode-based TS selector devices. The current section discusses the delta doping or layered doping of the ZnO by Ag metal through O_3-based ALD ZnO. So, the first step is to prepare a recipe for the Ag ALD process, which was carried out by using Silver hexafluoropentanedionate trimethylphosphine

complex as the Ag precursor (Figure 3.8a) and ozone (380 g/m^3) as the reducing agent. Ag precursor (99% purity, Strem Chemicals) typically comes packaged in a stainless-steel cylinder for its utilization in the deposition systems. For achieving desired vapor pressure, the precursor bottle was heated at 95 °C and for the prevention of precursor condensation at the reactor inlet, the precursor lines were maintained at a temperature of 105 °C. One full cycle of Ag ALD comprised sequential exposures of Ag(10s)/N_2(100s)/O_3(30s)/N_2(100s) (Figure 3.8a). We chose a deposition temperature above 115 °C because of the temperature matching between the ALD reactor and the Ag precursor. Additionally, Ag ALD processes using $PMe_3Ag(hfac)$, are known for their low reactivity, hence a higher deposition temperature is preferable.[151] Below 200 °C, there was a significant delay in nucleation process and it is known that a few noble metals can be conveniently deposited below the process temperature 200 °C by using thermal ALD process with ozone,[152–154] hence we carried out our deposition at a temperature of 225 °C. Ag ALD process ran for 500 cycles, yielded a film thickness of 15 nm which gives a GPC of 0.03 nm/cycle using $PMe_3Ag(hfac)$ and O_3. The XPS spectra of the Ag 3d peak has been shown in Figure 3.8b, which gives

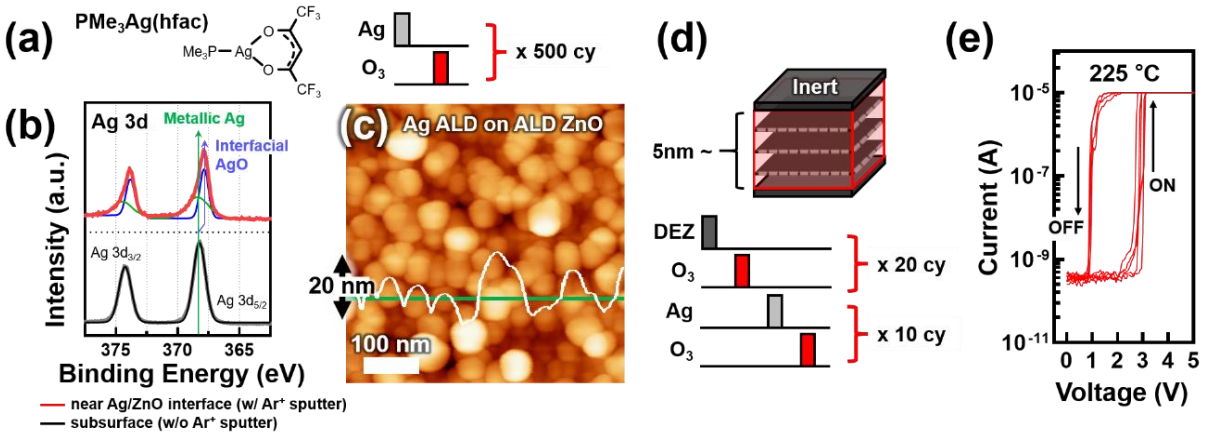

Figure 3.8. Schematic for Ag ALD and delta-doped ZnO. (a) $PMe_3Ag(hfac)$ precursor. (b) XPS spectra for Ag 3d. (c) AFM image for delta-doped ZnO substrate. (d) Schematic structure for selector device by layered doping, and super-cycle ALD sequence used in this work. (e) DC-*IV* characteristic for delta-doped threshold switches.

information on the chemical bonding at the interfacial Ag and ZnO surface. Since the penetration depth of XPS is approximately 10 nm because of its low energy (20 – 2000 eV), so if Ar^+ sputtering is not performed (Figure 3.8b, bottom plot), then most commonly the subsurface information would be dominant. In the XPS spectra, it can be observed that the Ag 3d peak corresponds to a single Gaussian peak which is assigned to metallic Ag. $3d_{5/2}$ peak for metallic Ag is found to position at 368.3 eV. It was observed that if Ar^+ sputtering is continued (Figure 3.8b, upper plot), the $3d_{5/2}$ peak can be deconvoluted into two subpeaks – a) metallic Ag positioned at 368.3 eV, b) AgO positioned at 0.5 – 0.7 eV lower than metallic Ag.[128,155] It has been noted that at Ag/ZnO interface, a part of AgO subpeak shows dominance compared to metallic Ag, which could possibly be happening as per our *in-situ* QCM study employing $PMe_3Ag(hfac)$, which states that the Ag precursor reacts with Al–O surface, with a byproduct of PMe_3.[153] Figure 3.8c displays the AFM image of the ALD grown Ag on ZnO surface which clearly displays crystalline growth of Ag achieved without any thermal treatment. The coalescence results in varied grain size distribution due to continuous growth of different nuclei. AFM result shows that there is a uniform deposition of the Ag even for a larger area but contains some delays at certain nucleation sites which is a common observation in case of ALD grown noble metals/oxides.[152,156]

Figure 3.8d shows the delta/layered doping profile that was achieved using Ag and ZnO ALD processes ran alternatively. In this doping profile, Ag layers were repeatedly sandwiched between the O_3-based ALD ZnO layers using super-cycle process. Now this one super-cycle comprised of 20 ZnO cycles, followed by 10 Ag cycles. When three such super-cycles were repeated, it yielded a thickness of 5 nm. The concentration of dopant (atomic percent) was challenging to quantify by XPS due to tool detection limit but could be estimated to be around ~17

at. % based on deposition rate. For determining the threshold switching behavior, we fabricated a simple two-terminal MIM (Pt/Ag:ZnO/Pt) selector structure without an active Ag metal layer, instead Ag was delta-doped inside the ZnO matrix as previously discussed in the super-cycle ALD process (Figure 3.8d). Figure 3.8e shows the volatile switching characteristics (DC-*IV*) of the steep-slope TS selector fabricated via super-cycle delta-doped ALD process. The selector devices show enhanced control over threshold voltage variances which could be attributed to restricted Ag amount via metal doping of SL,[115–117,121,122,157–160] which helps to lower down the randomness in local filament growth/nucleation. It was observed that in both the cases of Ag active electrode-based and Ag delta/layered doping-based selector devices, they exhibit a steep switching slope (subthreshold swing) of 10 mV/dec. It was observed that delta-doping based selector devices returned to off-state quickly as compared to Ag active electrode-based selectors, with a hold voltage of ~1 V, while the latter case had a hold voltage of nearly 0 V. Although, there is no exact explanation for this behavior, but it is expected that the unwanted phosphorous and fluorine elements coming from the $PMe_3Ag(hfac)$ precursor could be the reason for hold voltage increase for super-cycle ALD based selector devices. Also, the off-state leakage current is lower in this case in contrast to Ag active electrode-based selectors case. This is expected to happen as the Ag substitution at Zn site (Ag_{Zn}) is the most stable dopant state which act as a shallow acceptor in ZnO (wurtzite) matrix, lowering the leakage current.[126–128,161] As can be seen that the difference in off-state leakage is not that significant, it is expected to happen due to delays in nucleation cause by initial ALD cycles during the Ag ALD process. Additionally, the threshold voltage for delta-doping based selector devices is also higher than that of electrode-based selectors. The restrained influx of Ag ions into the SL in case of delta-doped devices could be responsible for this high

threshold voltages which is in indirect indicative of threshold voltage tunability by regulating Ag dopant concentration in the SL by well-controlled super-cycle ALD process.

3.4.1 Super-cycle ALD process challenges

Although, super-cycle ALD process presented as a novel alternative option to develop ECM-based TS selectors providing atomic percent control over Ag doping levels and gave benefits like threshold voltage tunability and higher hold voltages, but there were some serious downsides of the process as well. The super-cycle ALD process posed severe reproducibility issues due to the non-uniformity of the Ag precursor *i.e.*, $PMe_3Ag(hfac)$. Figure 3.9 (a-c) shows the AFM images of different super-cycle O_3-based ALD ZnO thin films fabricated at same deposition process parameters but shows completely inconsistent morphological behavior. The grains size was measured to be ~1.5 nm by ellipsometry which is significantly different from what discussed previously in Figure 3.7b. Due to this major reproducibility issue, the super-cycle ALD process was discontinued and succeeded by the sputtering/co-sputtering process, discussed in next chapter, to evaluate the selector device feasibility.

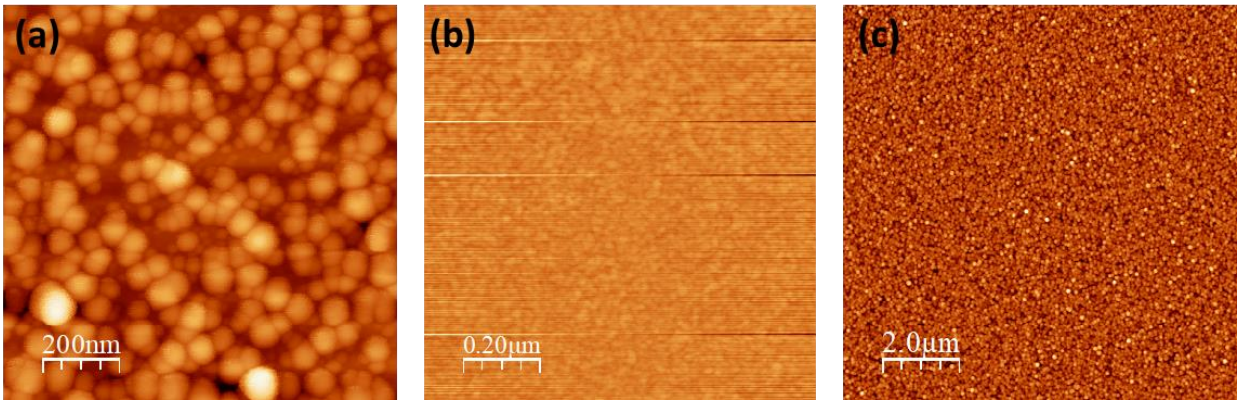

Figure 3.9. AFM images for same deposition conditions for super-cycle ALD process showing reproducibility issues.

3.5 Summary

In conclusion, we report a novel approach of threshold switching selector fabrication via super-cycle ALD process. Before implementing the super-cycle ALD process, we developed two different type of films – a) ZnO SL with low off-state current, b) Ag thin films for interlayer in the delta-doping case. As the O_3-based ALD ZnO process shows nucleation rate preferred growth mode, it led to enhanced crystallinity at low deposition temperatures. It was also confirmed by the O_3-based ALD ZnO stoichiometry that lesser defective films can be grown at lower deposition temperatures. We also demonstrated the feasibility of a volatile switching layer using O_3-based ALD ZnO, that exhibits decently low off-state current leakages, with < 50 ns switching speed. Ag delta doping-based TS selectors were successfully fabricated with the sequential introduction of Ag ALD into the ZnO ALD process thus constituting a super-cycle ALD method. Ag delta doping-based TS selector devices show benefits of lowered variability in threshold voltages and quicker filament dissolution thus resulting in faster turn-off speed compared to Ag active electrode-based TS selectors. Finally, this work shows the possibility of a new pathway for metal doping in addition to sputter technique, with precise controllability on the dopant concentration.

CHAPTER 4

SPUTTERING/CO-SPUTTERING APPROACH FOR DEVELOPING METAL-FILAMENT TYPE VOLATILE THRESHOLD SWITCHING SELECTORS

Authors – Akshay Sahota,[a] Harrison S. Kim,[b] Jaidah Mohan,[b] Yong Chan Jung,[b] Heber Hernandez-Arriaga,[b] Dan N. Le,[b] Si Joon Kim,[c] Jang-Sik Lee, [d] Jinho Ahn,[e] and Jiyoung Kim [a,b]

[a] Department of Electrical Engineering, EC 33
The University of Texas at Dallas
800 West Campbell Road
Richardson, Texas, 75080, USA

[b] Department of Materials Science and Engineering, RL 10
The University of Texas at Dallas
800 West Campbell Road
Richardson, Texas, 75080, USA

[c] Department of Electrical and Electronics Engineering
Kangwon National University
1 Gangwondaehakgil
Chuncheon, Gangwon-do, 24341, Republic of Korea

[d] Department of Materials Science and Engineering
Pohang University of Science and Technology (POSTECH)
77 Cheongam-ro
Pohang 790784, Republic of Korea

[e] Division of Materials Science and Engineering
Hanyang University
222 Wangshimni-ro, Seongdong-gu
Seoul 04763, Republic of Korea

The contents of this Chapter are partially adapted from two manuscripts entitled "Nano-polycrystalline Ag doped ZnO layer for steep-slope threshold switching selectors" – *accepted* and "Highly Reliable Selection Behavior with Controlled Ag Doping of Nano-polycrystalline ZnO Layer for 3D X-Point Framework" – *under journal review*. I am a first author in both the manuscripts, and contributed towards the experimental design and execution, device fabrication, electrical characterization in conjunction with manuscript preparation and corrections. The content of this Chapter is adapted with permission from (Nano-polycrystalline Ag doped ZnO layer for steep-slope threshold switching selectors). Reproduced with permission from AIP Advances.

4.1 Preface

As discussed in previous chapter, ALD and ECD processes provided a basic understanding on the delta/layered doping and the uniform doping of the ZnO switching layer with Ag and the associated benefits for minimizing the filament growth stochasticity; a common flaw primarily found in Ag active reservoir electrode-based TS selectors. Both the ALD and ECD methods demonstrate the effects of doping on TS characteristics, specifically the enhancements in V_{th} variances and device cycling endurance. However, the interpretation of operational mechanism per Ag doping concentration remains cryptic. Moreover, ALD and ECD processes have their own challenges like reproducibility issues, thickness/roughness controllability and both enables only one specific type of doping profile to be investigated at a time. Sputter/co-sputter technique on the other hand offers some benefits over the ALD and ECD processes– a) High thickness controllability, b) Uniform film morphology, c) Ability to support both layered/delta and uniform doping profiles, and finally, d) Process versatility to grow amorphous and polycrystalline thin films by tuning sputter deposition parameters.

Hence, sputtering/co-sputtering method has been investigated for fabricating simple MIM structured TS selector devices with varied Ag concentrations. Delta and uniform doping profiles have been tested for their feasibility and respective switching characteristics have been demonstrated. Also, a comparative study has been conducted to identify differences in the switching behavior for polycrystalline versus amorphous ZnO films.

4.2 Introduction

Recent breakthrough in 3D X-point architecture arrays has put them in spotlight for the studies related to implementing the next-generation high-density non-volatile memory technology for futuristic neuromorphic, and stand-alone memory applications.[17,24,93,162] 3D X-point structure fulfills the requirements of extremely high memory density using a simple device structure and also offers cost benefits in memory industry owing to the 3D stacking viability, thereby lessening bit cost per memory chip.[48,163–165] However, a X-point architecture suffers from an inevitable issue of sneak leakage path which is detrimental for its practical application as it increases overall power consumption as well as amplifies the read/write disturbance.[48,98,105,106,166] Thus, developing a selector device that prevents the sneak-current for an unselected cell within a X-point array, is required to mitigate this issue. An ideal selector device should inhibit any leakage current through the unselected cells offering high resistance at low bias, while turning on after crossing certain threshold voltage (V_{th}) enabling current flow for the selected memory cell.[167] A lot of selector devices have been engineered until now to satisfy the X-point architectural requirements,[48–50] but amongst them TS selectors, namely MIT selectors,[42,43] OTS selectors,[39,41] and Ag (or Cu)-based steep-slope TS selectors,[34,45,47,168,169] have garnered a lot of attention. MIT and OTS selectors

despite of having exceptional endurance and reliability, suffer from a big flaw of high I_{off} (~10^{-7} A) which makes them unsuitable for next generation high-density memory applications.[48,98,170,171] Ag-based steep-slope TS selectors alternately, outshine all other selector devices due to their exceptional features like extremely low leakage (OFF-state) current (<1 pA), high I_{on}/I_{off} ratio (>10^7), small subthreshold swing (<10 mV/decade) and high current-density (>1 MA/cm^2), yet having a simple MIM structure.[34,44,45,47,172,173]

The traditional approach of Ag-based TS selector fabrication involves depositing individual layers of metal oxide and Ag active reservoir electrode to form a MIM stack where the Ag electrode provides metal ions to the oxide layer for conductive filament formation once enough operational voltage (>V_{th}) is applied to the device. But as this conduction mechanism of metallic filament formation in an active reservoir electrode-based system has a stochastic nature, it therefore gives rise to unavoidable intrinsic variabilities.[26,27] Hence, parameter variability, *e.g.*, shifts in V_{th} and poor cycling endurance are inherent issues predominantly found in active reservoir electrode-based TS selectors.[61] Majority of the prevailing selector devices comprise of amorphous SL structure,[174–181] thus commanding isotropic diffusion of Ag ions, incorporating randomness. Another undesirable factor in Ag-based TS selectors is the necessity of electroforming (EF) process that requires higher applied voltage than the operating voltage.[115] During the EF process, large Ag clusters having several nanometers of diameter are formed which do not diffuse out completely from conductive path when applied voltage is removed and these residual Ag clusters thus lead to high I_{off} in subsequent off-state, causing significant device performance deterioration.[34,115,172] TS selectors suffer from the issue of having non-volatile filament formations at high on-currents, possibly due to uncatered supply of Ag ions from active reservoir electrode to

the SL, leading to memory switching behavior, which is unpreferable for a selector device.[114,182–184] Metal doping [47,115,119,120] is thus one of the methods that has been adopted to inhibit the active metal ion over-injection but the understanding of operational mechanism per dopant concentration, still remains unclear.

In our previous studies, TS selectors fabricated via electrochemical deposition process have been discussed,[47,119,120] but a big drawback of ECD process is difficulties on film thickness precision and smooth film growth thereby leading to non-reproducible results.[66,72,185,186] Also, solution-based ECD process is not desirable for executing conventional fabrication processes in semiconductor industry. Sputtering method on contrary, is an extensively used thin film deposition method employed by coating industries due to its capability to deposit large-scale metal-oxide films, simultaneously offering excellent controllability on thickness and doping concentration by simply adjusting sputter target power and deposition conditions.[121,128,187–189] Hence, in this work, we present a metal-filament type TS selector with a novel doping-based nano polycrystalline structure, using RF magnetron co-sputtering process. ZnO has been specifically chosen as the SL in our study because of its workability when doped with Ag,[120] hence crystalline ZnO SL with preferred *c*-axis (002) orientation can be conveniently deposited via RF magnetron co-sputtering technique.[190–192] Doping helps to regulate the influx of Ag ions during filament growth, while ZnO in its crystalline phase (wurtzite) allows facile anisotropic diffusion of Ag ions.[123,124] Although, the literatures using a multilayer selector structure to limit active metal ions influx mentioning reliability and endurance improvements are available,[187,193] but a selector employing a polycrystalline SL has rarely been reported. The presented doping-based nano polycrystalline TS selector shows enhanced TS characteristics of extremely low I_{off} (~10^{-13} A), high I_{on}/I_{off} ratio

(~10^8), improved cycling endurance, and free from the need of EF process. The results demonstrate that doping-based polycrystalline structure holds the potential to be utilized in selector devices for ultra-high density memory applications like 3D X-point arrays.

4.3 Sputter Working Conditions for Ag Active Electrode-based Selectors

4.3.1 Experimental Methods

All the experiments were performed using AJA Orion sputter deposition system, by AJA International. ZnO switching layer was fabricated using a high-purity ZnO target (99.99%, Kurt J. Lesker) at varied powers from 50 W to 250 W as per our experimental requirements. Target was sputtered in Ar+O_2 gas mixture maintaining the total flow (Ar + O_2) constant at 12 sccm. Though as per experimental requirements, Ar/O_2 ratio was varied from 2:1 to 15:1 to find the working range. The main sputter chamber was maintained at ~5 – 8×10^{-7} torr during depositions which involved a pre-sputtering for 15 – 30 minutes before every run. Working chamber pressure was tested in the range of 10 – 40 mtorr but as only 10 mtorr gave meaningful results, so all the

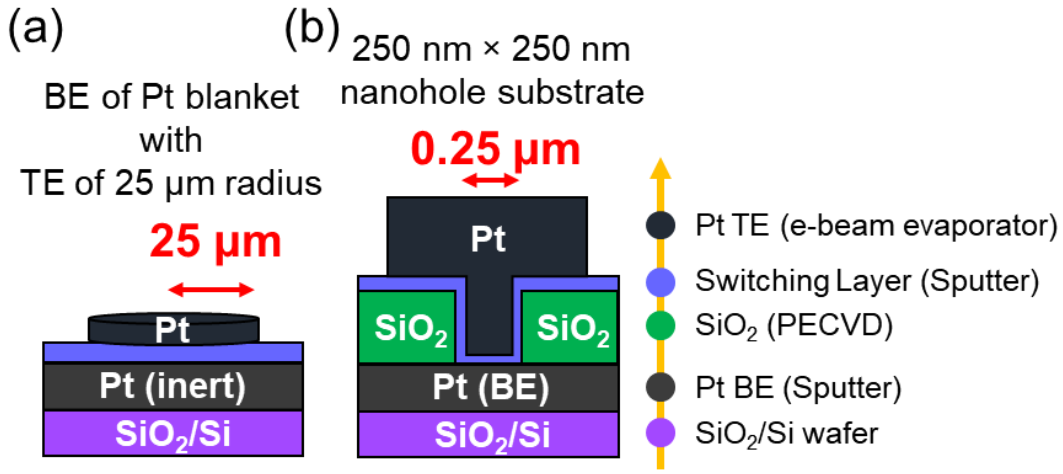

Figure 4.1. Schematic illustration of device structures and process flow for substrates with (a) Pt blanket BE having Pt TE of 25 µm radius, and (b) 250 nm × 250 nm nanohole structure substrate.

depositions discussed in this section were carried out in 10 mtorr pressure conditions. All the targets used in this dissertation were 2 inches in diameter and 0.25 inches thick. The substrate-to-target distance was ~5 inches. Sputter guns were tilted at an angle of ~30° and RF mode was used to sputter ZnO target. ZnO thin film was sputtered on top of Pt layer or 250 nm × 250 nm nanohole substrate, which is the bottom electrode in our MIM stack. Figure 4.1 shows the schematic and process flow of device structures used in this section. As previously discussed at CHAPTER 2, the nanohole structures were obtained from our project collaborators from POSTECH – Prof. H. Hwang and Prof. J.-S. Lee. The substrate was constantly under rotation at the speed of 10 rpm during deposition process. Based on the structure of our selector device, Pt or Ag top electrodes were deposited by Temescal 1800 e-beam evaporator using 25 μm radius shadow mask.

The sputter deposited ZnO switching layer's crystalline structure was determined using RAMAN spectroscopy and X-ray diffraction (XRD, Rigaku SmartLab) technique in *θ-2θ* configuration. The chemical state of ZnO switching layer was analyzed using X-ray photoelectron spectroscopy (XPS, PHI Versa Probe II) after Ar^+ pre-sputtering to get rid of any air-oxidized top species. Quantitative details about the SL elemental composition were extracted from sensitivity factor and the peak area.[133] Atomic force microscope (AFM) – Veeco, Model 3100 Dimension V was employed for examining the surface morphologies using tapping mode contact. The electrical properties were characterized using a Keithley 4200A-SCS parameter analyzer. For the electrical measurements, a voltage bias was applied to the TE keeping BE always grounded.

4.3.2 Results and Discussions

For demonstration of volatile threshold switching behavior in sputtered ZnO thin films, we first fabricated conventional Ag active electrode-based TS selectors. The first and foremost task

was to determine the working conditions for sputter tool as there were number of parameters to be tuned such as Ar/O_2 ratio, target power, and working pressure. Figure 4.2 shows the DC-*IV* data captured for different devices having Ar/O_2 ratio from 8:1 to 15:1 and devices having 100% Ar flow. It was observed that devices fabricated under high O_2 concentrations *i.e.*, Ar/O_2 ratio of 2:1 and 5:1 did not show any threshold switching behavior (*data not shown*). TS characteristics were first observed in the case of $Ar:O_2$ = 8:1 but the devices suffered from stuck-on failure *i.e.*, permanent filament formation or continuous low-resistance state, after repeated cycling. As the oxygen concentration was further reduced in cases of 10:1 and 15:1, the TS properties became better, with $Ar:O_2$ = 10:1 showing the best switching behavior. On contrary, when only Ar was flown through the chamber, the devices exhibited non-volatile memory switching rather than showing volatile switching properties. So, an interesting inference was drawn from this experiment that an introduction of slight oxygen content is mandatory to realize volatile switching behavior. To further understand this anomaly, various material characterizations were performed on the

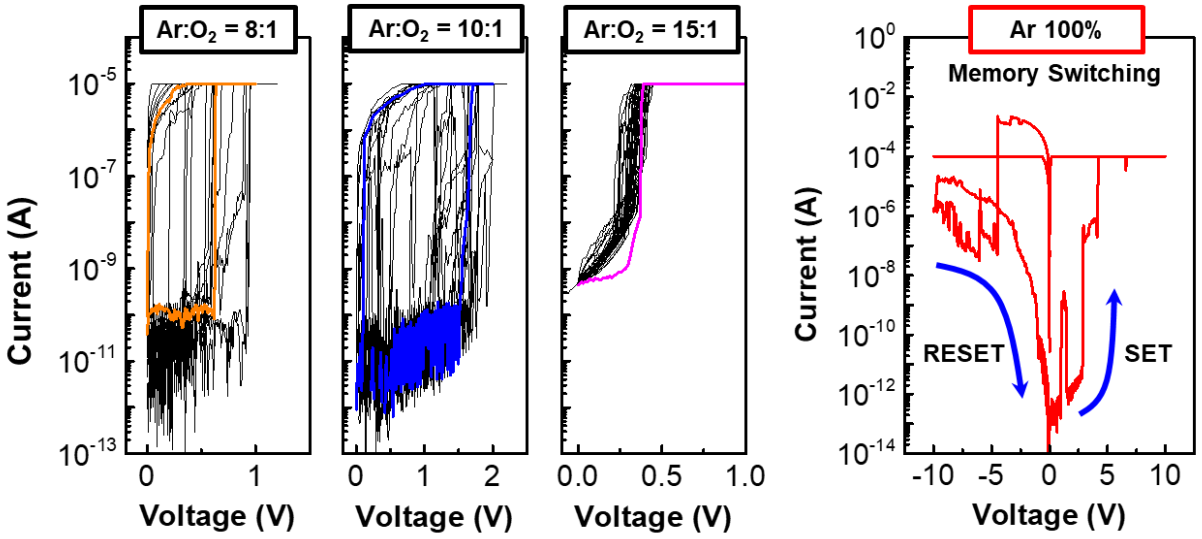

Figure 4.2. DC-*IV* characteristics for different devices having Ar/O_2 ratio from 8:1 to 15:1 and 100 % Ar.

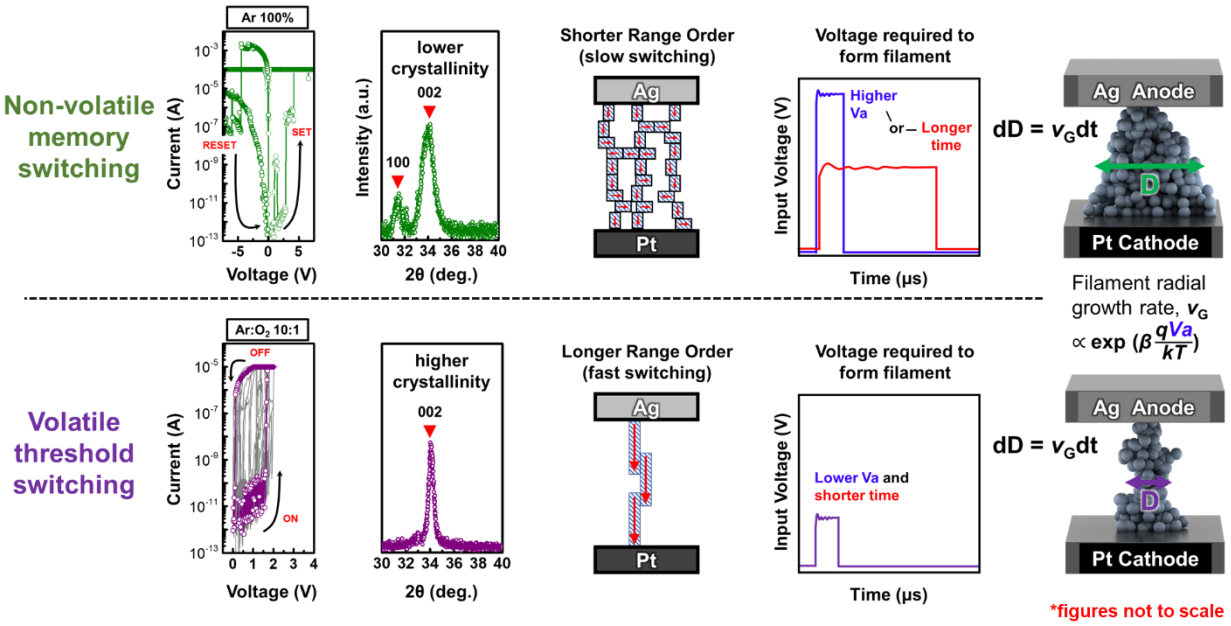

Figure 4.3. Illustration of Ag active electrode-based selector devices with sputtered ZnO volatile switching layer. Top row displays various system characteristics for 100 % Ar case that shows non-volatile memory switching due to short-range order and bottom row shows switching characteristics for Ar:O_2 = 10:1 case that shows volatile switching due to long-range order.

Ar:O_2 = 10:1 and 100% Ar cases. X-ray diffraction spectra, θ/2θ scanning mode (Figure 4.3) shows that ZnO has poor crystallinity when grown under Ar only ambient conditions while the ZnO grown under Ar:O_2 = 10:1 condition showed enhanced crystalline structure. This could be attributed to lesser induced defects in the presence of oxygen.[194–196] Moreover, (002) crystallite size was found to be larger for the Ar:O_2 = 10:1 case meaning high crystallinity possibly because of the material exhibiting long-range order that enables high diffusivity as Ag ion migration will be quicker between Pt TE and BE.[137,197] On contrary, when ZnO has poor crystallinity, the switching is supposed to be slow due to short-range order of the material system making it difficult for Ag ions to travel from one electrode to the another.[137,197] This is in direct relation to the time or voltage bias needed for filament formation per material system crystallinity. Kozicki *et al.*[198] has demonstrated that the active metal ion drift velocity is exponentially dependent on the diffusion

barrier height. The height of this hopping barrier typically reduces on application of voltage bias to the system, resulting in longer voltage pulse or high voltage amplitude for ion migration in disordered (poor crystallinity) systems. Contrastingly, the ion hopping barrier is low for material systems having a long-range order. This behavior can also be explained with the radius of metal-filament. For long-range order materials, a low voltage amplitude and time is needed for filament formation, thus the resulting filament is thin *i.e.*, small diameter while it is vice-versa for the short-range order material systems.[28]

From the results discussed at CHAPTER 3, it was inferred that crystallinity affects the TS selector operation significantly. So, to verify the same affect in sputtered films, we performed certain experiment sets varying the process parameters like working pressure, ZnO target power,

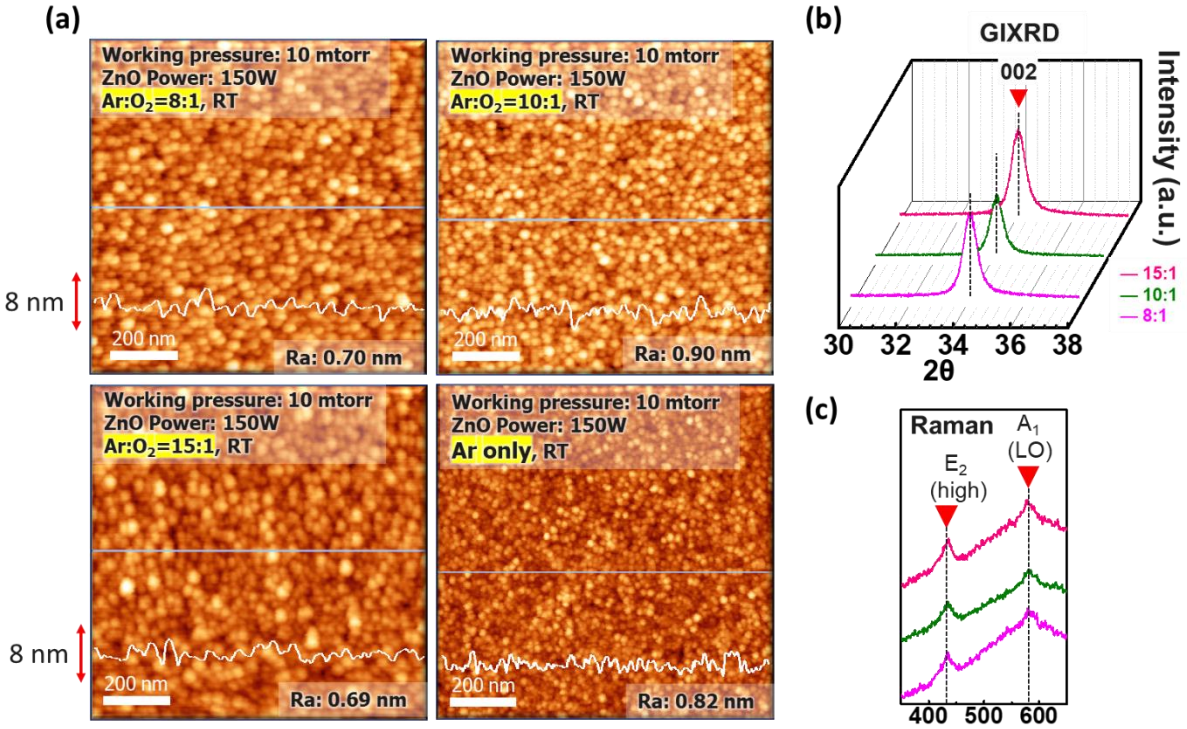

Figure 4.4. Material characterization for Ag active electrode-based sputtered ZnO films fabricated at varied Ar:O_2 ratio. (a) AFM, (b) GIXRD, and (c) Raman spectra are shown.

and $Ar:O_2$ ratio, as ZnO thin films showed chemical/physical changes under the influence.[199] Figure 4.4 shows the material characterization of the devices discussed in Figure 4.2 previously. All the AFM, GIXRD and RAMAN spectra points that the highest crystallinity with preferred *c*-axis orientation for ZnO wurtzite phase was obtained for the case of $Ar:O_2$ = 10:1 when other deposition parameters were kept constant *i.e.*, ZnO target power – 150 W, working pressure – 10 mtorr and deposited at RT. The results demonstrate that introducing oxygen resulted in larger grain size which is consistent with our previous inferences.[194–196] So, it is believed that presence of oxygen helps the grain to grow stably with minimized defects resulting in enhanced crystallinity.

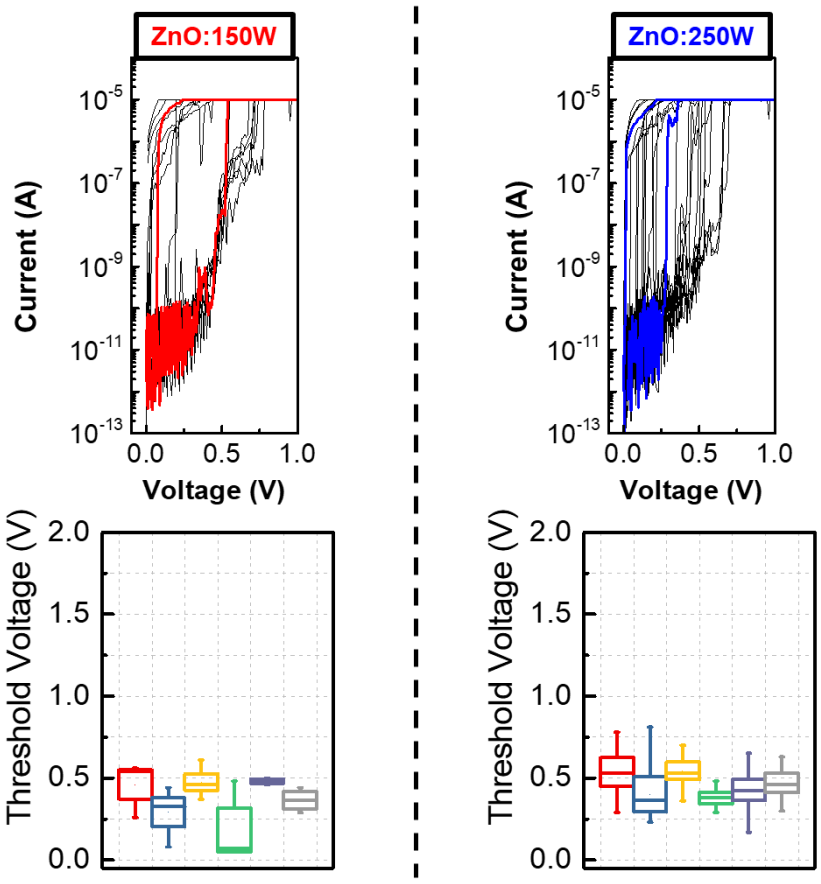

Figure 4.5. DC-*IV* characteristics and corresponding statistical device analysis for the selector devices deposited at ZnO target power of 150 W and 250 W.

Another regime that we tested to investigate its impact on the ZnO SL film quality, was ZnO sputter target power.[200] Different selector devices were fabricated at ZnO target powers ranging from 50 W to 250 W. Figure 4.5 shows the DC-*IV* characteristics and respective statistical analysis for the devices with SLs deposited at target power of 150 W and 250 W, when rest of the deposition parameters *i.e.*, Ar:O_2 ratio, working pressure, and deposition temperature were maintained constant at 10:1, 10 mtorr, and RT respectively. No TS was observed below the target power of 150 W with the devices showing immediate stuck-on failure, so those plots have not been shown here. It was observed that ZnO at 150 W showed better TS properties with lower V_{th} fluctuations as compared to the 250 W case where more variances in the V_{th} were observed. To understand this behavior, material characterization was performed (Figure 4.6). As per the AFM images, ZnO deposited at 50 W grew as an amorphous film rather than showing crystallinity which

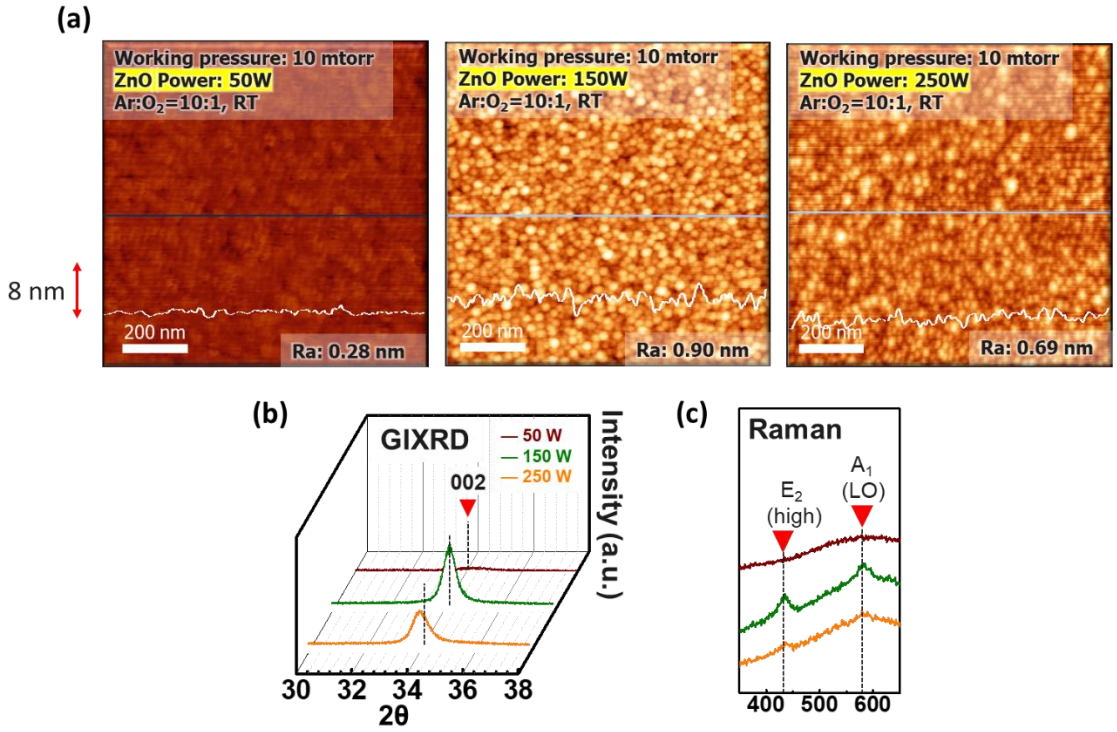

Figure 4.6. Material characterization for Ag active electrode-based sputtered ZnO films fabricated at varied ZnO target powers, showing (a) AFM, (b) GIXRD, and (c) Raman spectra.

was observed for higher powers of 150 W and 250 W (Figure 4.6a). This observation was further complemented by GIXRD (Figure 4.6b) and RAMAN (Figure 4.6c) analysis which showed largest grain size for (002) plane and high E2 peaks for RAMAN, respectively. This interestingly points out that highest crystallinity is not directly dependent on target power as there is a probability of surface damage to the deposited ZnO film by high energy ion bombardment during sputtering at higher powers. At the same time, if the film is grown at very low target power like 50 W, then the film shows amorphous nature with lots of ZnOH incorporation and lacks any volatile switching behavior. This can be further correlated to our proposed theory at Figure 4.3, that disordered material arrangement requires higher voltage bias for filament formation, ultimately leading to a stable and radially thick filament.

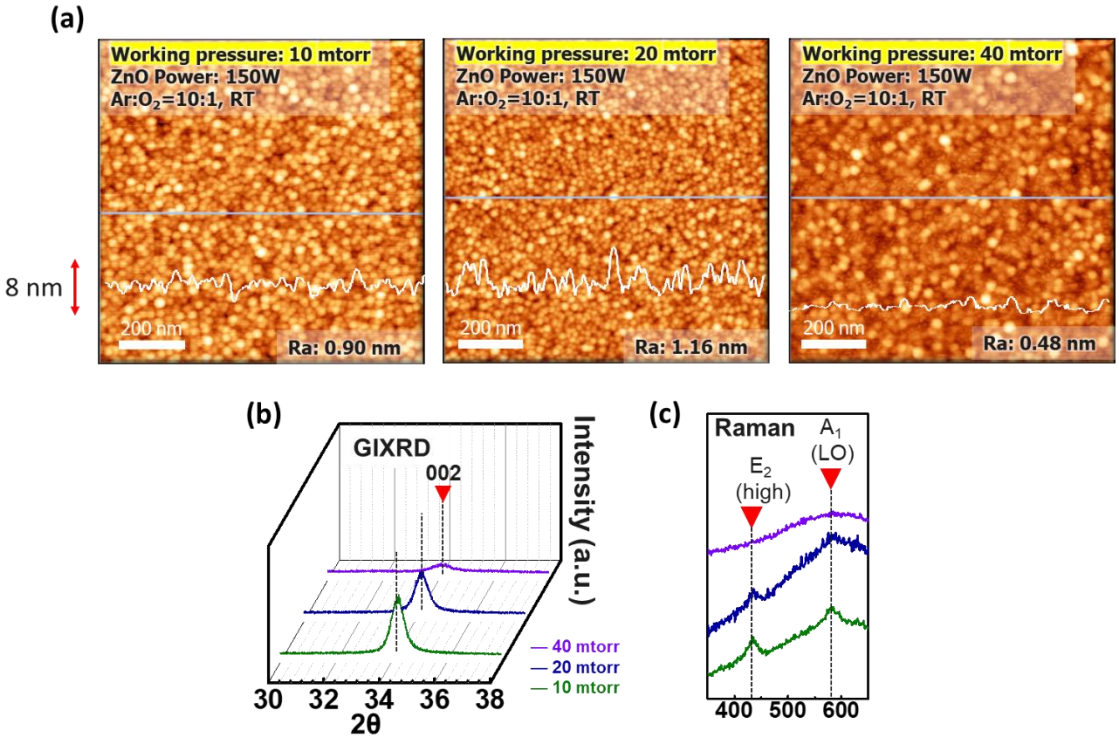

Figure 4.7. Material characterization for Ag active electrode-based sputtered ZnO films fabricated at varied working pressures, showing (a) AFM, (b) GIXRD, and (c) Raman spectra.

The last parameter tested was the working pressure, when other deposition parameters *i.e.*, Ar:O_2 ratio, ZnO target power, and deposition temperature were respectively kept constant at 10:1, 150 W, and RT. As per the AFM images (Figure 4.7a), GIXRD spectra (Figure 4.7b), and RAMAN analysis (Figure 4.7c), it can be seen that the film growth at highest working pressure of 40 mtorr is amorphous. It is possibly because the kinetic energy of the sputtered target material lowers at high pressures due to shorter mean free paths. This in turn lowers down the probability of the Zn adatoms on the surface to find a thermodynamically favorable site in the wurtzite structure of ZnO, which eventually results in a poor crystallinity. As previously mentioned, ZnO whenever has a disordered arrangement, it does not show any switching characteristics. Particularly in this case it was observed that the TS selector devices suffered from stuck-off failure *i.e.*, continuous high-resistance state which implies that the Ag ions encountered a difficulty in filament formation possibly due to low probability of Ag ion aggregation at cathode interface. Table 4.1 summarizes all the working conditions evaluated for the TS selector devices.

Table 4.1. Working conditions evaluated for the Ag active electrode-based selector devices *via* sputtering.

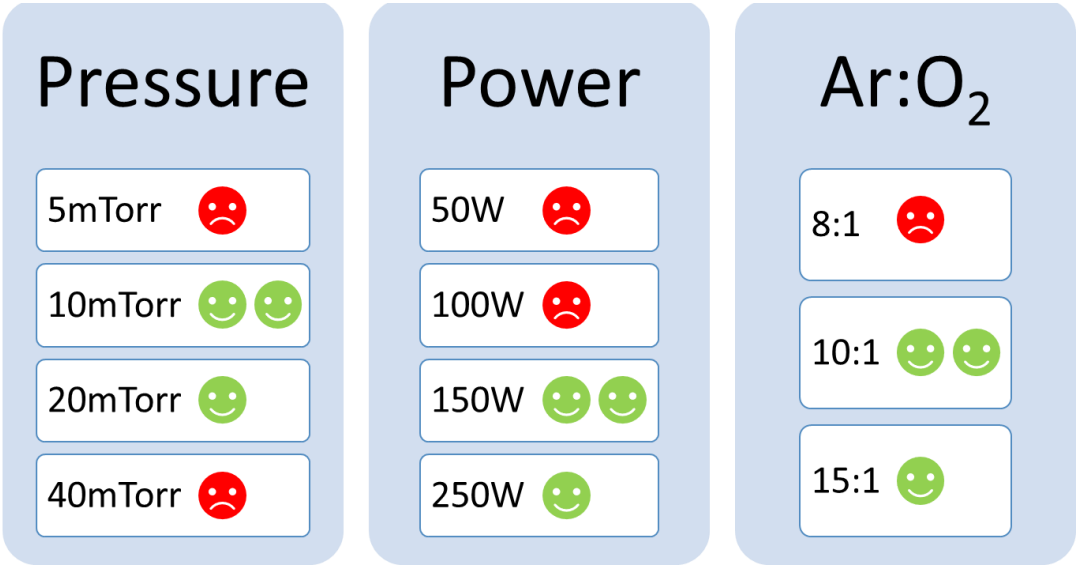

4.4 Doping Profile Engineering

As discussed in the section 4.3, the working conditions for sputtering process were first sorted out for the conventional Ag active electrode-based selector device structure. As per the obtained results, working pressure of 10 mtorr, ZnO target power at 150 W, deposition temperature at RT, and Ar:O_2 ratio of 10:1 showed the best non-volatile TS selector behavior. Next, two different doping profile *i.e.*, delta/layered doping and uniform doping were investigated, discussed in detail in the following sections.

4.4.1 Delta/layered Doping

For the demonstration of volatile switching characteristics of the TS selectors, a simple two-terminal structured delta-doped devices were fabricated in two different device sizes of 25 μm radius, and 250 nm × 250 nm nanohole structure as per experimental design. Fabrication conditions were same as previously discussed at section 4.3.1, except for that Ag was introduced as the dopant for delta doping *via* DC co-sputtering with ZnO target (Figure 4.8). For achieving the delta doped profile, sequential depositions of ZnO and Ag were made as shown in Figure 4.8, by controlling

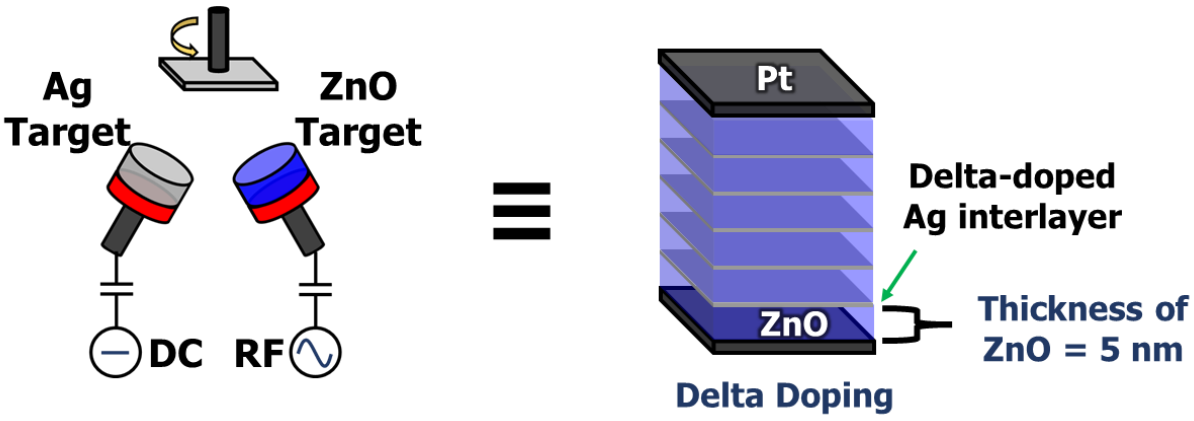

Figure 4.8. Schematic illustration of the delta doping profile showing sequential ZnO and Ag interlayers.

the thickness of each deposited layer. In this case, the ZnO interlayer thickness was kept constant at ~5 nm and Ag interlayer thickness was varied from ~0.3 nm – 0.8 nm, while the general film thickness for SL was maintained at ~30 nm. The Ag target DC power was varied from 15 W (lowest tool power) to 48 W. Two different Ar/O_2 ratios of 8:1 (Figure 4.9) and 10:1 (Figure 4.10), were investigated. Figure 4.9 displays the volatile switching characteristics of Ag delta-doped ZnO for $Ar:O_2$ = 8:1. No TS is observed when the Ag interlayer thickness is <0.8 nm. Devices show stuck-off failure *i.e.*, no filament formation happens possibly due to Ag deficiency in the ZnO SL. When Ag interlayer thickness is ~0.8 nm, TS behavior is observed but the device yield is extremely poor. Figure 4.10 displays the volatile switching behavior of the Ag delta-doped ZnO when $Ar:O_2$ = 10:1. In this case, poor TS is observed for the Ag interlayer thickness of ~0.3 nm with majority of the devices showing stuck-on failure ($I \propto e^x$) meaning the Ag amount was not sufficient for filament formation. Interestingly, when the Ag interlayer thickness was further

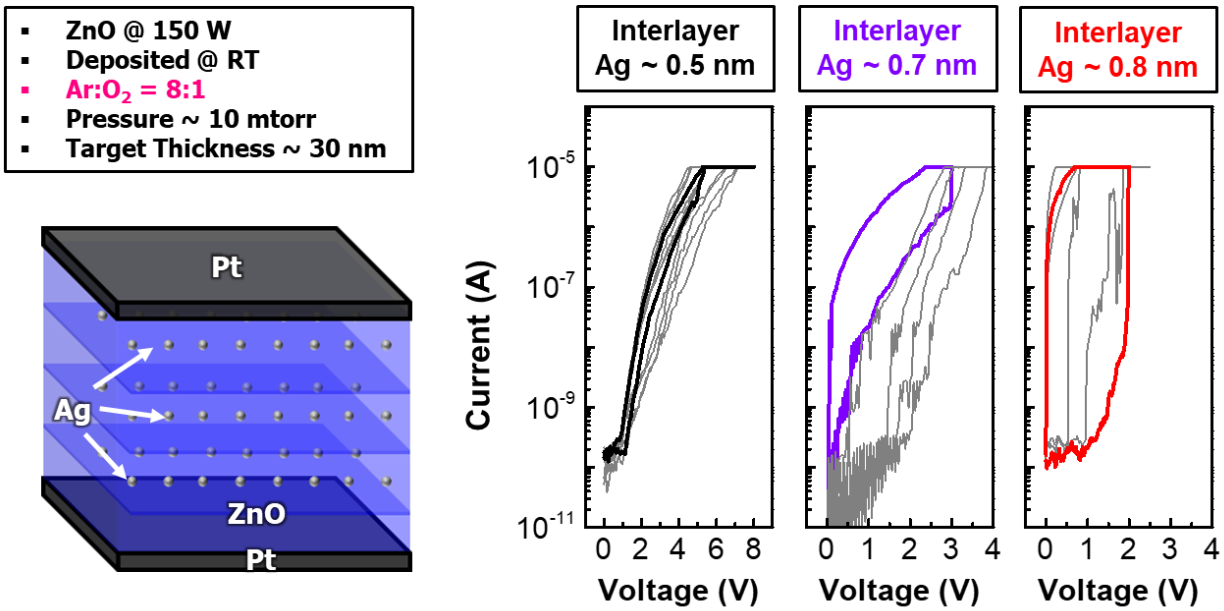

Figure 4.9. Volatile switching characteristics of the Ag delta-doped ZnO for $Ar:O_2$ = 8:1, for varied Ag interlayer thicknesses.

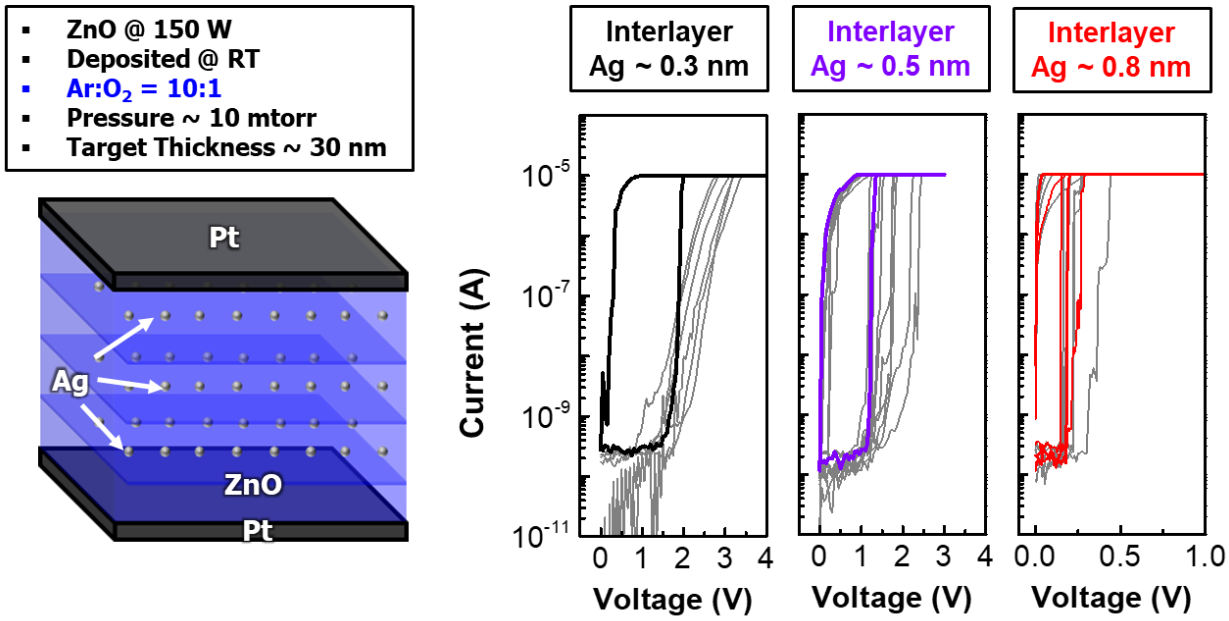

Figure 4.10. Volatile switching characteristics of the Ag delta-doped ZnO for Ar:O_2 = 10:1, for varied Ag interlayer thicknesses.

increase to ~0.5 nm, the selector devices exhibited decent TS properties with a high device yield of around ~80% and >50 DC cycling endurance. Though the devices showed a significant V_{th} fluctuation pointing towards further scope of improvement. All the devices having a thicker Ag interlayer >0.5 nm primarily showed stuck-on failure due to permanent filament formation possibly due to excessive Ag amount in the ZnO SL. The results from Figures 4.9 and 4.10 once again confirm that switching properties are better for Ar:O_2 = 10:1 case compared to Ar:O_2 of 8:1.

Finally, device scaling effect was investigated using devices sizes of 25 μm radius, and 250 nm × 250 nm nanohole structure (Figure 4.11), for Ag interlayer thickness of ~ 0.5 nm. It was observed that the scaled down devices showed enhanced filamentary formation with non-volatile memory switching instead of volatile switching. Though the exact cause for this origin is not clear

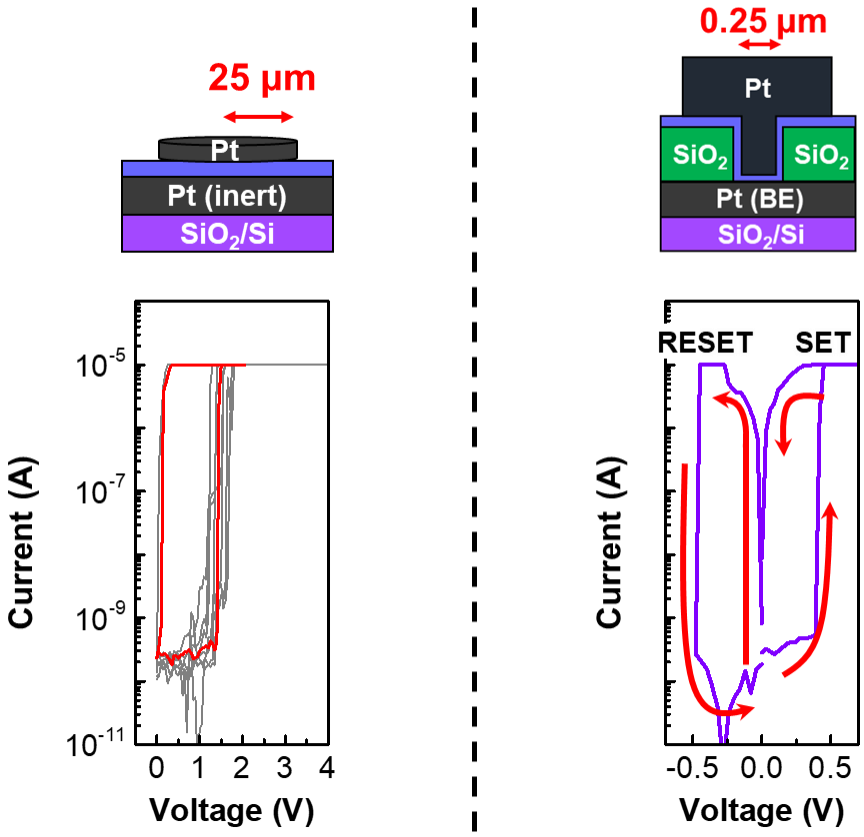

Figure 4.11. Demonstration of device scaling effect using devices sizes of 25 µm radius, and 250 nm × 250 nm nanohole structure for TS selector devices having delta-doped Ag interlayer with thickness of ~ 0.5 nm.

but two possibilities can be raised – a) Film deposition conformality issue with sputtering process when using a nanohole structure as the filament may be easily formed near the region where Ag:ZnO is thinly deposited, and b) Lessened grain boundaries effect.

To summarize, these results successfully demonstrate the delta-doped profile for restricting the Ag amount in the ZnO switching layer medium, although due to tool limitations of not having a better control on Ag interlayer thickness due to lack of tool automation capabilities, this doping profile was not further studied but could be a wonderful topic for future studies due to its interesting results.

4.4.2 Uniform Doping

Next, we demonstrated the uniform doping profile exhibiting the volatile switching characteristics for two-terminal MIM structured TS selector devices (Figure 4.12). We fabricated Ag-doped nano-polycrystalline ZnO based (Pt/Ag-doped ZnO/Pt) TS selector devices by using two different device sizes of 25 μm radius, and 250 nm via-hole structures on Si wafer. The detailed procedure for 250 nm via-hole structure fabrication has already been discussed elsewhere.[120] A Pt layer was used as the bottom contact electrode. Ag-doped ZnO served as the SL of the steep-slope TS selector devices and was deposited using ATC Orion (by AJA International) sputter deposition system. Ag doping-based amorphous ZnO SL was deposited using ZnO target (Kurt J. Lesker, 99.9 % purity) at a RF power of ~150 W and Ag target (Kurt J. Lesker, 99.9 % purity) at a DC power of ~27 W, at room temperature. Ag doping-based polycrystalline ZnO layer was deposited under same conditions except for ZnO target sputtered at ~250 W. For evaluation of Ag concentration effects, Ag doping-based polycrystalline ZnO layer was deposited at room

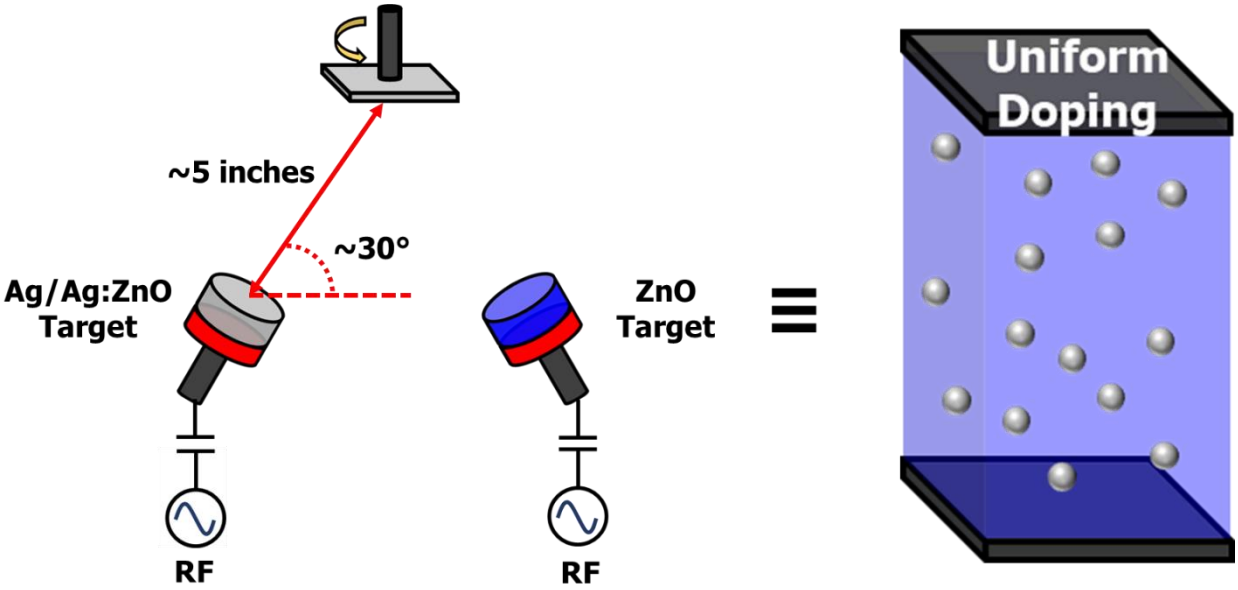

Figure 4.12. Schematic illustration of the uniform doping profile showing homogeneously doped ZnO medium with Ag.

temperature by co-sputtering ZnO target at a RF power of ~250 W and Ag:ZnO (ZnO/Ag 100-x/x x=1, 3, 10 at. %; SCI Engineered Materials, 99.99 % purity) composite target at varied RF powers (~50 W to ~150 W). Ag concentration has been tuned by adjusting Ag:ZnO composite target power. The deposition thickness for SL was ~30 nm. A 30 nm thick Pt layer was deposited via an e-beam evaporator (Temescal 1800) using a shadow mask, which served as the top contact electrode. The surface of fabricated thin films was characterized using X-ray diffraction (XRD, Rigaku SmartLab), X-ray photoelectron spectroscopy (XPS, PHI Versa Probe II), and scanning electron microscopy (SEM, Zeiss Supra 40). Keithley 4200A-SCS parameter analyzer was used to evaluate electrical properties.

First, 25 µm radius devices were fabricated under the process conditions previously discussed in section 4.3.2, *i.e.*, ZnO target power at 250 W, Ag target power of 27 W, working

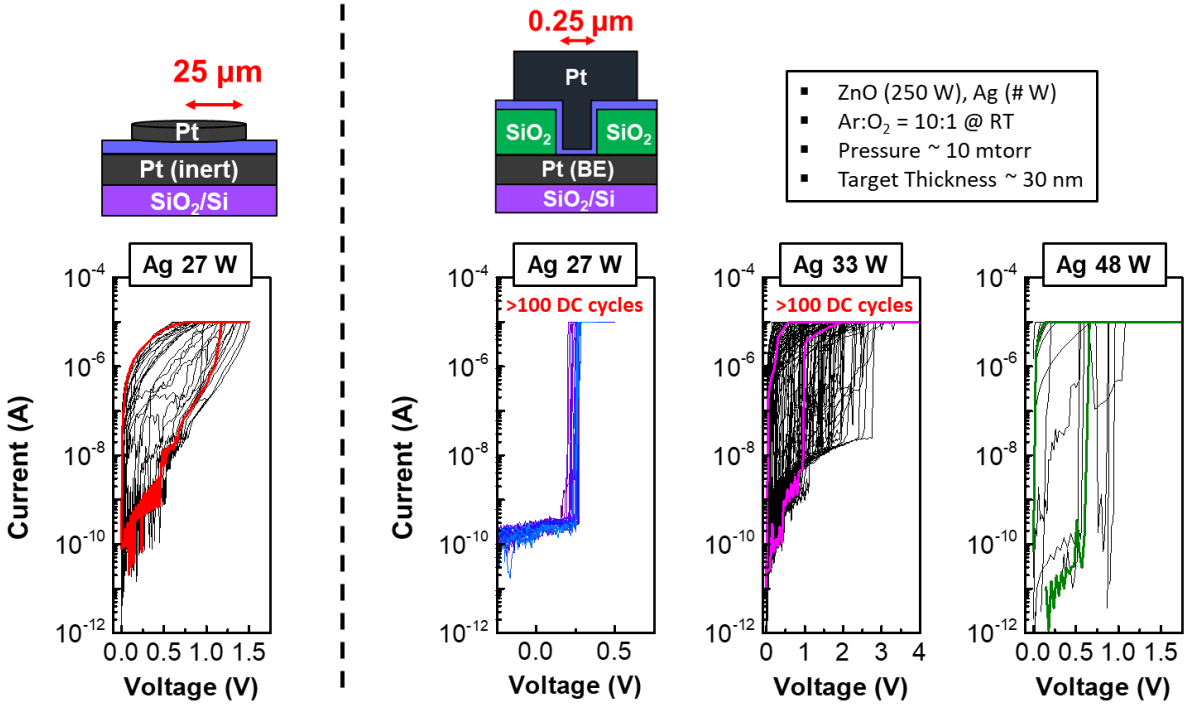

Figure 4.13. Volatile TS characteristics for uniformly doped selector devices having 25 µm radius (leftmost plot) and 250 nm × 250 nm nanohole devices at varied Ag target powers.

pressure of 10 mtorr, Ar:O_2 ratio of 10:1, and deposited at RT. Surprisingly, the devices did not show any TS but rather suffered from stuck-off failure (Figure 4.13, leftmost plot). When under the same process conditions, a scaled down device of 250 nm × 250 nm nanohole via structure was fabricated, excellent TS properties were observed. Filament formation is possibly found to enhance with device scaling due to – a) Joule heating resulting from increased current density with reduced device size, and b) localized electric field enhancement due to smaller BE contact area available for filament formation. The devices showed improved V_{th} variances of 0.4 V ± 0.2 V even in the worst-case scenario. A stable bidirectional switching operation over >100 DC cycles was observed with the off-state leakage current of ~10 fA when operated at compliance current of 100 μA displaying a ~0.1 MA/cm^2 current density and a massive I_{on}/I_{off} ratio of ~10^9. The reason for high selectivity with ultra-low off-state current is that Ag acts as a *p*-type dopant in intrinsically *n*-type ZnO thereby compensating its *n*-type nature. [126,127,201–203] When Ag target power was increased to 33 W, TS properties were still realized with good endurance of >100 DC cycles but the V_{th} variability increased significantly. On further increase of target power to 48 W, switching properties became even worse with majority of devices showing stuck-on failure mode indicating excessive Ag concentration in the ZnO SL. Potential of uniformly doped TS selector devices for Ag 27 W was further checked by performing various electrical characterizations (Figure 4.14). The co-sputtered Ag doping-based selector device exhibits reversible unipolar TS operation up to 100 μA (selectivity ~10^{10}). This corresponds to the current density of >0.1 MA/cm^2. Ultra-low leakage current (~10 fA) is also confirmed when the DUT is measured under slow integration time. Cycle-to-cycle V_{th} variation was just, ΔV_{th} ± 0.2 V. The main failure mechanism is stuck-off failure

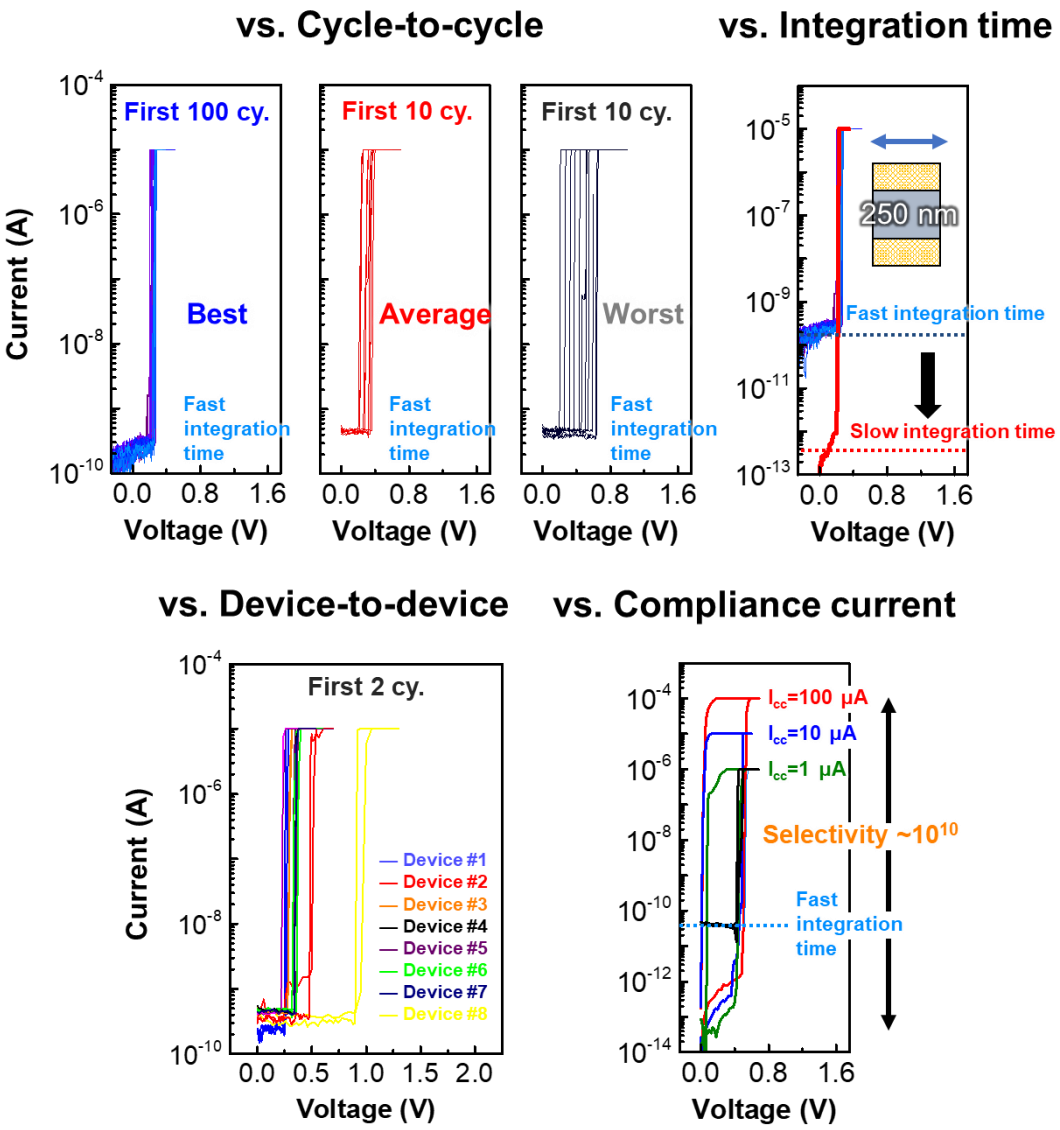

Figure 4.14. Varied electrical characterizations showing volatile switching behavior for different cases of cycle-to-cycle, integration time, device-to-device, and compliance current.

possibly due to Ag ions getting stuck at grain boundaries or forming stable Ag_{Zn}–Ag_{Zn} clustered agglomerations that further restrict filament growth. The devices could sustain more than 100 DC cycles. A good device-to-device uniformity was observed for the devices where 8 out of 12 tested devices show outstanding volatile threshold characteristics but in this scenario device #8 is considered as an outlier (V_{th} ~1 V). Remaining 2/12 devices showed memory switching and other

2/12 showed TS behavior but with I_{off} ~ 100 nA, indicating that further process optimization is required for improved device-to-device uniformity.

To properly understand the effect of Ag in supersaturated ZnO matrix, several material characterization processes were performed on the selector devices (Figure 4.15). It was expected that due to excessive silver in the selector medium, severe distortions were created in the pristine ZnO wurtzite structure, [126,127,201,202,204] which were characterized by various techniques of TEM, XPS, XRR, GIXRD and RAMAN analysis. The distortions were happening because even when Ag was introduced at the lowest possible tool power of 27 W, Ag exceeded the solubility limit of ZnO. Figure 4.15a displays the HR-TEM (cross-section) image of the co-sputtered uniformly doped ZnO SL. A poly-nanocrystalline phase for ZnO can be clearly seen in the image showing multiple orientations for ZnO crystals with a few lattice matched nanocrystals dispersed randomly throughout the film, implicating lattice distortions caused by the Ag supersaturation. Using XRR, pure ZnO gives a bulk density and theoretical value of 5.6 g/cm^3, and 5.44 g/cm^3, respectively. In our case, the Ag-doped ZnO film showed a bulk density of 5.03 g/cm^3 (Figure 4.15b). Comparing it with theoretical value, we can see that the film density has decreased. It is expected to decrease because of the increased Ag_i or Ag_O in the film rather than just Ag_{Zn}, which induces more distortions and lead to a fall in the bulk density. When Ag concentration was measured using XPS (Figure 4.15c), it turned out to be 12 at. % even for the lowest sputter target power. The lattice distortions due to Ag supersaturation were further confirmed by GIXRD (Figure 4.15d) and RAMAN (Figure 4.15e) analysis. (002) peak was found to be broadened in the GIXRD pattern indicating the presence of Ag^+ having radius of 126 pm or Ag^{2+} with 97 pm radii, inducing

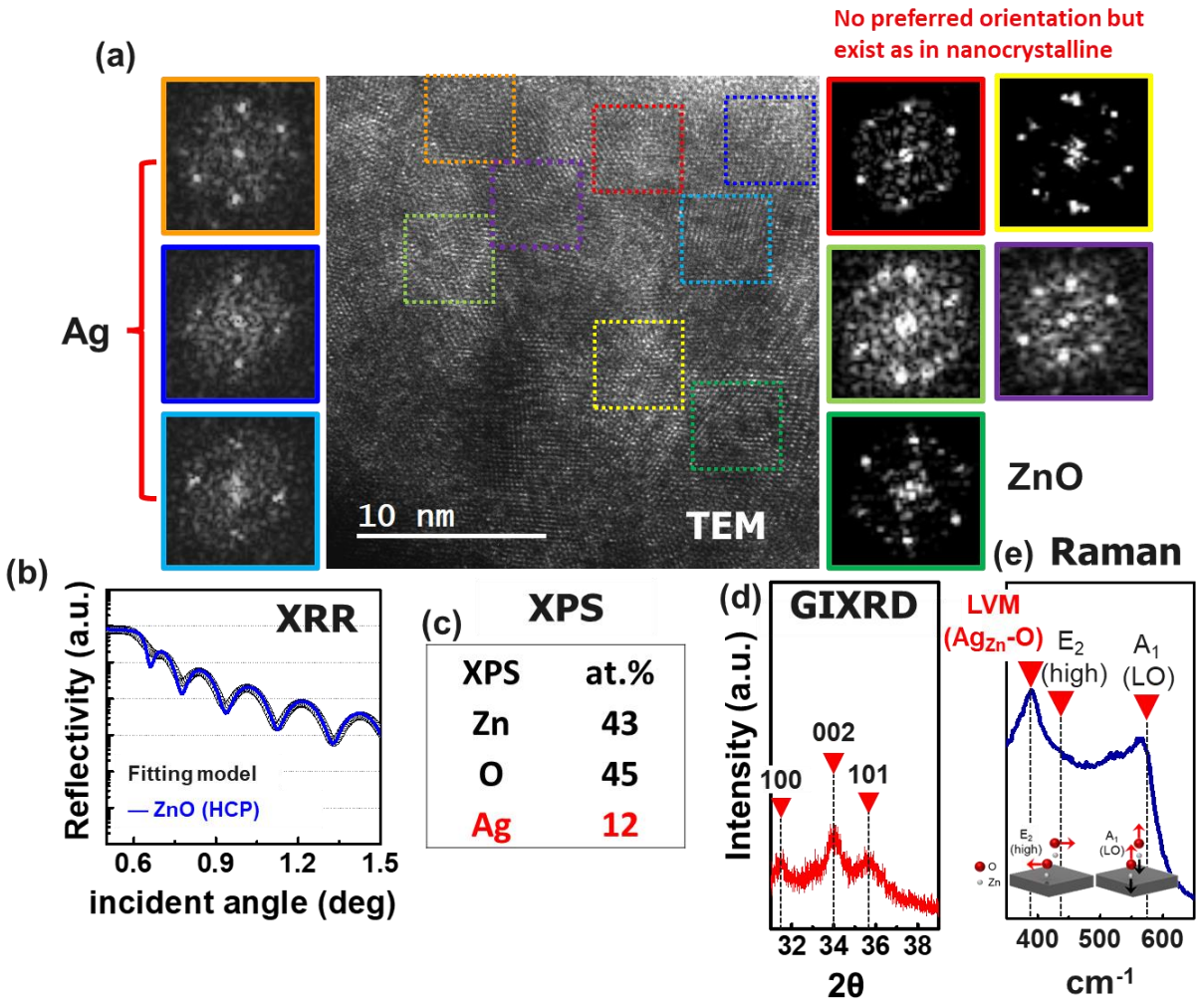

Figure 4.15. Material characterization of the Ag-doped ZnO fabricated via co-sputtering process showing, (a) HR-TEM, (b) XRR, (c) XPS, (d) GIXRD, and (e) Raman confirming induced lattice distortions.

distortions compared to Zn^{2+} (74 pm). Also, the disappearance of E_2 (high) mode in RAMAN is attributed to the lattice distortions in the crystalline ZnO structure. Moreover, local vibrational modes (LVM) were observed at 394.5/cm. [201,203,204]

Hence, efforts were made to reduce Ag concentration in the switching layer by changing the process parameters for co-sputtering system involving pure ZnO and Ag targets. As mentioned earlier that the co-sputtering process was already carried out at the lowest target power of 27 W

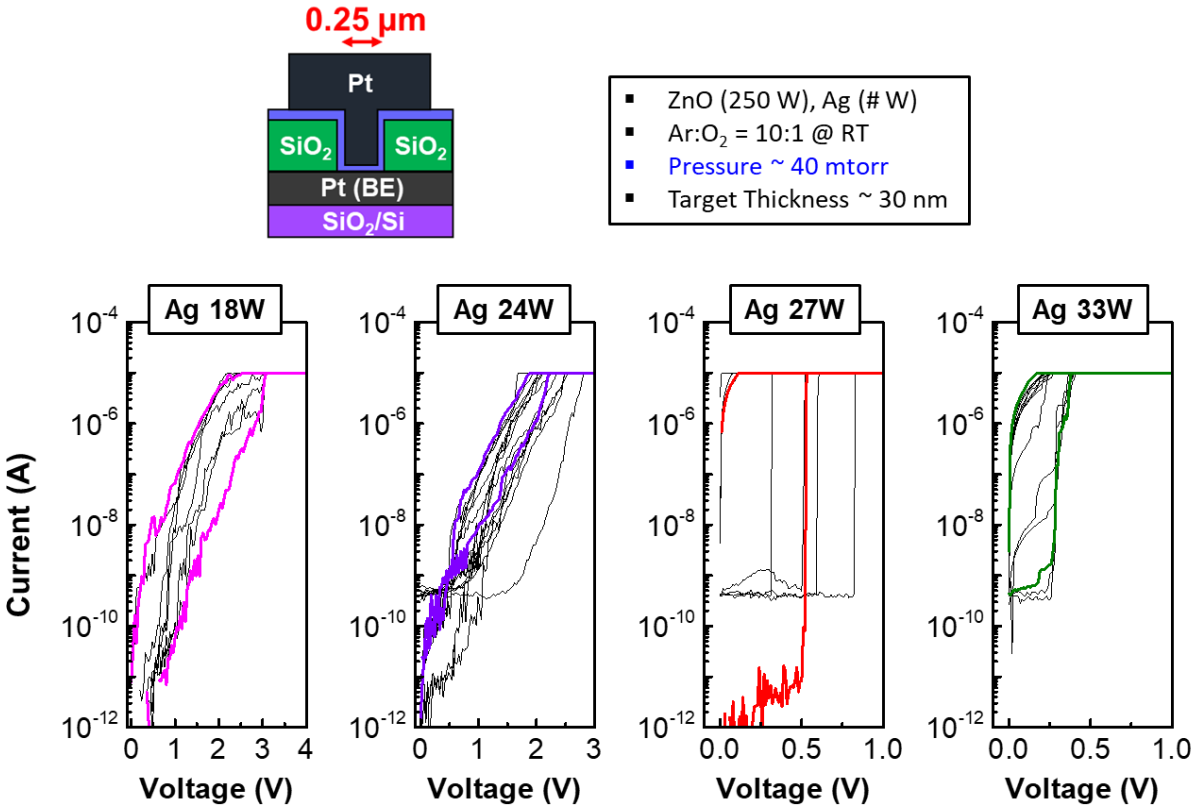

Figure 4.16. Volatile TS characteristics for uniformly doped selector devices having a working pressure of 40 mtorr, deposited at varied Ag target powers.

for the Ag target, so the only available option to achieve an even lower target power was to increase the working pressure. So, new selector devices were fabricated at a working pressure of 40 mtorr while maintaining ZnO target power at 250 W, $Ar:O_2$ = 10:1 and Ag target powers were varied as per design of experiment. As expected, with the increase in working pressure, the new lowest achievable target power was 18 W. Figure 4.16 displays the DC-*IV* characteristics of the fabricated selector devices at lower Ag target powers with an aim to reduce the Ag concentration in the film. But as evident from the *IV* behavior, none of the devices showed TS, although we were able to reduce the Ag content in film. This is possibly because we previously mentioned that selectors do not exhibit threshold switching behavior at 40 mtorr as films grow as amorphous rather than

crystalline. So, it became imperative to figure out a way to reduce Ag amount without having the need to change the deposition conditions which were producing good switching properties.

The next approach that we adopted to control Ag doping was introducing a lightly doped composite target instead of using a pure Ag target for co-sputtering. Three different composite targets *i.e.*, ZnO/Ag 90/10 at. %, ZnO/Ag 99/1 at. %, and ZnO/Ag 97/3 at. % were tested in this dissertation, respectively. Before evaluating the composite targets, we performed proof-of-test experiment to re-verify the working conditions for the case of uniform doping as shown in Figure 4.17. Three different device structures were fabricated – a) undoped ZnO with no Ag active electrode, b) undoped ZnO with Ag active electrode, and c) Ag-doped ZnO using pure Ag target with ZnO target. First the breakdown field for deposited ZnO film was calculated which turned

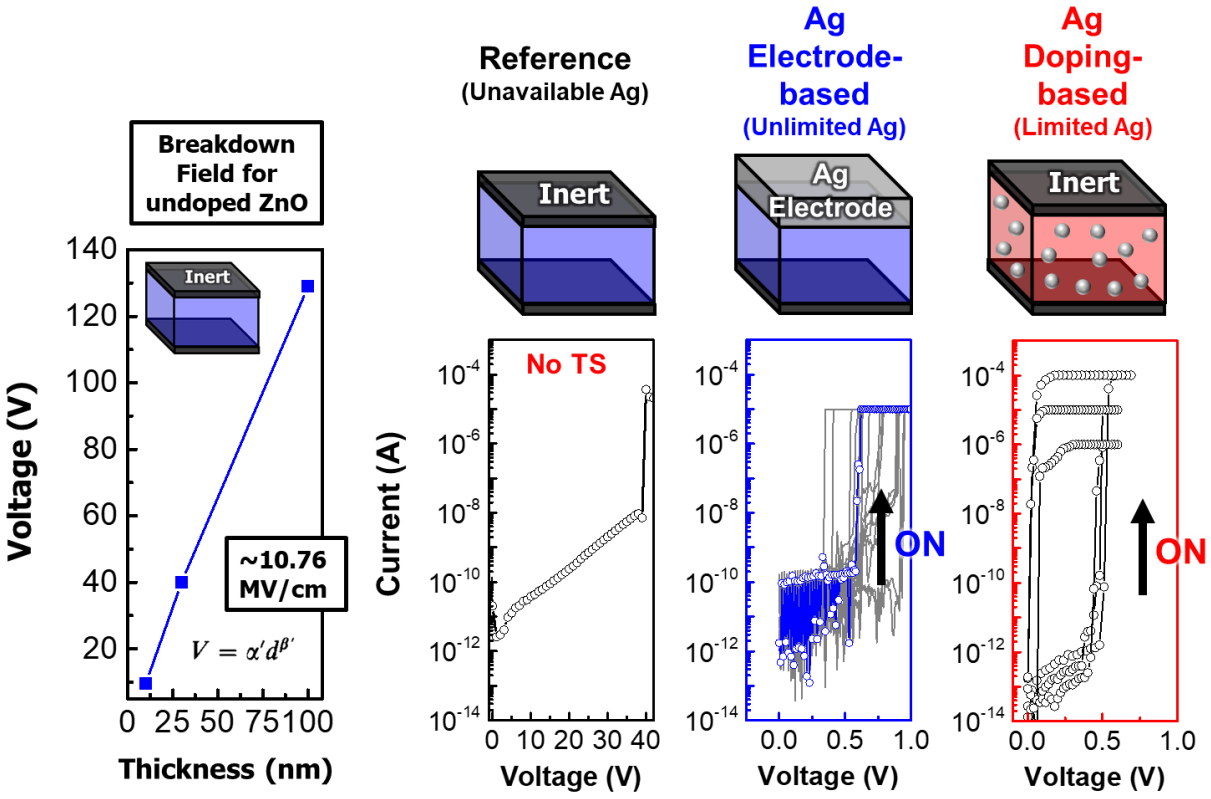

Figure 4.17. Proof-of-test experiment performed to re-verify the working conditions for the case of uniform doping.

out to be ~10.76 MV/cm which was very close the theoretical value of ~11.0 MV/cm. This means that the deposited films did not have too many defects. The devices with undoped ZnO and no Ag active electrode showed no TS behavior due to absence of Ag. The devices with undoped ZnO and Ag active electrode showed TS behavior after following electroforming (EF) process (~1-2 V) in their pristine state. Though significant amount of V_{th} fluctuations were observed with a relatively higher off-state current. The Ag-doped ZnO TS selector devices exhibited EF-free switching behavior and a low leakage current.

The first composite target evaluated was ZnO/Ag 90/10 at. %. Figure 4.18 shows the schematic process flow for Ag-doped nano-polycrystalline ZnO based TS selector device fabrication. Figures 4.18 b – c shows the cross-sectional SEM image of the TS selector device without Pt top electrode (TE), and the top-view of selector devices with TE, respectively. We did

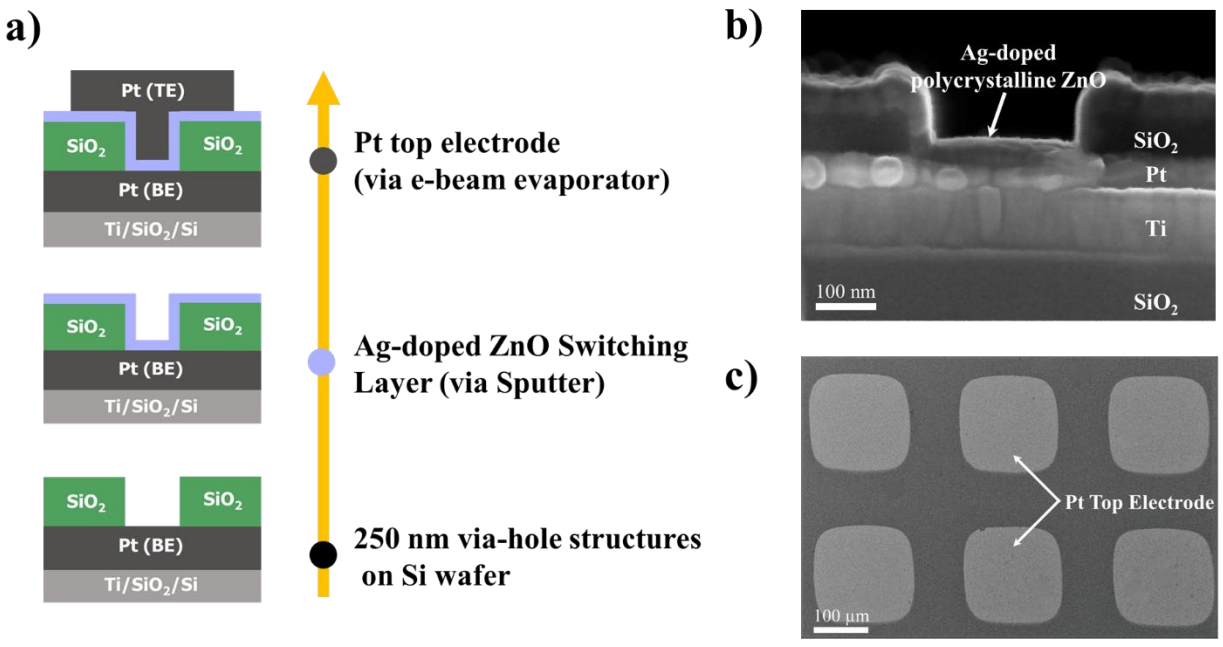

Figure 4.18. Schematic illustration of the (a) Selector device fabrication process flow, (b) Cross-sectional SEM image of Ag-doped nano-polycrystalline ZnO based threshold switching selector device, and (c) Top-view of the threshold switching selector devices with Pt top electrode.

a comparative analysis between amorphously doped and crystalline doped ZnO to further our understanding on if the crystallinity actually aids the threshold switching operation. Figures 4.19 a – b shows a comparative analysis of the volatile switching characteristics between the selector devices having an amorphous and a polycrystalline ZnO SL, respectively. For the case of Ag-doped amorphous ZnO SL, no TS behavior was observed while the Ag-doped polycrystalline ZnO based selector devices exhibited EF-free TS characteristics with a tight threshold voltage (V_{th}) distribution having V_{th} standard deviation (SD) of ± 0.05 V. These results are in good agreement with our earlier proposed hypothesis that crystalline ZnO allows facile anisotropic diffusion of Ag

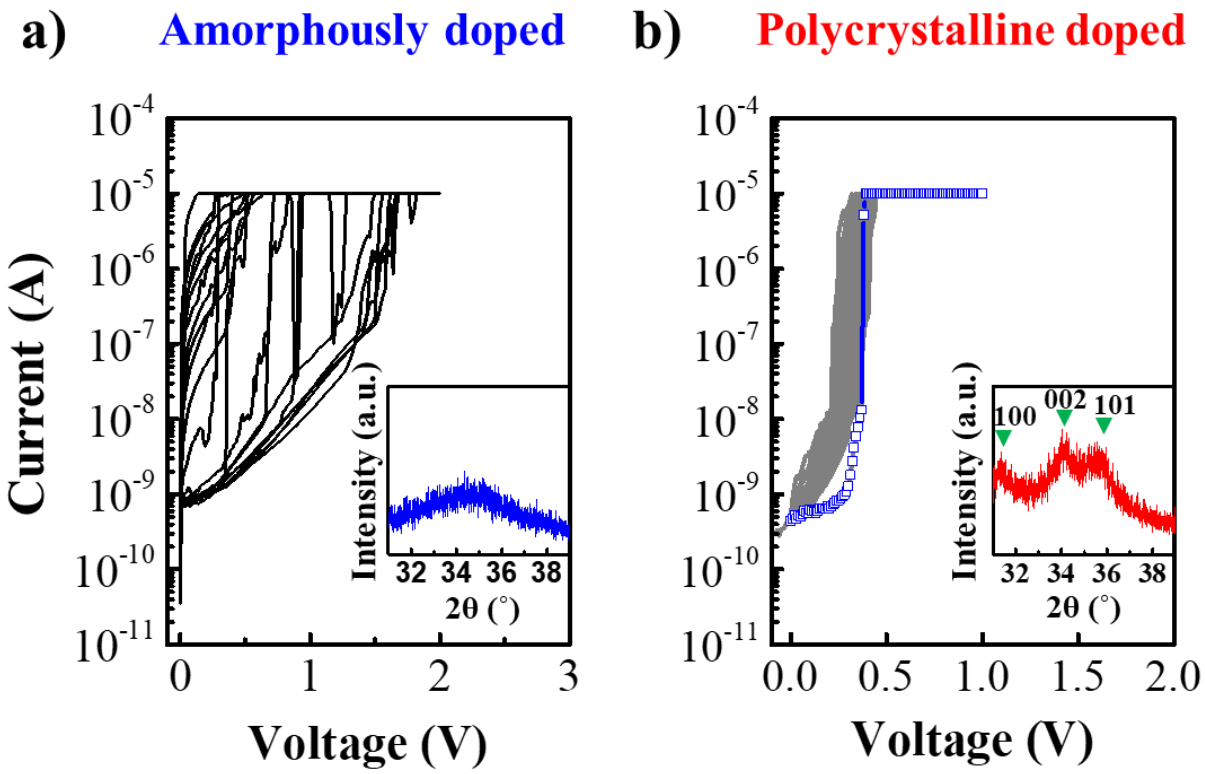

Figure 4.19. Representative volatile switching characteristics of the selector devices deposited (a) Amorphously, displaying no threshold switching characteristics, and (b) Polycrystalline, showing threshold switching characteristics (blue line represents first DC cycle); inset images show X-ray diffraction (XRD) pattern showing amorphously doped ZnO and polycrystalline doped ZnO, respectively. Ag concentration in both cases is ~12 at. %.

ions,[123,124] thereby reducing the V_{th} variabilities.[187,193] However, the Ag-doped polycrystalline ZnO based TS selector devices showed a high leakage current I_{off} (~10^{-9} A), and the presence of strong (100) and (101) peaks, inset Figure 4.19b, indicates suppressed crystallinity with no preferred orientation possibly due to higher Ag concentration of ~12 at. %, thereby giving the scope of further switching characteristics improvement by reducing the Ag doping concentration in the ZnO switching layer.

Figures 4.20 a – b demonstrates physical and chemical properties of sputtered Ag-doped polycrystalline ZnO thin films deposited with very low Ag concentrations (~1 to 3 at. %). Figure 4.20a ratifies that all the sputtered ZnO thin films, lightly doped with Ag have polycrystalline

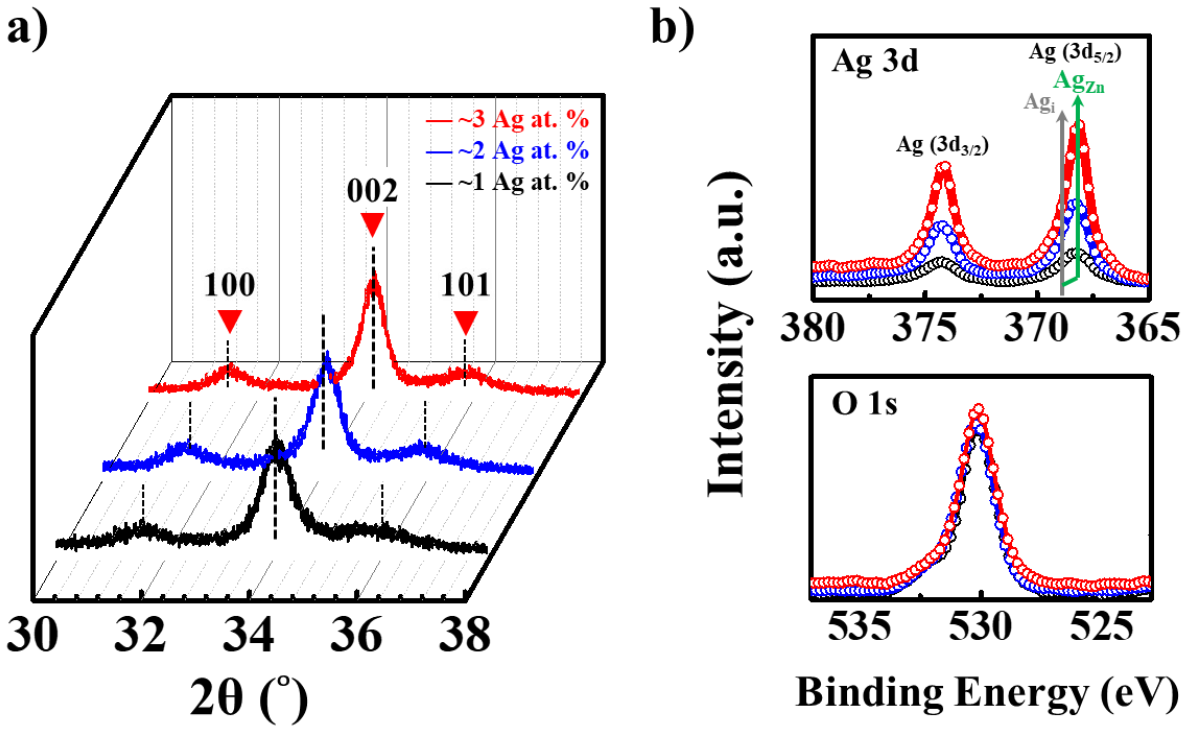

Figure 4.20. (a) X-ray diffraction (XRD) patterns showing preferred (002) orientation and, (b) X-ray photoelectron spectroscopy (XPS) spectra of the Ag $3d_{3/2}$, Ag $3d_{5/2}$ (Ag_{Zn}), and O 1s, ; of the Ag-doped ZnO films at varying Ag concentrations of ~1 at.% (black line), ~2 at.% (blue line), ~3 at.% (red line).

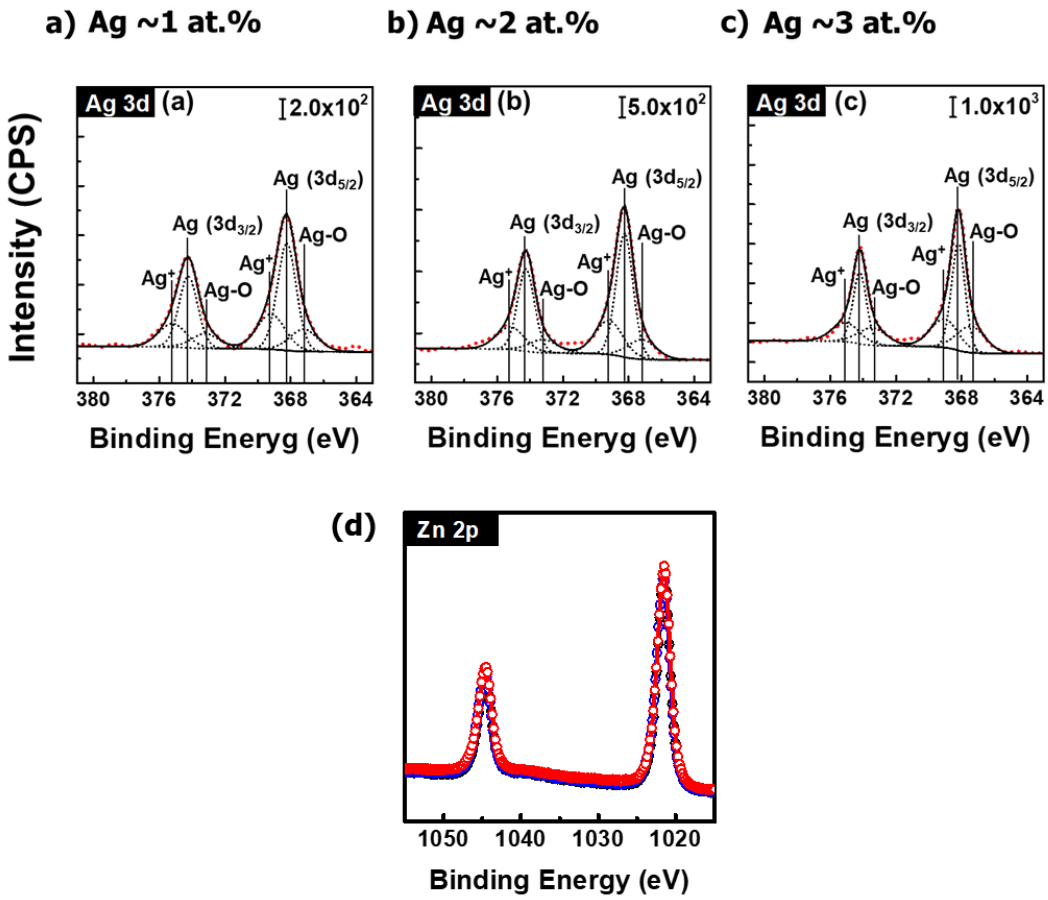

Figure 4.21. Deconvoluted XPS spectra of the Ag 3d; of the Ag-doped polycrystalline ZnO films at varying Ag concentrations of (a) ~1 at.%, (b) ~2 at.%, and (c) ~3 at.%. (d) X-ray photoelectron spectroscopy (XPS) spectra of the Zn 2p; of the Ag-doped polycrystalline ZnO films at varying Ag concentrations of ~1 at.% (black line), ~2 at.% (blue line), ~3 at.% (red line).

phase with preferred *c*-axis (002) orientation which implies that doped ZnO maintains its wurtzite structure when slightly doped even without any thermal treatment. Thus, depositing ZnO SL with low Ag concentration levels reasonably enhance the crystallinity of the SL. The lattice parameters for the Ag-doped ZnO case do not show any significant changes because of the most stable Ag substitution on the Zn site (Ag_{Zn}) dopant state as compared to Ag_O (Ag substitution on O site) or Ag_i (Ag interstitial) which induces considerable lattice distortions as per the calculations based on the density functional theory (DFT).[128] Figure 4.20b shows the XPS analysis, performed to confirm

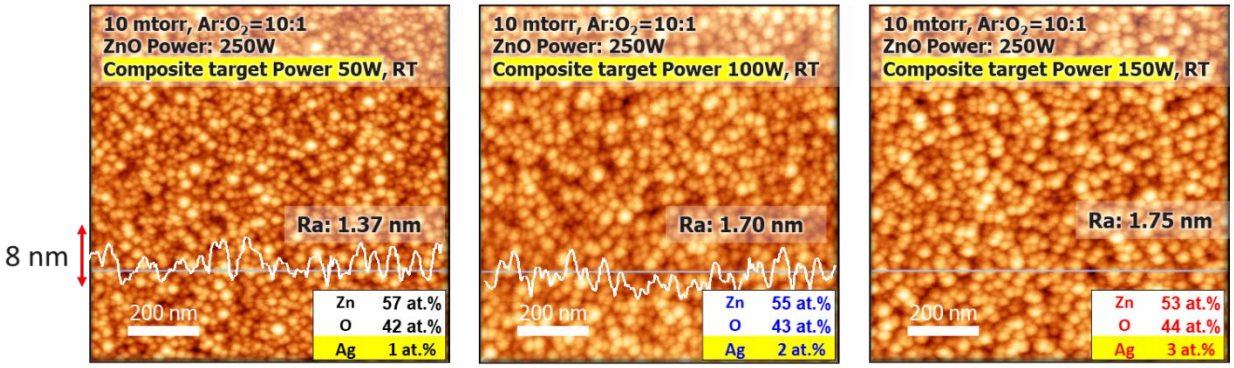

Figure 4.22. AFM images of the Ag-doped polycrystalline ZnO films at varying Ag concentrations of ~1 at.%, ~2 at.%, and ~3 at.%.

the chemical state of doped Ag in the ZnO matrix. In Ag 3d spectra, $3d_{5/2}$ peak is positioned at 368.2 eV for metallic Ag/Ag_i, whereas the binding energy for Ag^+ in Ag_{Zn} is positioned 0.5−0.7 eV lower.[128,205] The XPS analysis for Ag 3d and O 1s narrow scans shows dominant Ag_{Zn} dopant state and thus demonstrates that ZnO wurtzite structure has been successfully doped with substitutional Ag at Zn sites. XPS spectra of Zn 2p and Ag 3d are shown in Figure 4.21. Figure 4.22 shows AFM images of deposited Ag-doped ZnO films for which the lowest average film roughness was observed in Ag concentration of ~1 at. %.

Figure 4.23 shows the comparative analysis of volatile switching characteristics of non-Ag based, Ag active reservoir electrode-based and Ag-doping based steep-slope TS selectors. Direct current (DC)-voltage (*I*-*V*) sweeps measured for five different types of TS selector devices show evident characteristics. No TS behavior was observed in the non-Ag based ZnO device which is neither Ag-doped nor contains Ag active reservoir electrode (Figure 4.23a). On the incorporation of an Ag active reservoir electrode, the selector device starts exhibiting TS behavior following the EF process in its pristine state (Figure 4.23b). The device current reaches the compliance current (I_{cc}) at the voltage of 2.72 ± 0.12 V during the EF process (the initial first voltage sweep) and thereafter, the selector device continuously showed TS behavior even at a switching voltage lower

than the forming voltage. However, the TS selector device shows degraded properties in terms of high leakage current (I_{off}) of ~10^{-8} A and significant V_{th} variability (0.47 ± 0.33 V). It has been discussed earlier that I_{off} increases after EF process due to the existence of Ag clusters,[115] and V_{th} variability is observed possibly because the growth of metallic filament is a stochastic process (or random event of multiple filament occurrence).[26,47] On the other hand, I_{off} for devices having Ag-doped (~1 at. %) polycrystalline ZnO SL (Figure 4.23c), was observed to dramatically subside by ~10^4 times as compared to the TS selectors containing Ag active reservoir electrode. When Ag concentration is varied in the polycrystalline ZnO SL from 1 to 3 at. %, the I_{off} further decreases by a magnitude of 10 (Figure 4.23 c – e). The underlying phenomenon responsible for trimming down the I_{off} has been discussed in the next section.

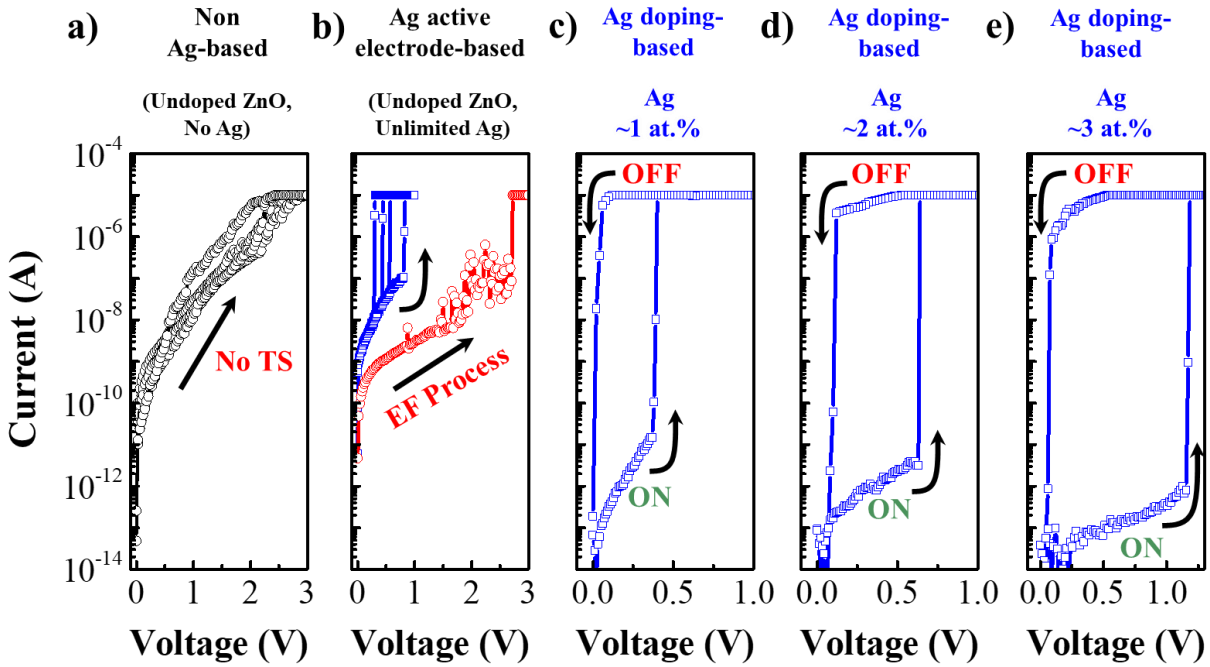

Figure 4.23. Representative volatile switching characteristics of the fabricated devices (a) non-Ag based (highly insulating state), (b) Ag active electrode-based, showing EF process and subsequent TS behavior. Volatile switching characteristics depending on Ag concentration (c) Ag ~1 at.%, (d) Ag ~2 at.%, and (e) Ag ~3 at.%, showing no EF process. The threshold voltages of (c-e) are 0.40, 0.64, and 1.18 V, respectively. Black arrows indicate the measurement direction.

Figures 4.24 a – b shows the statistical box chart for the device-to-device analysis on V_{th} and I_{off} distribution for varied Ag concentration in Ag-doping based steep-slope TS selectors. For each Ag concentration case, we tested at least 10 devices and measured a minimum of 10 DC-*IV* cycles per device. Device-to-device V_{th} (Figure 4.24a), for infinite Ag amount case *i.e.,* Ag active reservoir electrode-based TS devices display a V_{th} SD of ± 0.23 V whereas for Ag doping-based ZnO TS devices by choosing a lightly doped selector medium (~1 to 3 at. %), V_{th} SD could be minimized to ± 0.07 V. As mentioned earlier, the source of V_{th} variability in Ag active reservoir electrode-based TS devices is the stochastic nature of metallic filament nucleation process,[26,27] whereas the reduction in V_{th} variability in Ag-doping based steep-slope TS selectors case could be attributed to fewer low resistance paths available for filament growth,[47,206,207] constrained by doping. Interestingly, V_{th} (mean) was observed to increase when Ag concentration was increased from 1 to 3 at. %, for which the thermal energy involved during filament formation might be responsible, though a thorough investigation on V_{th} shifting with increasing Ag concentration is imperative for more clarity. Figure 4.24b shows extremely high I_{off} (~10 nA) for all the measured

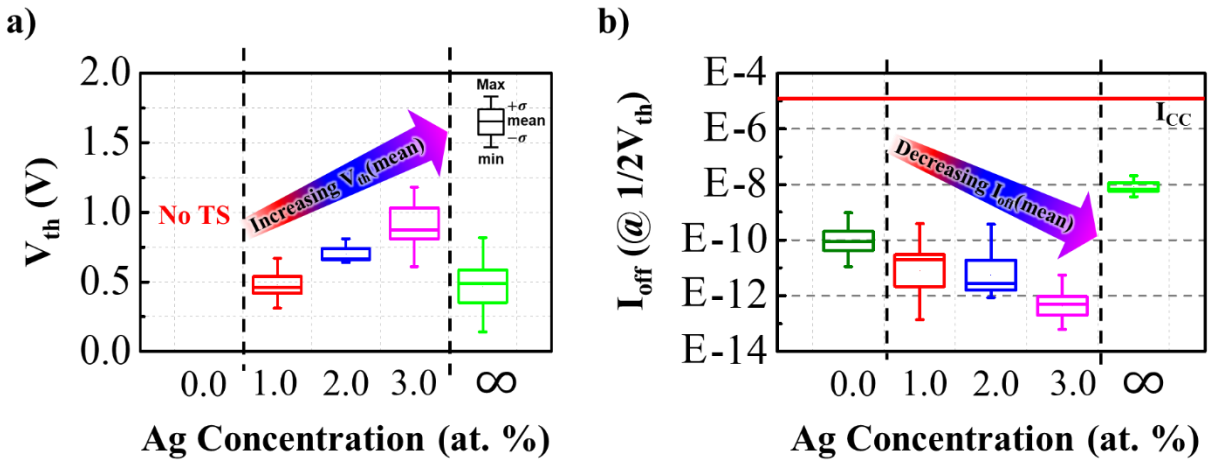

Figure 4.24. Statistical analysis box chart of (a) Threshold voltages, and (b) Leakage current, with varying Ag concentration, showing mean values, standard deviations, and min./max. outliers.

Ag active reservoir electrode-based selector devices. Whereas, for Ag-doping based steep-slope TS devices, fewer than 40% of the measured devices show a leakage current of ~0.1 nA, 20% devices showed I_{off} with a magnitude of ~10 pA, while the remaining devices exhibited an I_{off} ~1 pA or lower. This is because of the shifting of fermi-level towards the valance band edge owing to Ag_{Zn} which acts as a shallow acceptor in ZnO wurtzite structure, eventually curtailing the I_{off}.[47,125,126,128,208] Ultimately, TS selector devices with extreme-low leakage current (~10 fA), high I_{on}/I_{off} ratio (~10^8), and extremely small subthreshold swing/switching slope (< 1 mV/decade) can be realized.

Based on the DC cycling endurance studies on the Ag active reservoir electrode-based and Ag-doping based steep-slope TS devices, a noteworthy difference in number of DC cycles sustained before TS device fails, is noticed. Ag active reservoir electrode-based TS devices shows continuous stuck-ON state (*i.e.*, low resistance state) even for less than 10 DC cycles while for the

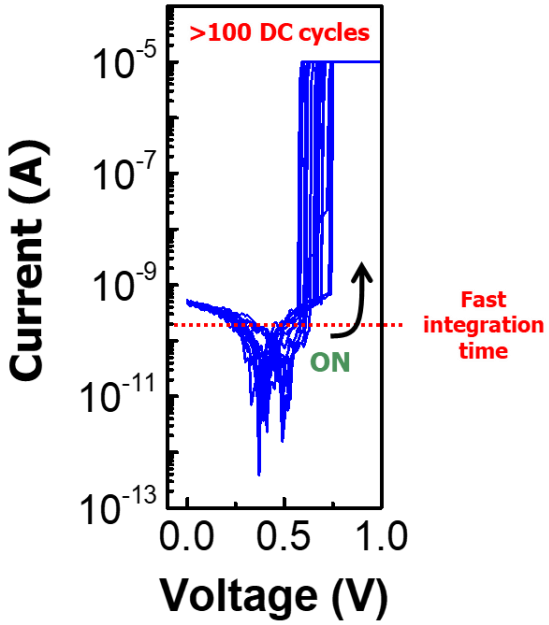

Figure 4.25. Representative single sweep volatile switching characteristics of selector devices with Ag ~1 at.% showing >100 DC cycling loops.

Ag doping-based TS devices, more than 100 consecutive DC cycles (Figure 4.25) could be acquired before the device goes into permanent stuck-ON state. For the Ag active reservoir electrode-based TS devices, the plausible explanation is, because of the unrestrained supply of Ag ions from the Ag active reservoir electrode, successive radial growth of metallic filament is easier, which leads to laterally thick and stable filament formation thereby leading to permanent stuck-ON state. Whereas, for the Ag doping-based TS devices, the radial growth of metallic filament is subdued by slight doping of Ag in polycrystalline ZnO selector medium.

The final regime tested for this composite target was the effect of switching layer thickness on the TS characteristics. Figure 4.26 shows the DC-*IV* characteristics for three different SL

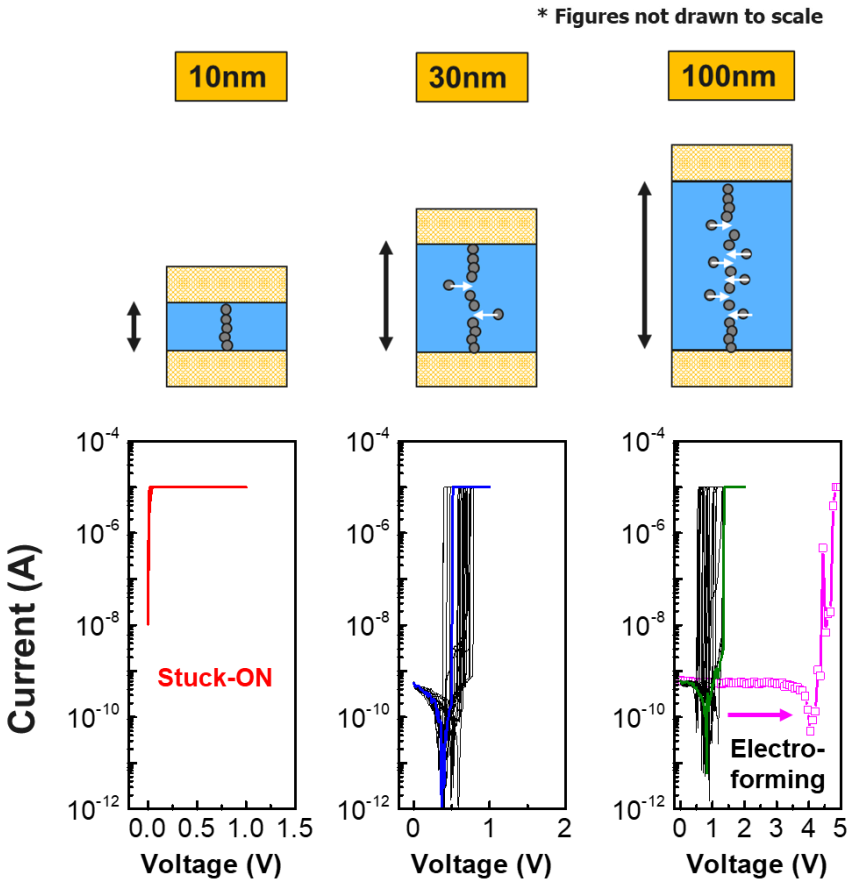

Figure 4.26. DC-*IV* characteristics of TS selector devices with SL thicknesses of 10 nm, 30 nm, and 100 nm, respectively.

thicknesses of 10 nm, 30 nm, and 100 nm. For the lowest thickness of 10 nm, no TS behavior is observed. The devices immediately showed stuck-on failure due to quick and permanent filament formation on the application of voltage bias. Excellent TS characteristics were obtained for the SL thickness of 30 nm where the devices could be swept more than 100 DC cycles with a tight V_{th} distribution and no significant degradation in device performance. When SL thickness was further increased to 100 nm, TS behavior was observed but the devices needed electroforming (~ 4–5 V) in their pristine state before they show switching properties. Moreover, the devices showed a significant V_{th} fluctuation in this case possibly due to difficulty in filament formation due to increased distance between TE and BE and reduced probability for Ag ions to connect. This event has been explained using a numerical approach as discussed below.

Some assumptions were made for numerical calculations simplicity – a) only single strand of filament is formed, and b) every ZnO crystalline SL contributes only one Ag atom to filament formation.

Let's assume a system of 'n' ZnO layers

Probability (Switching ON) $= \frac{Favorable\ Outcomes}{Total\ Number\ of\ Outcomes}$

Number of favorable outcomes (Switching ON) = 1

(∵ Switching ON happens when all Ag atoms gather to form the filament)

Total number of outcomes = Favorable + Non-Favorable Outcomes

= 1 + (Total cases when 1 Ag atom is missing) + (Total cases when 2 Ag atoms are missing) + (Total cases when 3 Ag atoms are missing) +...

$= 1 + {}^{n}C_1 + {}^{n}C_2 + {}^{n}C_3 + ...$

Probability (Switching ON)$_n$ $= \frac{1}{1 + {}^{n}C_1 + {}^{n}C_2 + {}^{n}C_3 + ...}$

Probability (Switching ON)$_2$= $\frac{1}{4}$, Probability (Switching ON)$_3$= $\frac{1}{8}$,

Probability (Switching ON)$_4$ = $\frac{1}{16}$ ....

Probability (Switching ON)$_n$ = $\frac{1}{2^n}$

Thus, this numerical approach shows that with the increase in ZnO switching layer thickness or ZnO layer by 'n', the probability for filament formation decreases by a factor of 'n'. Hence, this explanation justifies our previously obtained *IV* behavior for SL thickness study.

To summarize our findings for composite target ZnO/Ag 90/10 at. %, we fabricated a doping-based polycrystalline metal-filament type TS selector which facilitated enhanced control on filament formation due to the restricted availability and anisotropic diffusion of Ag ions in the polycrystalline ZnO SL. TS characteristics were found to be improved compared to the selector devices with amorphous ZnO SL. The effects of Ag concentration with respect to I_{off} were investigated for the Ag doping-based TS selectors having different Ag concentrations. An impressive 99.99% reduction in I_{off} is observed when Ag is introduced as a dopant in the polycrystalline ZnO matrix which is attributed to Ag that serves as a *p*-type dopant thus balancing the intrinsically *n*-type nature of ZnO, lowers down the I_{off}. In addition, doping the selector medium eliminates the requirement for EF which otherwise leads to degraded device performance as evident from Ag active reservoir electrode-based TS selectors where EF is vital. I_{off} for Ag doping-based (~1 at. %) TS selectors, was found to be reduced by an order of 4 as compared to the Ag active reservoir electrode-based TS selectors. By varying the Ag concentration from 1 to 3 at. %, the I_{off} further tends to drop by one order and an I_{on}/I_{off} ratio of ~10^8 can be achieved. Moreover, device-to-device V_{th} distribution for Ag doping-based TS shows merely ± 0.07 V of SD. The

reduced V_{th} variability is ascribed to only a few low resistance paths available for filament growth. It has been demonstrated that with Ag doping approach, DC cycling endurance could be augmented as doping strictly confines the Ag concentration in the ZnO SL, thus impeding the successive growth for metallic filament. Additionally, it was noticed that doping-based polycrystalline SL could potentially help in providing a better control over V_{th} for TS devices. Finally, we demonstrated the SL thickness effect where the TS selectors with 30 nm SL thickness exhibited the best device performance.

The major challenge encountered in the case of ZnO/Ag 90/10 at. % composite target was that the Ag concentration could not be decreased below 1 at. % due to tool limitations. Also, from the GIXRD pattern analysis (Figure 4.20), the presence of (100) and (101) peaks show scope of further process improvement to obtain (002) dominant peak only to have *c*-axis preferred orientation as desired. So, in order to go further below 1 at. % of Ag concentration, we next tested an extremely lightly doped composite target – ZnO/Ag 99/1 at. %.

Two-terminal selector devices were fabricated using composite target of ZnO/Ag 99/1 at. %. The fabrication conditions are same as mentioned previously for ZnO/Ag 90/10 at. % composite target. Figure 4.27 shows the volatile switching characteristics for the selector devices fabricated with co-sputtering pure ZnO (250 W, RF) and ZnO/Ag 99/1 at. % composite target (varied RF powers). For the lowest tool power of 30 W, the devices show TS behavior after EF process with a relatively high off-state current of ~10^{-9} A. Similar behavior was observed for higher target power of 60 W. In both the cases the device yield was also poor (~10 %). When target power was further increased, the devices immediately showed stuck-on failure *i.e.*, permanent filament formation (*data not shown*). To understand this behavior, material characterization was performed

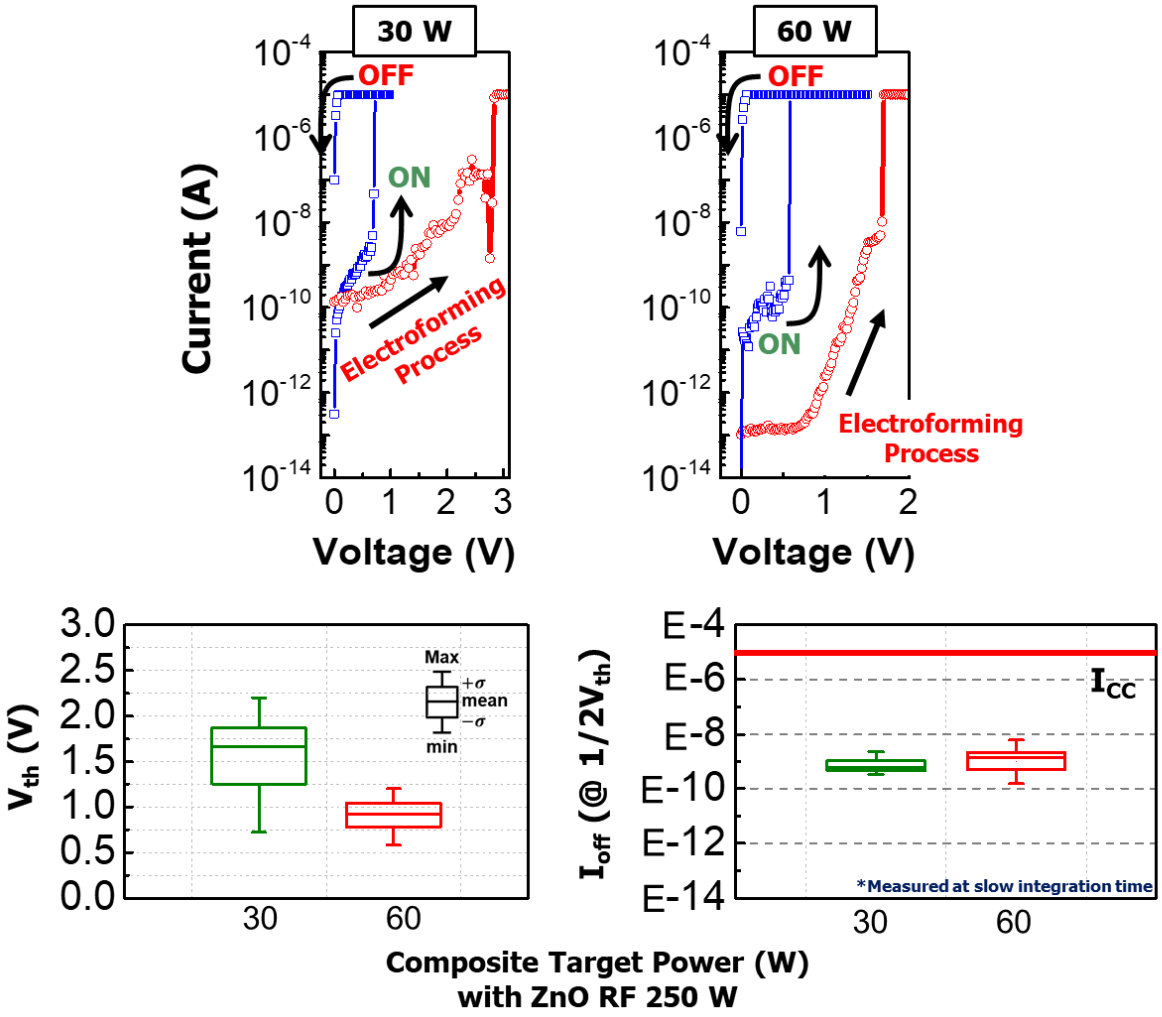

Figure 4.27. Volatile switching characteristics for the selector devices fabricated with co-sputtering pure ZnO (250 W, RF) and ZnO/Ag 99/1 at. % Composite target at 30 W and 60 W, respectively.

shown in Figure 4.27. AFM images shown in Figure 4.27a show least average roughness for 60 W case indicating high crystallinity as compared to other deposition conditions for target power, confirmed by GIXRD plot (Figure 4.27b) and (002) crystallite size (Figure 4.27c). Since, EF process was required in all the working conditions, implicating insufficient Ag amount in the SL and thus initial EF process was required to gather all the Ag ions for filament formation. XPS study was conducted to estimate the Ag concentration in the films, but it was found that Ag was under

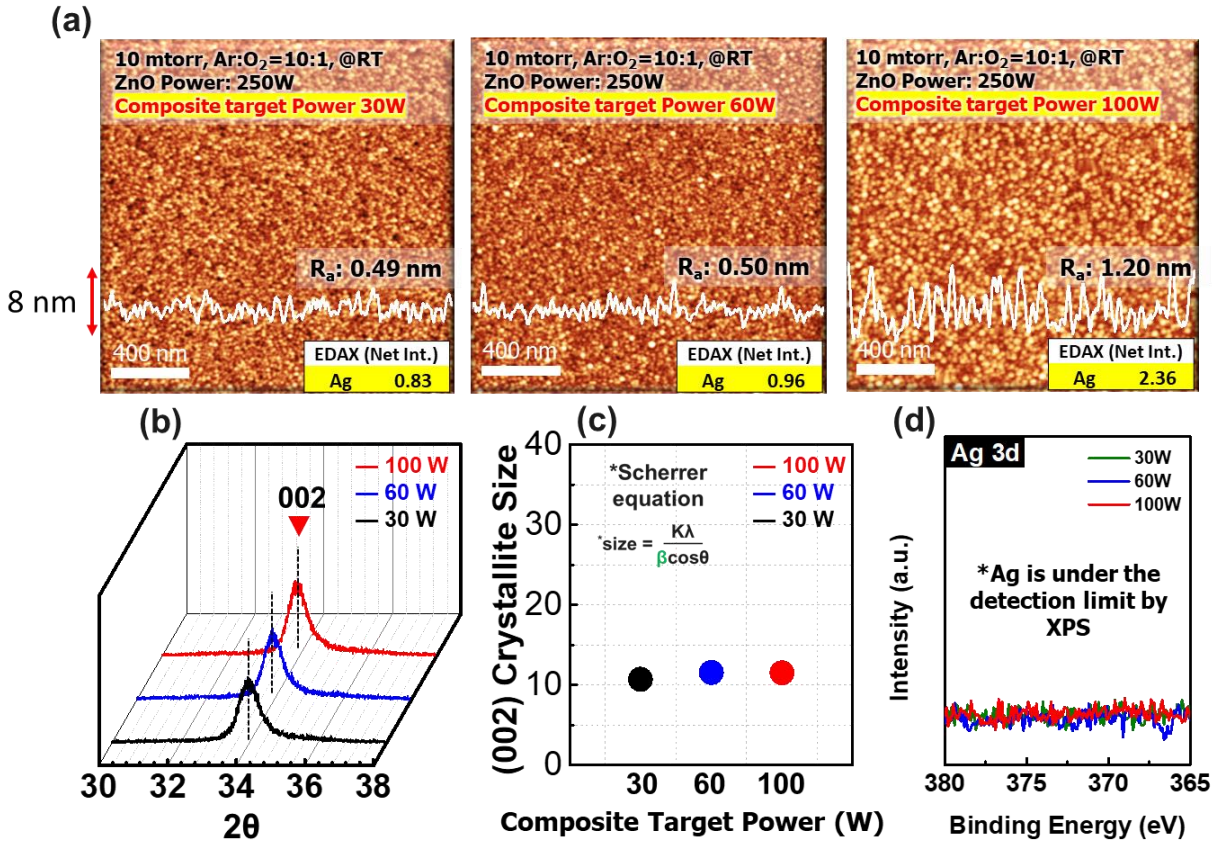

Figure 4.28. Material characterization for the selector devices fabricated with co-sputtering pure ZnO (250 W, RF) and ZnO/Ag 99/1 at. % Composite target at 30 W and 60 W showing, (a) AFM, (b) GIXRD, (c) (002) crystallite size, and (d) XPS spectra, respectively.

the detection limit for the tool (~1 %), Figure 4.27d. So, it is highly probable that we went too low on the Ag concentration in an attempt to reduce the net Ag amount in the film which needed to be further rectified. It is notable from the results that if Ag concentration is too low in the ZnO matrix, then preferred *c*-axis orientation can be obtained without any other visible peaks, but it is obligatory to extensively study the optimum Ag concentration to achieve preferred orientation without the need of electroforming.

The last composite target studied in this dissertation is the ZnO/Ag 97/3 at. %, having Ag doping in between the previously studied targets with 10 at. % and 1 at. % Ag doping

concentrations, respectively. Where 10 at. % doped target had excess Ag amount issues, the devices fabricated with 1 at. % target were Ag deficient. We fabricated Pt/Ag-doped ZnO/Pt stacked nanoscale TS selector devices utilizing 250 nm via-hole structures,[120] where Pt served as the bottom electrode (BE). A 30-nm-thick Ag-doped ZnO SL was then deposited using RF magnetron co-sputtering process at RT. For SL deposition, a pure ZnO target (Kurt J. Lesker, 99.999% purity) at 250W, RF source and a composite target – Ag:ZnO (ZnO/Ag 97/3 at. %; SCI Engineered Materials, 99.99% purity) at varied RF powers were co-sputtered. Ag-doping concentration in the SL was controlled by varying Ag:ZnO composite target power. Finally, a 30-nm-thick Pt top electrode (TE) was deposited *via* an e-beam evaporator (Temescal 1800) using a shadow mask. The surface morphology was characterized by scanning electron microscopy (SEM, Zeiss Supra 40) and X-ray diffraction (XRD, Rigaku SmartLab). Zn/Ag concentration was measured using ICP-MS (Perkin-Elmer SCIEX Elan 6100 DRC). All the electrical measurements were performed using Keithley 4200A-SCS parameter analyzer and AC pulse measurement setup using a pulse generator and an oscilloscope.

Figure 4.29 shows the COMSOL simulation results for the proposed anisotropic diffusion of Ag inside the crystalline ZnO matrix. It shows the in-plane (x-y plane) motion of Ag ions under the applied bias in z-direction. Figure 4.30 shows the comparative DC *I-V* analysis of volatile switching behavior of the selector devices. No TS characteristics were observed in the selectors fabricated at the lowest composite target power of 20 W (Figure 4.30a), due to the absence of Ag (confirmed by ICP-MS analysis) which is expected not to be effectively sputtered out at the lowest tool power. On increasing composite target power to 25 W (~0.097 at. % Ag concentration, Figure 4.33), selectors showed TS behavior after EF process in their pristine state with a relatively higher

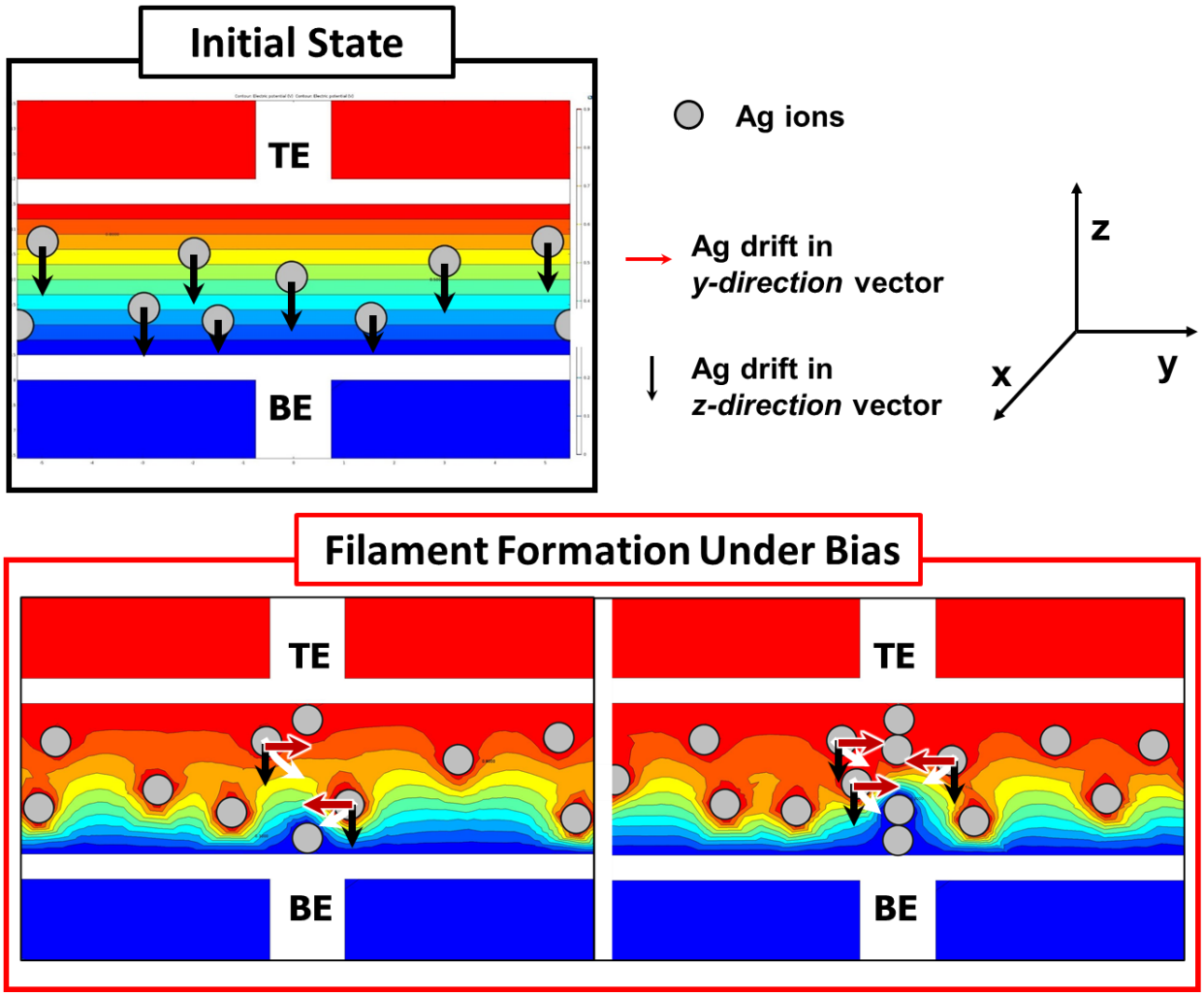

Figure 4.29. COMSOL simulation results showing anisotropic diffusion of Ag ions inside the crystalline ZnO matrix, near the filament.

off-state current (I_{off}) of ~10^{-11} A, Figure 4.30b. Jeong *et al.*[115] have also shown similar behavior of I_{off} increase following EF process, in Pt/Ag-doped HfO_x/Pt structure, due to formation of Ag clusters, thus making EF process undesirable. When composite target power was further raised to 30 W (~0.14 at. % Ag concentration), EF-free TS behavior was observed with ~10 fA I_{off}, and a high device yield of ~90 % *for devices fabricated in academic common user lab environment*, Figure 4.30c. It is noteworthy that EF-free selectors showed 3 orders of magnitude I_{off} reduction

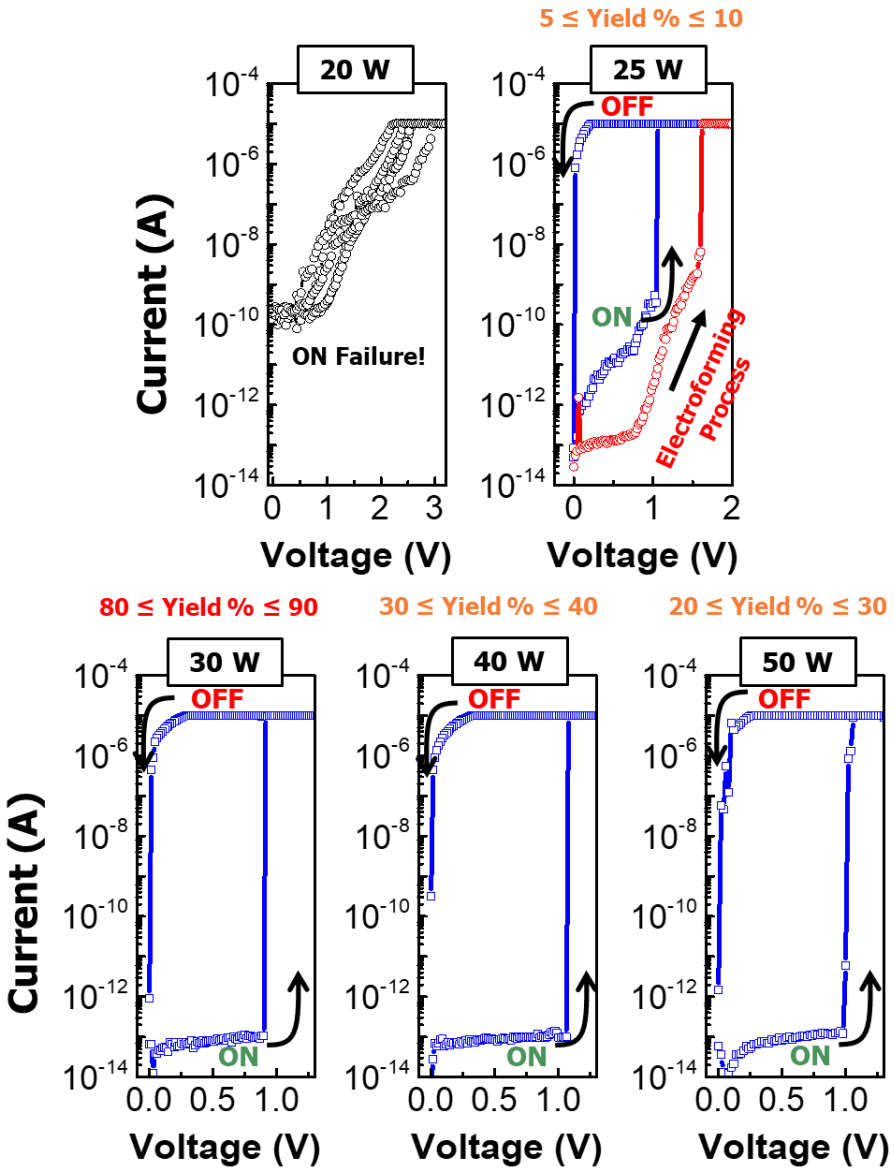

Figure 4.30. Representative volatile switching characteristics of selector devices, with ZnO/Ag (97/3 at. %) composite target power at (a) 20 W, stuck-OFF state showing no TS, (b) 25 W, EF process and subsequent TS behavior, (c) 30 W, high-yield EF-free TS behavior, (d) 40 W, low-yield EF-free TS, and (e) 50 W.

as compared to devices that needed EF. The selectors continued to show EF-free TS when composite target power was increased to 40 W (~0.19 at. % Ag), Figure 4.30d, but the device yield significantly dropped to ~30 %. This is expected to happen because the crystallinity dropped

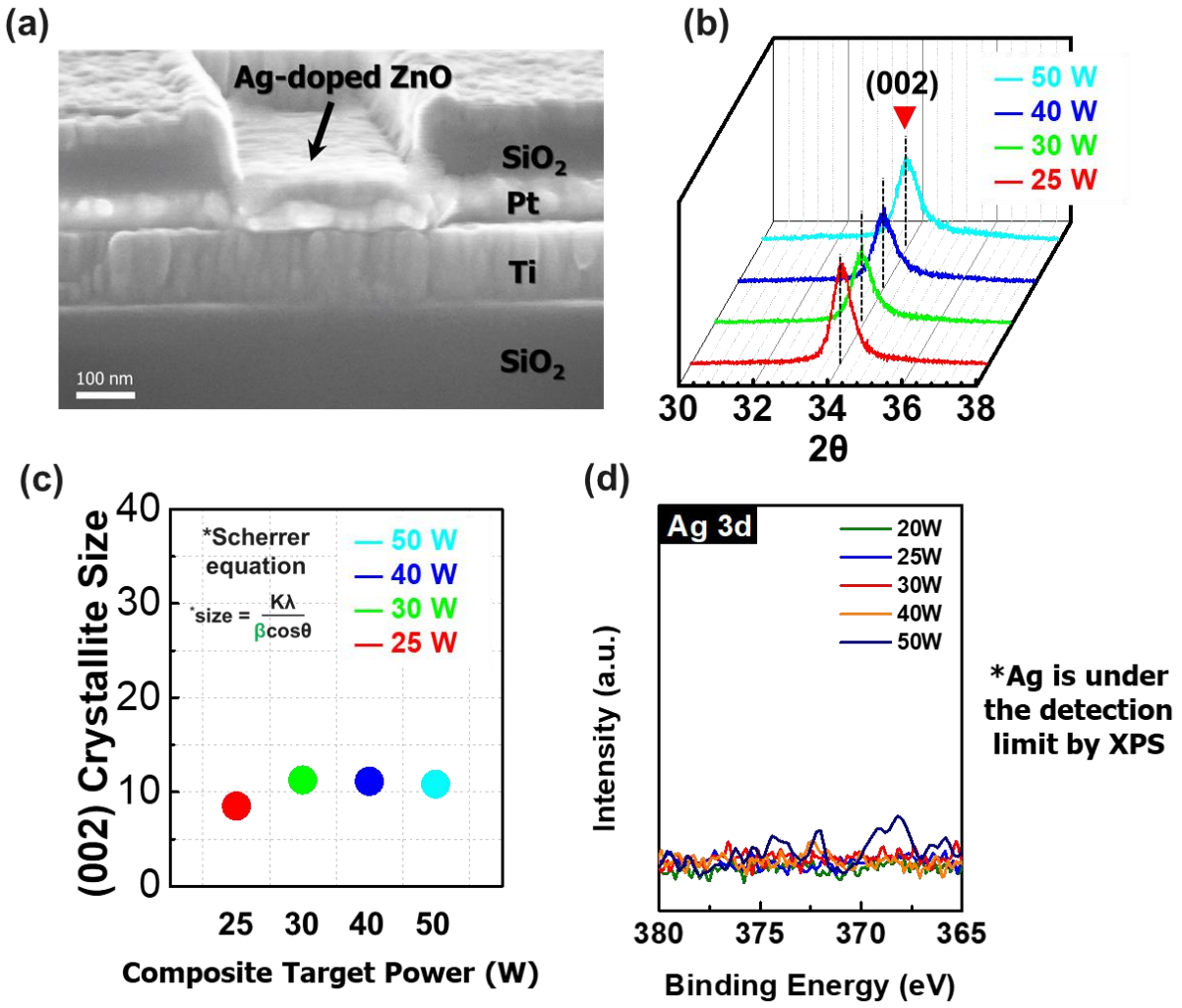

Figure 4.31. Material characterization for the selector devices fabricated with co-sputtering pure ZnO (250 W, RF) and ZnO/Ag 97/3 at. % Composite target at varied powers, showing (a) cross-sectional SEM, (b) GIXRD, (c) (002) crystallite size, and (d) XPS spectra, respectively.

by ~12.55 % per GIXRD results (Figure 4.31b) when Ag concentration increased from ~0.14 at. % to ~0.19 at. %. The increased Ag amount possibly created lattice distortions in the wurtzite ZnO matrix, thus reducing the crystallinity, and causing an immediate degradation in selector performance. Figure 4.31 shows the cross-sectional SEM image, XRD spectra, (002) crystallite size and XPS analysis, respectively. AFM images (Figure 4.32) show the highest crystallinity for 30 W case which shows significant improvement as compared to our previous best case of Ag:ZnO

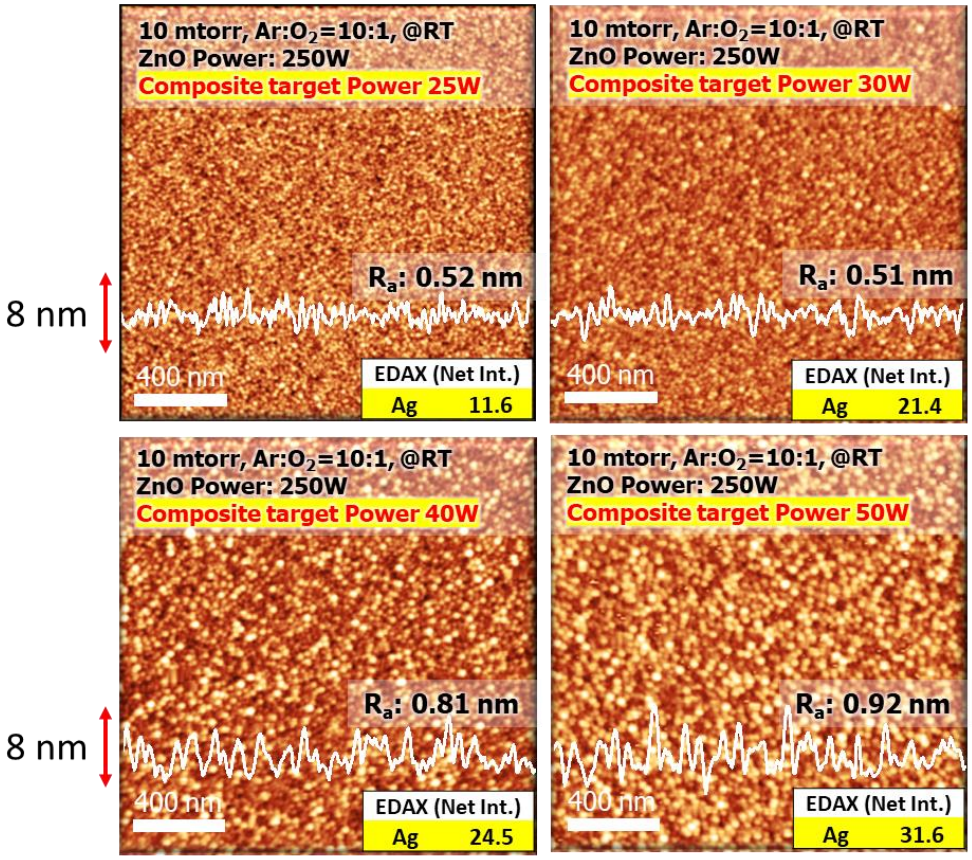

Figure 4.32. AFM images for the selector devices fabricated at varied target powers for ZnO/Ag 99/1 at. % Composite target.

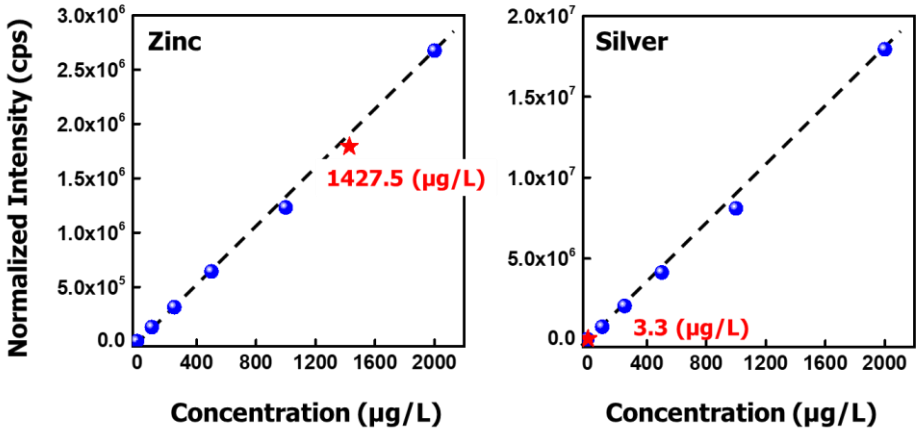

Figure 4.33. ICP-MS analysis for estimating Zn and Ag concentration, for composite target power of 25 W.

50W Ag 10 at.% doping, with ~5 % increase in grain size and ~63 % reduction in film roughness.

Since, the Ag concentration was under tool detection limit, so ICP-MS analysis was performed to estimate Zn/Ag concentration.

The potential of proposed doping-based polycrystalline ZnO-based TS selector was further evaluated by performing varied electrical characterizations (Figure 4.34). Figure 4.34a shows TS behavior of same device as in Figure 4.30c by changing compliance current (I_{cc}) levels from 1 µA

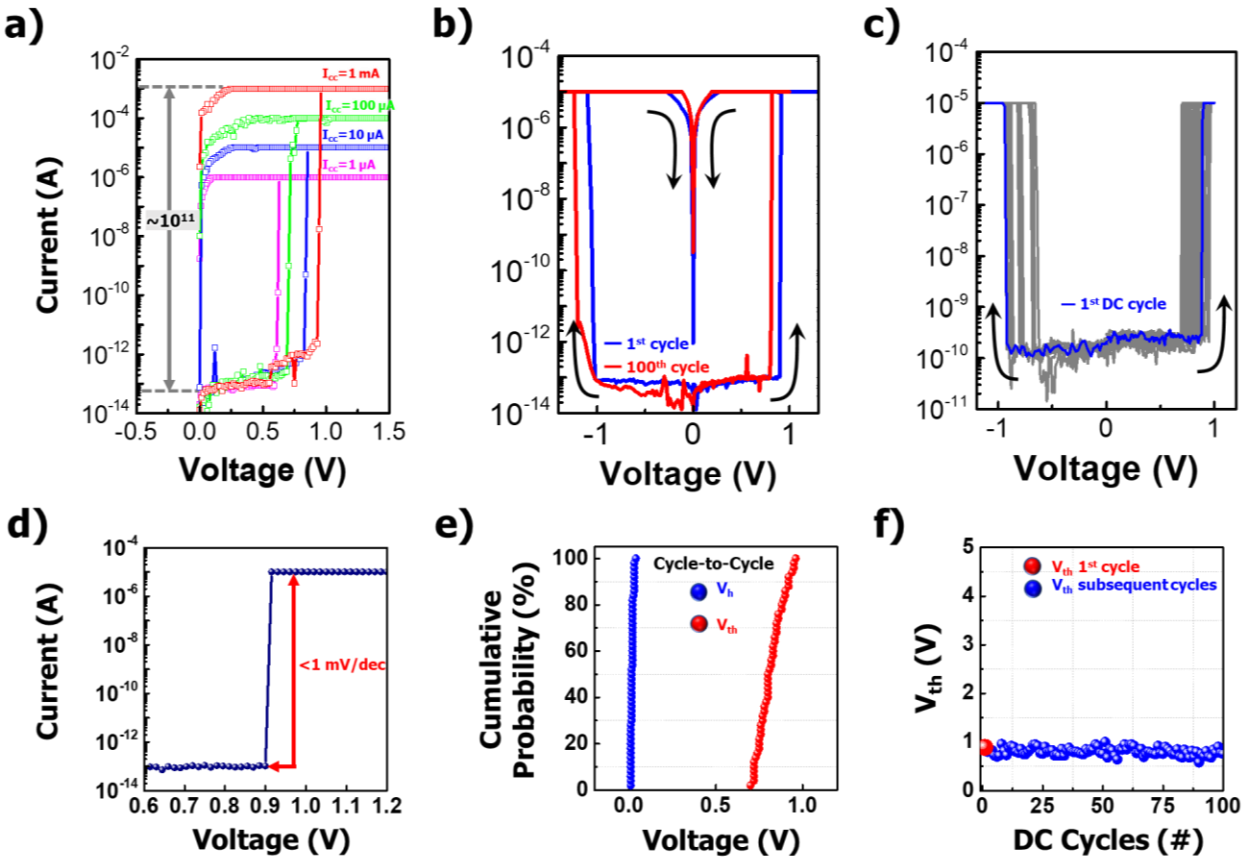

Figure 4.32. Excellent performance of Ag-doped ZnO based TS selector. a) TS behavior of Ag-doped ZnO based selector device at different compliance currents (I_{cc}) from 1 µA to 1 mA, showing extremely high selectivity (on/off ratio) around 10^{11}. (b) Reliable selector device operation up to 100 DC cycles (measurements in slow integration time). (c) Bidirectional TS behavior of selector device in 100 DC voltage sweep cycles (measurements in fast integration time). (d) Subthreshold switching slope showing <1 mV per decade for selector device. (e) Cumulative probability of turn-on voltage (threshold voltage, V_{th}) and turn-off voltage (hold voltage, V_h) as cycle-to-cycle. (f) V_{th} variation measured for first cycle vs subsequent cycles in 100 successive DC cycles.

to 1 mA. A gigantic selectivity (I_{on}/I_{off}) of ~10^{11} was achieved, and a reliable device operation was observed for >100 successive DC cycles at 10 µA I_{cc}. Also, the devices showed an ultra-steep SS of ~0.8 mV/decade, and *on*-current density of ~1.6 MA/cm^2. Results in Figure 4.34 ratify that an optimum Ag concentration is critical for achieving EF-free, enhanced crystallinity resulting in superior selection behavior.

Figure 4.35 shows the AC characteristics of ~0.14 at. % Ag-doped selectors. A write pulse of 1 µs with an amplitude of 1.5 V was applied to the selector device followed by a read voltage pulse of 0.5 V after a delay of 1 µs, as shown in Figure 4.35a. It is shown that the selector turns-on in ~38 ns, while it can relax to off-state in ~64 ns. Figure 4.35b shows the AC endurance test where a stably repeatable behavior up to10^6 pulses is exhibited. Figure 4.36 shows the comparative analysis of DC-*IV* characteristics for the different SL thicknesses. No TS is observed in the lowest thickness of 15 nm for SL (Figure 4.36a). The devices showed stuck-on failure immediately after applying voltage bias. For the SL thickness of 30 nm, excellent EF-free TS was observed with a

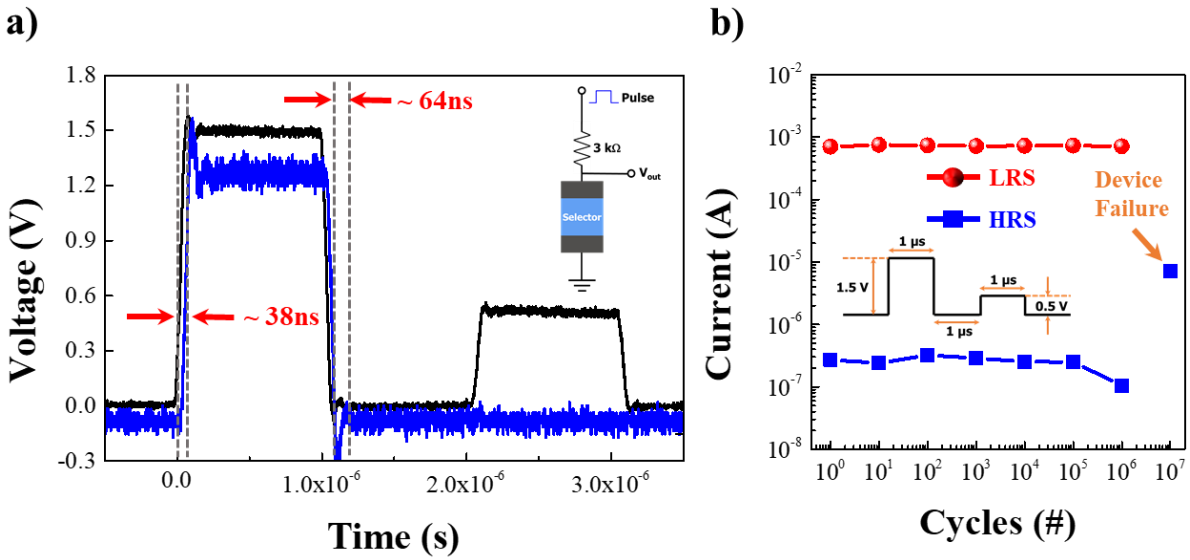

Figure 4.33. (a) Transient characteristics of the selector devices with AC pulse test showing switching speed (~38 ns) and relaxation time (~64 ns). Input and output signals are shown in black and blue respectively. (b) AC endurance (up to 10^6 cycles) of the selector device.

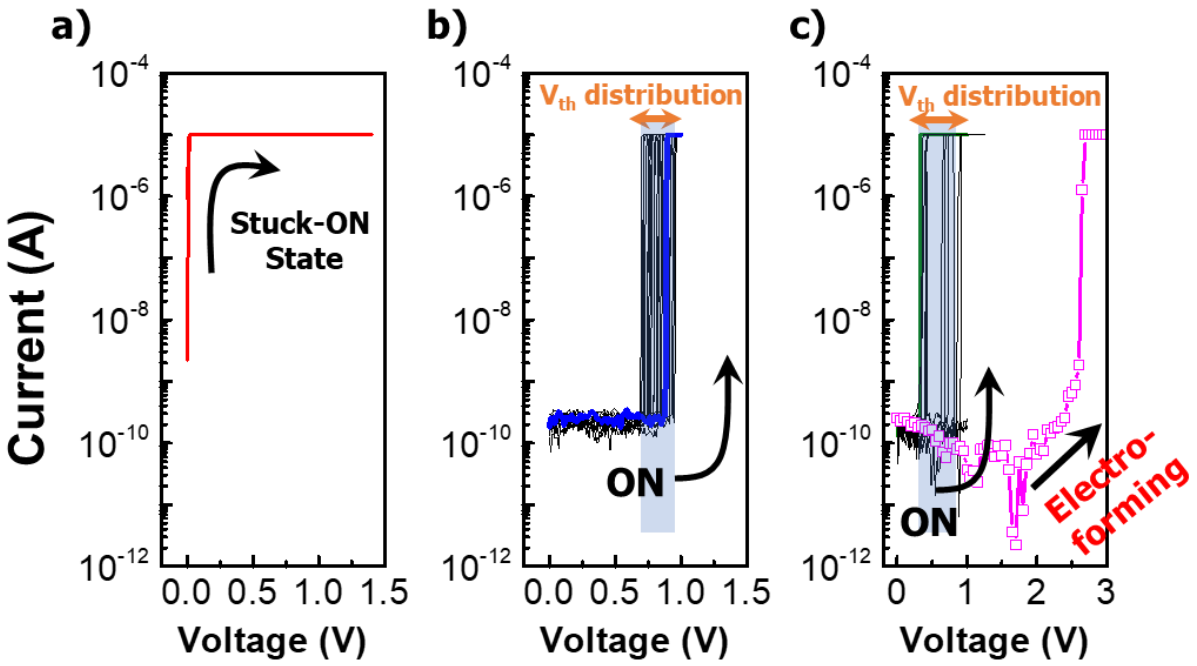

Figure 4.34. Representative volatile switching characteristics of the Ag-doped ZnO based TS selector devices, with switching layer thickness of (a) ~15 nm, stuck-ON state showing no threshold switching, (b) ~30 nm, showing EF-free TS behavior with tight V_{th} distribution for cycle-to-cycle, and (c) ~75 nm, showing TS behavior following EF process, with widely distributed V_{th} for cycle-to-cycle. Black arrow indicates the measurement direction. Blue lines represent the first respective DC voltage sweep in (a-c).

tight V_{th} distribution (Figure 4.36b). When a very thick layer of SL, 75 nm, was deposited then the devices showed TS after EF process and exhibited stuck-off failure after repeated measurements (Figure 4.36c). As previously discussed, that with the increase in ZnO SLs by 'n', the probability for filament formation drops by 'n', which explains the volatile switching behavior with the thickness increase.

Finally, the reliability and reproducibility has been investigated for ~0.14 at. % Ag-doped selector devices. Figure 4.37a shows the normal probability plot of cycle-to-cycle V_{th} variation analyzed for the case of (i) device-to-device for same batch and sample, (ii) batch-to-batch, and (iii) sample-to- sample, for same batch. Here, one batch has 3-4 samples, and one sample contains

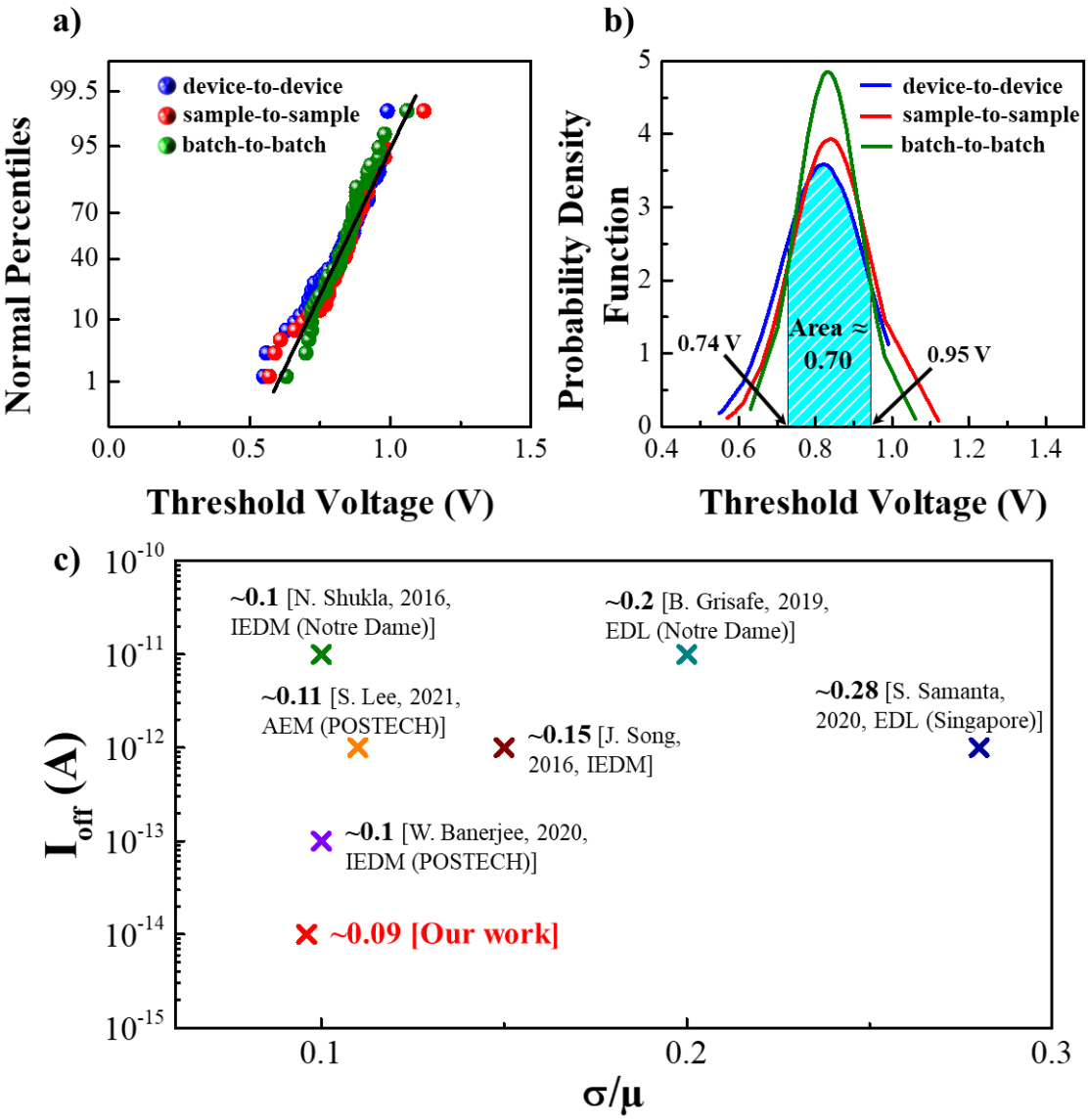

Figure 4.35. (a) Normal probability plot of V_{th} variation for selector devices analyzed in the case of device-to-device for same batch and sample, batch-to-batch, and sample-to-sample for same batch, showing variances along the reference line. (b) Probability Density Function of the V_{th} variation for case (a). (c) Comparison of I_{off} vs σ/μ realized in our work, and amorphous selector devices in other reported literatures.

20×20 selector devices. For each analyzed sample, we tested at least 5 devices selected randomly and recorded V_{th} for a minimum of 10 DC-*IV* cycles per device. Standard deviation (σ)/ mean (μ) – coefficient of variation, for all the tested selector devices is ~0.09, with ~8 % variance in V_{th}.

The reduced variances are attributed to anisotropic diffusion of Ag ions in the well-developed preferred *c*-axis oriented (002) crystalline ZnO (wurtzite) phase,[123,124] in addition to restricted Ag ion influx modulated by doping.[47,115,119,120] Figure 4.37b shows that ~70 % of all the measured devices fall in a narrow V_{th} range of 0.21 V, having mere ~4 % V_{th} variance. Figure 4.37c compares the I_{off} vs σ/μ in this work with the conventional amorphous SL structures reported in previously published literatures.[46,139,209–212] Our devices exhibit one order I_{off} reduction compared to lowest reported I_{off}, simultaneously having an improved coefficient of variation.

In conclusion, implementing a (002) preferred *c*-axis oriented, wurtzite polycrystalline ZnO SL structure to control Ag ion diffusion, a highly robust TS behavior is realized such as EF-free high selectivity (~10^{11}), extremely low off-state current (~10 fA), high on-current density (~1.6 MA/cm^2), ultra-steep SS (~0.8 mV/decade), satisfactory AC endurance (>10^6), fast operation speed (~38 ns) and relaxation speed (~64 ns), with an outstanding device-to-device uniformity having just ~8 % V_{th} fluctuations. The demonstrated results show that our proposed low concentration (~0.14 at. %) Ag-doped polycrystalline ZnO structure could be a promising next-generation selector candidate for ultrahigh density 3D X-Point applications.

4.5 Summary

This chapter summarizes the sputtering/co-sputtering approach for fabricating nano-polycrystalline Ag-doped TS selector devices. Delta/layered doping and uniform doping profiles have been demonstrated as feasible techniques to restrict Ag concentration in the SL and respective switching characteristics have been demonstrated. In this work, a nano polycrystalline Ag-doped ZnO based TS selector *via* a facile co-sputtering technique is investigated without using an Ag active metal layer. The effects of Ag concentration with respect to OFF-state leakage current (I_{off})

were studied, and the results demonstrate that by regulating Ag doping concentration in the switching layer, an electroforming-free switching with an I_{on}/I_{off} ratio of ~10^8 could be achieved, having an extremely low I_{off} of ~10^{-13} A. Furthermore, cycling endurance can also be improved as the formation of laterally thick and stable filament does not happen promptly with consequent measurements when there is limited amount of Ag in SL. The selector device performance enhancement is attributed to the doping-based polycrystalline structure that facilitates enhanced control on filament formation due to the restricted availability and anisotropic diffusion of Ag ions in the polycrystalline ZnO SL, thereby trimming down the overall stochasticity during metallic filament growth. The present study demonstrates that a doping-based polycrystalline SL structure can be implemented in a selector device to augment TS characteristics *i.e.*, device variances and cycling endurance for adoption in ultra-high density memory applications. When Ag concentration was further reduced by using an extreme-lightly doped composite target, remarkable switching characteristics were realized. The TS selectors with extremely controlled doping of ~0.14 at. % Ag concentration showed remarkable electroforming (EF)-free selection behavior such as gigantic selectivity (~10^{11}), extreme-low off-current (~10 fA), high on-current density (~1.6 MA/cm^2), ultra-steep switching slope (~0.8 mV/decade), satisfactory endurance (>10^6), fast switch-*on* speed (~38 ns) and relaxation speed (~64 ns), and high device yield (~90%). Furthermore, selector devices showed reproducible selection behavior with stable threshold voltage (V_{th}) having merely ~8% variances. Table 4.2 summarizes the final accomplished parameters for the threshold switching selectors in this dissertation which exceeds the expected target values mentioned previously in Table 1.1. Table 4.3 provides a comparison between the most eminent and commercially available OTS [213] selector and the Ag doping-based polycrystalline ZnO threshold

switching selector realized in this dissertation. Table 4.4 compares our work with other reported literatures based on amorphous threshold switching selectors.[46,139,209–212]

Table 4.2. Summary of the final accomplished parameters for the Ag doping-based polycrystalline ZnO threshold switching selector fabricated in this dissertation.

FEATURES	ACCOMPLISHED parameters
Selectivity ratio (I_{on}/I_{off})	~ 10^{11}
Leakage Current (I_{off})	~ 10 fA
On-state current density, J_{on}	~ 1.6 MA/cm^2
Switching slope (subthreshold swing, SS)	~ 0.8 mV/decade
Switching speed (turn-on and dissolution)	~ 38 ns, 64 ns
Thermal budget	N/A (@ RT)
Device uniformity (variances)	~ 8%
AC endurance	> 10^6
Bipolar operation	Yes
V_{th} & V_h tunability	Yes
Memory collocation	Yes

Table 4.3. Comparison between the most eminent and commercially available OTS selector and the Ag-doped polycrystalline ZnO threshold switching selector realized in this dissertation.

FEATURES	OTS	Ag-doped Polycrystalline ZnO TS Selector
Material	AsTeGeSiN	ZnO
Leakage current (I_{off}) [A]	~0.1-1 x 10^{-6}	~1x10^{-14}
On. J [MA/cm^2]	10	~1.6
Off. J [kA/cm^2]	2	~2.5 x 10^{-13}
Selectivity ratio (I_{on}/I_{off})	>10^3	~10^{11}
SS [mV/dec]	<50	~0.8
Turn-ON speed [ns]	5	~34
Process Temperature [˚C]	~200	@RT

Table 4.4. Summary of the selector parameters realized in this work compared with the conventional amorphous SL structures reported in previously published literatures.

Stack	**I_{off}**	**I_{on}/I_{off}**	**V_{th}, V_H**	**t_{on}, t_{off}**	**SS**	**T ˚C**	**σ/μ**	**Reference**
AgTe/TiN/TiO_2/Pt	~1pA	10^8	~0.4V, ~0.05V	N/A, 100ns	~5mV/dec	400	~0.15	J. Song, 2016, IEDM (POSTECH)
Ag/HfO_2/SiO_2/p+-Si	~10pA	10^7	~1.5V, ~0.1V	58ns, 67ns	<3mV/dec	90	~0.1	N. Shukla, 2016, IEDM (Notre Dame)
Ag/TiN/HfOx/Pt	~10pA	10^7	~0.25V, ~0V	~28ns, 100μs	N/A	120	~0.2	B. Grisafe, 2019, EDL (Notre Dame)
Ag/Al_2O_3/SiOx/W	~1pA	10^8	~0.25V, ~0V	N/A, 200ns	<5mV/dec	250	~0.28	S. Samanta, 2020, EDL (Singapore)
AgTe/HfOx/HfO_2/Pt	~1pA	10^8	~1V, ~0.3V	~1μs, ~100ns	N/A	250	~0.11	S. Lee, 2021, Adv. Electron. Mater. (POSTECH)
AgTe/HfOx/Pt	~100fA	10^9	~0.6V, ~0.2V	~1μs, N/A	~1mV/dec	N/A	~0.1	W. Banerjee, 2020, IEDM (POSTECH)
Pt/Ag:ZnO/Pt	**~10fA**	**10^{11}**	**~0.8V, ~0V**	**~38ns, ~64ns**	**~0.8mV/dec**	**RT**	**~0.09**	**This work (UTD)**

CHAPTER 5

CONCLUSIONS AND FUTURE WORK

5.1 Conclusions

This dissertation is focused on the development of a robust and reliable threshold switching selector for inhibiting any sneak currents from *half*-selected or *un*-selected cells in a 3D X-point array. Also, it provides a way on circumventing the intrinsic device issues of threshold voltage variances and lousy cycling endurance found customarily in the conventional amorphous structured Ag active electrode-based threshold switching selectors. An extensive comprehensive elaboration has been provided to shed some light on the fundamentals of Ag-doping effect in the nano polycrystalline ZnO switching layer by employing various deposition techniques like ECD, ALD and sputtering/co-sputtering. Selector device's electrical, chemical, and physical properties have been characterized using various tools such as Keithley semiconductor parameter analyzer, XPS, XRD, ICP-MS, AFM, and SEM.

This work discusses two of the adopted deposition techniques *i.e.*, ALD and sputtering/co-sputtering for fabricating the Ag-based threshold switching selectors. Doping approach has been discussed in detail for curtailing the Ag concentration in the ZnO SL with the aim to control V_{th} variabilities and enhance cycling endurance. All the findings from different deposition techniques can be summarized in nutshell as – a) Introducing Ag as a dopant in SL instead of an Ag active metal layer reduces the Ag ions influx during filament growth, and b) (002) *c*-axis preferred orientation for wurtzite ZnO facilitates anisotropic Ag ions diffusion which leads to reduction in overall stochasticity of filament formation process, thus enhancing endurance and lowering threshold voltage fluctuations.

5.2 Future Work

Integration of Metal-Filament type Ag-doped Nanopolycrystalline ZnO-based Selector with Ferroelectric Memory Element for Neuromorphic Computing

Currently, 3D X-point memristive architectures have been in the spotlight for being promising candidates for implementing bio-inspired neuromorphic computing hardware for mimicking human brain functionality.[214–218] For a X-point array, the choice of memory cell and selector device is very crucial to get overall high performance and array efficiency. Our research group has a lot of experience in the fabrication and characterization of highly robust ferroelectric capacitors using atomic layer deposited $Hf_xZr_{1-x}O_2$ (HZO) at a very low process temperature of 350°C, enabling easier integration in back-end-of-line processes. Also, we realized a highly reliable and robust Ag-doped nanopolycrystalline ZnO-based threshold switching selector which

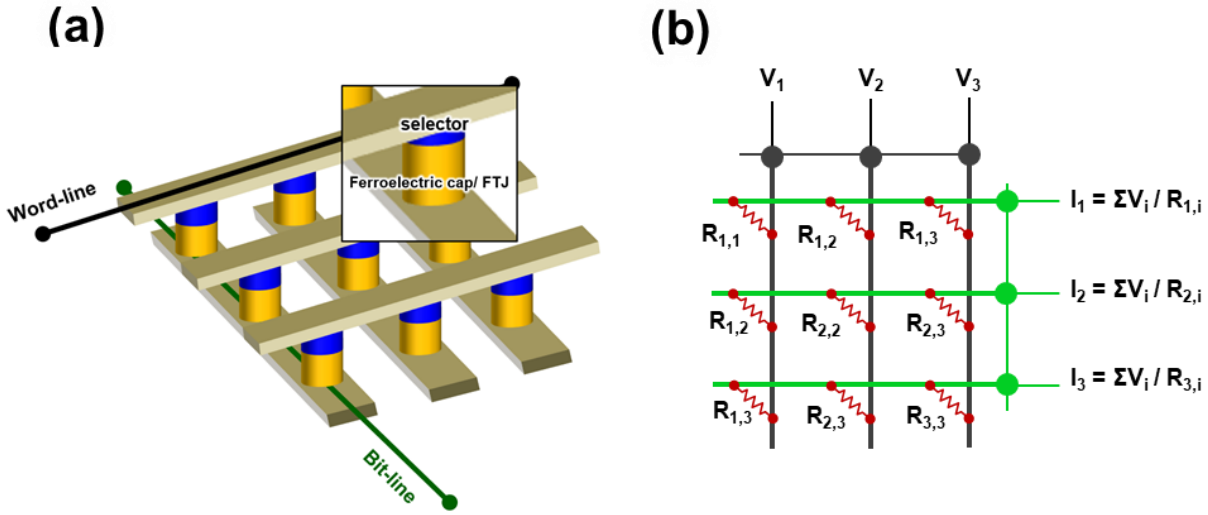

Figure 5.1. a) schematic of a cross point structure using a selector and ferroelectric component (b) an example of analog computing operation performed using a cross bar structure.

offers very high selectivity (on/off current ratio ~10^{11}) and other features discussed in detail at CHAPTER 4. Thus, we propose novel X-point arrays using integrated ferroelectric memory and

selectors, (1F1S) structure (Figure 5.1) for neuromorphic applications for future studies. Brain-inspired neuromorphic framework is a substitute to replace the conventional Von-Neumann computing and memory architecture. This framework offers several advantages in term of scalability and energy efficiency. To successfully build a neuromorphic hardware, a key requirement is to have memory elements with analog behavior. The multiple memory states of some novel non-volatile memory (NVM) devices can be leveraged to perform the in-memory computation required for neuromorphic systems. Ferroelectric materials are suitable for such neural devices due to their analog storage of conductance states, and their analog capacitive behavior is also promising (Figure 5.2). It would be interesting to investigate a cross-point array by integrating the ferroelectric material with a selector, to enable high density and high efficiency synapse cells with a $4F^2$ footprint. The scope of this research can possibly span from materials, process and integration to circuit and system level investigation. This task will be performed in

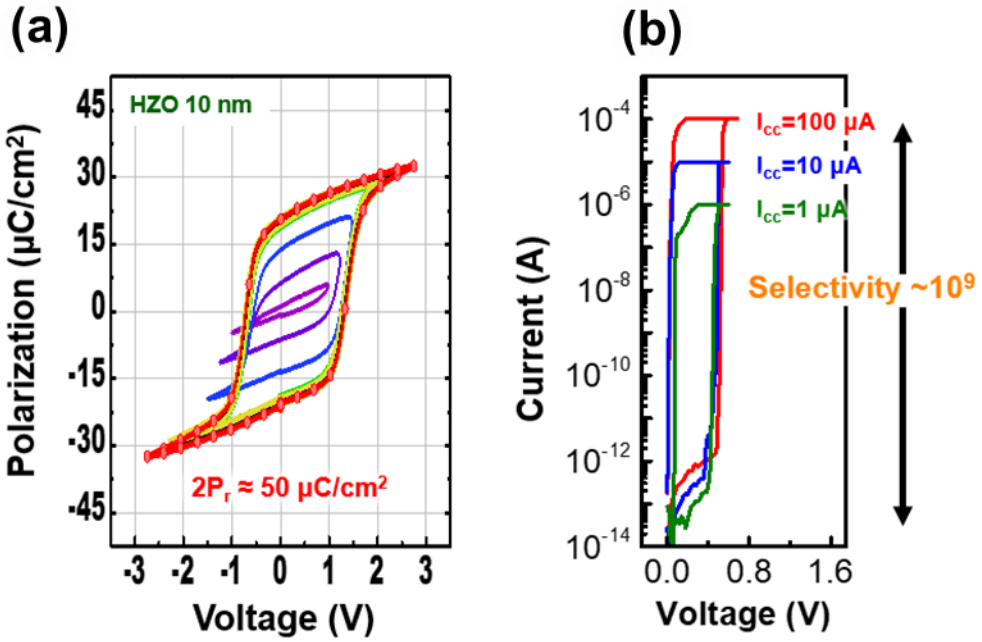

Figure 5.2. a) Ferroelectric properties of 10nm HZO metal-ferroelectric-metal
(b) Threshold switching properties of sputtered Ag doped-ZnO

collaboration with a team comprising of simulation experts. Our research group will focus on materials, processes, and integration while the simulation team will be focusing on device modeling and circuit design and simulation to realize practical fabrication and understanding of neuromorphic hardware components leveraging the characteristics of ferroelectric devices.

We aim to analyze and prove the concept of using ferroelectric materials for neuromorphic applications. The goals targeted during the proposed timeline are: -

1. A ferroelectric tunnel junction (FTJ) structure will be modeled, fabricated, and characterized. An FTJ 3x3 cross-point array will be modeled, fabricated, and characterized to leverage the memristive behavior of the ferroelectric material.
2. A FE-capacitor 3x3 cross-point array will be modeled, fabricated, and characterized, and the possibility of leveraging this memcapacitor behavior will be explored.
3. Integration of FTJ and/or FE-capacitor with a selector will be investigated. Simulations will also be performed to optimize the ferroelectric and selector properties needed to enable proper operation of the neuromorphic crossbar structure.

This proposed work will help us generate preliminary results for the fabrication of FTJ/Fe-cap cross-point arrays, and to aid in the device to system level understanding of neuromorphic circuits.

REFERENCES

1. Dennard, R. H., Gaensslen, F. H., Hwa-Nien, Y. U., Leo Rideout, V., Bassous, E. & Leblanc, A. R. Design of Ion-Implanted MOSFETs with Very Small Physical Dimensions. *Proc. IEEE* **87,** 668–678 (1999).

2. Moore, G. E. Cramming more components onto integrated circuits (Reprinted from Electronics. *Proc. Ieee* **86,** 82–85 (1998).

3. Huang, X., Lee, W. C., Kuo, C., Hisamoto, D., Chang, L., Kedzierski, J., Anderson, E., Takeuchi, H., Choi, Y. K., Asano, K., Subramanian, V., King, T. J., Bokor, J. & Hu, C. Sub-50 nm P-channel FinFET. *IEEE Trans. Electron Devices* **48,** 880–886 (2001).

4. Yanagawa, Y., Sekiguchi, T., Kotabe, A., Ono, K. & Takemura, R. In-substrate-bitline sense amplifier with array-noise-gating scheme for low-noise 4F2 DRAM array operable at 10-fF cell capacitance. *IEEE Symp. VLSI Circuits, Dig. Tech. Pap.* **911,** 230–231 (2011).

5. Kim, S., Kim, H. D. & Choi, S. J. Numerical study of read scheme in one-selector one-resistor crossbar array. *Solid. State. Electron.* **114,** 80–86 (2015).

6. Sung, C., Hwang, H. & Yoo, I. K. Perspective: A review on memristive hardware for neuromorphic computation. *J. Appl. Phys.* **124,** (2018).

7. Burr, G. W., Shelby, R. M., Sidler, S., Di Nolfo, C., Jang, J., Boybat, I., Shenoy, R. S., Narayanan, P., Virwani, K., Giacometti, E. U., Kurdi, B. N. & Hwang, H. Experimental Demonstration and Tolerancing of a Large-Scale Neural Network (165 000 Synapses) Using Phase-Change Memory as the Synaptic Weight Element. *IEEE Trans. Electron Devices* **62,** 3498–3507 (2015).

8. Ankit, A., Sengupta, A. & Roy, K. TraNNsformer: Neural network transformation for memristive crossbar based neuromorphic system design. *IEEE/ACM Int. Conf. Comput. Des. Dig. Tech. Pap. ICCAD* **2017-Novem,** 533–540 (2017).

9. Van De Burgt, Y., Lubberman, E., Fuller, E. J., Keene, S. T., Faria, G. C., Agarwal, S., Marinella, M. J., Alec Talin, A. & Salleo, A. A non-volatile organic electrochemical device as a low-voltage artificial synapse for neuromorphic computing. *Nat. Mater.* **16,** 414–418 (2017).

10. Kim, S. J., Kim, S. B. & Jang, H. W. Competing memristors for brain-inspired computing. *iScience* **24,** 101889 (2021).

11. Burr, G. W., Shelby, R. M., Sebastian, A., Kim, S., Kim, S., Sidler, S., Virwani, K., Ishii, M., Narayanan, P., Fumarola, A., Sanches, L. L., Boybat, I., Le Gallo, M., Moon, K., Woo, J., Hwang, H. & Leblebici, Y. Neuromorphic computing using non-volatile memory. *Adv. Phys. X* **2,** 89–124 (2017).

12. Chua, L. If it's pinched it's a memristor. *Semicond. Sci. Technol.* **29,** (2014).

13. Xia, Q. & Yang, J. J. Memristive crossbar arrays for brain-inspired computing. *Nat. Mater.* **18,** 309–323 (2019).

14. Lin, P., Li, C., Wang, Z., Li, Y., Jiang, H., Song, W., Rao, M., Zhuo, Y., Upadhyay, N. K., Barnell, M., Wu, Q., Yang, J. J. & Xia, Q. Three-dimensional memristor circuits as complex neural networks. *Nat. Electron.* **3,** 225–232 (2020).

15. Merolla, P. A., Arthur, J. V, Alvarez-Icaza, R., Cassidy, A. S., Sawada, J., Akopyan, F., Jackson, B. L., Imam, N., Guo, C., Nakamura, Y., Brezzo, B., Vo, I., Esser, S. K., Appuswamy, R., Taba, B., Amir, A., Flickner, M. D., Risk, W. P., Manohar, R. & Modha, D. S. A million spiking-neuron integrated circuit with a scalable communication network and interface. *Science (80-.).* **345,** 668–673 (2014).

16. De Salvo, B. Brain-Inspired technologies: Towards chips that think? in *Dig. Tech. Pap. - IEEE Int. Solid-State Circuits Conf.* **61,** 12–18 (IEEE, 2018).

17. Salahuddin, S., Ni, K. & Datta, S. The era of hyper-scaling in electronics. *Nat. Electron.* **1,** 442–450 (2018).

18. Burr, G. W., Kurdi, B. N., Scott, J. C., Lam, C. H., Gopalakrishnan, K. & Shenoy, R. S. Overview of candidate device technologies for storage-class memory. *IBM J. Res. Dev.* **52,** 449–464 (2008).

19. Waser, R. & Aono, M. in *Nanosci. Technol. A Collect. Rev. from Nat. Journals* 158–165 (2009). doi:10.1142/9789814287005_0016

20. Ielmini, D. Resistive switching memories based on metal oxides: Mechanisms, reliability and scaling. *Semicond. Sci. Technol.* **31,** (2016).

21. Wuttig, M. & Yamada, N. Phase-change materials for rewriteable data storage. *Nat. Mater.* **6,** 824–832 (2007).

22. Sousa, V. Chalcogenide materials and their application to Non-Volatile Memories. in *Microelectron. Eng.* **88,** 807–813 (2011).

23. Chen, A. A review of emerging non-volatile memory (NVM) technologies and applications. *Solid. State. Electron.* **125,** 25–38 (2016).

24. Wang, Z., Wu, H., Burr, G. W., Hwang, C. S., Wang, K. L., Xia, Q. & Yang, J. J. Resistive switching materials for information processing. *Nat. Rev. Mater.* **5,** 173–195 (2020).

25. Yang, J. J., Strukov, D. B. & Stewart, D. R. Memristive devices for computing. *Nat. Nanotechnol.* **8,** 13–24 (2013).

26. Waser, R., Dittmann, R., Staikov, C. & Szot, K. Redox-based resistive switching memories nanoionic mechanisms, prospects, and challenges. *Adv. Mater.* **21,** 2632–2663 (2009).

27. Valov, I., Waser, R., Jameson, J. R. & Kozicki, M. N. Electrochemical metallization memories - Fundamentals, applications, prospects. *Nanotechnology* **22,** (2011).

28. Russo, U., Kamalanathan, D., Ielmini, D., Lacaita, A. L. & Kozicki, M. N. Study of multilevel programming in Programmable Metallization Cell (PMC) memory. *IEEE Trans. Electron Devices* **56,** 1040–1047 (2009).

29. Yang, Y., Gao, P., Li, L., Pan, X., Tappertzhofen, S., Choi, S., Waser, R., Valov, I. & Lu, W. D. Electrochemical dynamics of nanoscale metallic inclusions in dielectrics. *Nat. Commun.* **5,** (2014).

30. Yang, Y., Gao, P., Gaba, S., Chang, T., Pan, X. & Lu, W. Observation of conducting filament growth in nanoscale resistive memories. *Nat. Commun.* **3,** (2012).

31. Chae, B. G., Seol, J. B., Song, J. H., Baek, K., Oh, S. H., Hwang, H. & Park, C. G. Nanometer-Scale Phase Transformation Determines Threshold and Memory Switching Mechanism. *Adv. Mater.* **29,** 1–8 (2017).

32. Sun, H., Liu, Q., Li, C., Long, S., Lv, H., Bi, C., Huo, Z., Li, L. & Liu, M. Direct Observation of Conversion Between Threshold Switching and Memory Switching Induced by Conductive Filament Morphology. *Adv. Funct. Mater.* **24,** 5679–5686 (2014).

33. Guo, X., Schindler, C., Menzel, S. & Waser, R. Understanding the switching-off mechanism in Ag+ migration based resistively switching model systems. *Appl. Phys. Lett.* **91,** (2007).

34. Wang, Z., Joshi, S., Savel'ev, S. E., Jiang, H., Midya, R., Lin, P., Hu, M., Ge, N., Strachan, J. P., Li, Z., Wu, Q., Barnell, M., Li, G. L., Xin, H. L., Williams, R. S., Xia, Q. & Yang, J. J. Memristors with diffusive dynamics as synaptic emulators for neuromorphic computing. *Nat. Mater.* **16,** 101–108 (2017).

35. Cheng, B., Emboras, A., Salamin, Y., Ducry, F., Ma, P., Fedoryshyn, Y., Andermatt, S., Luisier, M. & Leuthold, J. Ultra compact electrochemical metallization cells offering reproducible atomic scale memristive switching. *Commun. Phys.* **2,** 1–9 (2019).

36. Lee, M., Park, Y., Kang, B., Ahn, S., Lee, C., Kim, K., Stefanovich, G., Lee, J., Chung, S., Kim, Y., Lee, C., Bong, J.-, Baek, I. & Yoo, I. High Density Resistance RAM Applications. *Electron Devices Meet. 2007. IEDM 2007. IEEE Int.* 771–774 (2007).

37. Gopalakrishnan, K., Shenoy, R. S., Rettner, C. T., Virwani, K., Bethune, D. S., Shelby, R. M., Burr, G. W., Kellock, A., King, R. S., Nguyen, K., Bowers, A. N., Jurich, M., Jackson, B., Friz, A. M., Topuria, T., Rice, P. M. & Kurdi, B. N. Highly scalable novel access device based on Mixed Ionic Electronic Conduction (MIEC) materials for high density phase change memory (PCM) arrays. *Dig. Tech. Pap. - Symp. VLSI Technol.* **1,** 205–206 (2010).

38. Bowers, a N., Jurich, M., Brightsky, M., Joseph, E. a, Kellock, a J., Arellano, N., Kurdi, B. N. & Gopalakrishnan, K. 3D crosspoint memory based on Mixed-Ionic-Electronic-Conduction (MIEC) Materials. *IEDM, Tech. Dig. - Int. Electron Devices Meet.* **95120,** 36–39 (2012).

39. Lee, M. J., Lee, D., Kim, H., Choi, H. S., Park, J. B., Kim, H. G., Cha, Y. K., Chung, U. I., Yoo, I. K. & Kim, K. Highly-scalable threshold switching select device based on chaclogenide glasses for 3D nanoscaled memory arrays. *Tech. Dig. - Int. Electron Devices Meet. IEDM* **2,** 33–35 (2012).

40. Kau, D., Tang, S., Karpov, I. V., Dodge, R., Klehn, B., Kalb, J. A., Strand, J., Diaz, A., Leung, N., Wu, J., Lee, S., Langtry, T., Chang, K. W., Papagianni, C., Lee, J., Hirst, J., Erra, S., Flores, E., Righos, N., Castro, H. & Spadini, G. A stackable cross point phase change memory. *Tech. Dig. - Int. Electron Devices Meet. IEDM* 617–620 (2009). doi:10.1109/IEDM.2009.5424263

41. Kim, S., Kim, Y. B., Kim, K. M., Kim, S. J., Lee, S. R., Chang, M., Cho, E., Lee, M. J., Lee, D., Kim, C. J., Chung, U. I. & Yoo, I. K. Performance of threshold switching in chalcogenide glass for 3D stackable selector. *Dig. Tech. Pap. - Symp. VLSI Technol.* 9–10 (2013).

42. Son, M., Lee, J., Park, J., Shin, J., Choi, G., Jung, S., Lee, W., Kim, S., Park, S. & Hwang, H. Excellent selector characteristics of nanoscale VO2 for high-density bipolar ReRAM applications. *IEEE Electron Device Lett.* **32,** 1579–1581 (2011).

43. Kim, S., Liu, X., Park, J., Jung, S., Lee, W., Woo, J., Shin, J., Choi, G., Cho, C., Park, S., Lee, D., Cha, E. J., Lee, B. H., Lee, H. D., Kim, S. G., Chung, S. & Hwang, H. Ultrathin (<10nm) Nb 2O 5/NbO 2 hybrid memory with both memory and selector characteristics for high density 3D vertically stackable RRAM applications. *Dig. Tech. Pap. - Symp. VLSI Technol.* 155–156 (2012). doi:10.1109/VLSIT.2012.6242508

44. Song, J., Woo, J., Prakash, A., Lee, D. & Hwang, H. Threshold Selector with High Selectivity and Steep Slope for Cross-Point Memory Array. *IEEE Electron Device Lett.* **36,** 681–683 (2015).

45. Midya, R., Wang, Z., Zhang, J., Savel'ev, S. E., Li, C., Rao, M., Jang, M. H., Joshi, S., Jiang, H., Lin, P., Norris, K., Ge, N., Wu, Q., Barnell, M., Li, Z., Xin, H. L., Williams, R. S., Xia, Q. & Yang, J. J. Anatomy of Ag/Hafnia-Based Selectors with 1010 Nonlinearity. *Adv. Mater.* **29,** 1–8 (2017).

46. Shukla, N., Grisafe, B., Ghosh, R. K., Jao, N., Aziz, A., Frougier, J., Jerry, M., Sonde, S., Rouvimov, S., Orlova, T., Gupta, S. & Datta, S. Ag/HfO2 based threshold switch with extreme non-linearity for unipolar cross-point memory and steep-slope phase-FETs. *Tech. Dig. - Int. Electron Devices Meet. IEDM* 34.6.1-34.6.4 (2017). doi:10.1109/IEDM.2016.7838542

47. Kim, H. S., Sahota, A., Mohan, J., Lucero, A. T., Chan Jung, Y., Kim, M., Lee, J.-S., Choi, R., Kim, S. J. & Kim, J. Extremely Low Leakage Threshold Switch with Enhanced Characteristics via Ag Doping on Polycrystalline ZnO Fabricated by Facile Electrochemical Deposition for an X-Point Selector. *ACS Appl. Electron. Mater.* **3,** 2309–2316 (2021).

48. Burr, G. W., Shenoy, R. S., Virwani, K., Narayanan, P., Padilla, A., Kurdi, B. & Hwang, H. Access devices for 3D crosspoint memory. *J. Vac. Sci. Technol. B Microelectron. Nanom. Struct.* **32,** (2014).

49. Aluguri, R. & Tseng, T.-Y. Overview of Selector Devices for 3-D Stackable Cross Point RRAM Arrays. *J. Electron Device Soc.* **4,** 294–306 (2016).

50. Chen, A. Memory selector devices and crossbar array design: a modeling-based assessment. *J. Comput. Electron.* **16,** 1186–1200 (2017).

51. Shenoy, R. S., Burr, G. W., Virwani, K., Jackson, B., Padilla, A., Narayanan, P., Rettner, C. T., Shelby, R. M., Bethune, D. S., Raman, K. V., Brightsky, M., Joseph, E., Rice, P. M., Topuria, T., Kellock, A. J., Kurdi, B. & Gopalakrishnan, K. MIEC (mixed-ionic-electronic-conduction)-based access devices for non-volatile crossbar memory arrays. *Semicond. Sci. Technol.* **29,** (2014).

52. Koo, Y., Baek, K. & Hwang, H. Te-based amorphous binary OTS device with excellent selector characteristics for x-point memory applications. in *Dig. Tech. Pap. - Symp. VLSI Technol.* **2016-Septe,** 54–55 (IEEE, 2016).

53. Chekol, S. A., Yoo, J., Park, J., Song, J., Sung, C. & Hwang, H. A C-Te-based binary OTS device exhibiting excellent performance and high thermal stability for selector application. *Nanotechnology* **29,** (2018).

54. Cheng, H. Y., Chien, W. C., Kuo, I. T., Lai, E. K., Zhu, Y., Jordan-Sweet, J. L., Ray, A., Carta, F., Lee, F. M., Tseng, P. H., Lee, M. H., Lin, Y. Y., Kim, W., Bruce, R., Yeh, C. W., Yang, C. H., Brightsky, M. & Lung, H. L. An ultra high endurance and thermally stable selector based on TeAsGeSiSe chalcogenides compatible with BEOL IC Integration for cross-point PCM. in *Tech. Dig. - Int. Electron Devices Meet. IEDM* 2.2.1-2.2.4 (2018). doi:10.1109/IEDM.2017.8268310

55. Yoo, J., Koo, Y., Chekol, S. A., Park, J., Song, J. & Hwang, H. Te-based binary OTS selectors with excellent selectivity (>105), endurance (>108) and thermal stability (>450°C). in *Dig. Tech. Pap. - Symp. VLSI Technol.* **2018-June,** 207–208 (IEEE, 2018).

56. Ovshinsky, S. R. Reversible electrical switching phenomena in disordered structures. *Phys. Rev. Lett.* **21,** 1450–1453 (1968).

57. Shukla, N., Ghosh, R. K., Gnsafe, B. & Datta, S. Fundamental mechanism behind volatile and non-volatile switching in metallic conducting bridge RAM. in *Tech. Dig. - Int. Electron Devices Meet. IEDM* 4.3.1-4.3.4 (2018). doi:10.1109/IEDM.2017.8268325

58. Yoo, J., Park, J., Song, J., Lim, S. & Hwang, H. Field-induced nucleation in threshold switching characteristics of electrochemical metallization devices. *Appl. Phys. Lett.* **111,** (2017).

59. Karpov, V. G., Maltby, R. E. E., Karpov, I. V & Yalon, E. Field-Induced Nucleation in the Presence of a Metal Electrode. *Phys. Rev. Appl.* **3,** 1–6 (2015).

60. Wang, Z., Rao, M., Midya, R., Joshi, S., Jiang, H., Lin, P., Song, W., Asapu, S., Zhuo, Y., Li, C., Wu, H., Xia, Q. & Yang, J. J. Threshold Switching of Ag or Cu in Dielectrics: Materials, Mechanism, and Applications. *Adv. Funct. Mater.* **28,** 1–19 (2018).

61. Sun, W., Gao, B., Chi, M., Xia, Q., Yang, J. J., Qian, H. & Wu, H. Understanding memristive switching via in situ characterization and device modeling. *Nat. Commun.* **10,** 1–13 (2019).

62. Miller, J. M., Dunn, B., Tran, T. D. & Pekala, R. W. Deposition of Ruthenium Nanoparticles on Carbon Aerogels for High Energy Density Supercapacitor Electrodes. *J. Electrochem. Soc.* **144,** L309–L311 (1997).

63. Lee, J. K., Pathan, H. M., Jung, K. D. & Joo, O. S. Electrochemical capacitance of nanocomposite films formed by loading carbon nanotubes with ruthenium oxide. *J. Power Sources* **159,** 1527–1531 (2006).

64. Patake, V. D. & Lokhande, C. D. Chemical synthesis of nano-porous ruthenium oxide (RuO 2) thin films for supercapacitor application. *Appl. Surf. Sci.* **254,** 2820–2824 (2008).

65. Aref, A. A. & Tang, Y. W. Chemical bath deposition synthesis and electrochemical properties of MnO2 thin film: Effect of deposition time and bath temperature. *Mater. Sci. Pol.* **32,** 555–564 (2014).

66. Myamlin, V. A. & Pleskov, Y. V. *Electrochemistry of Semiconductors*. *Electrochem. Semicond.* (1967). doi:10.1007/978-1-4899-6533-2

67. Prod'Homme, P., Maroun, F., Cortès, R. & Allongue, P. Electrochemical growth of ultraflat Au(111) epitaxial buffer layers on H-Si(111). *Appl. Phys. Lett.* **93,** 2–5 (2008).

68. Lay, M. D. & Stickney, J. L. Electrodeposition of Au-Cd alloy nanostructures on Au(111). *J. Am. Chem. Soc.* **125,** 1352–1355 (2003).

69. Switzer, J. A., Liu, R., Bohannan, E. W. & Ernst, F. Epitaxial electrodeposition of a crystalline metal oxide onto single-crystalline silicon. *J. Phys. Chem. B* **106,** 12369–12372 (2002).

70. Goux, A., Pauporté, T., Yoshida, T. & Lincot, D. Mechanistic study of the electrodeposition of nanoporous self-assembled ZnO/eosin y hybrid thin films: Effect of eosin concentration. *Langmuir* **22,** 10545–10553 (2006).

71. Prabu, S. & Wang, H. W. Factors Affecting the Electrodeposition of Aluminum Metal in an Aluminum Chloride–Urea Electrolyte Solution. *J. Chinese Chem. Soc.* **64,** 1467–1477 (2017).

72. Ojo, A. A. & Dharmadasa, I. M. Electroplating of semiconductor materials for applications in large area electronics: A review. *Coatings* **8,** (2018).

73. Johnson, R. W., Hultqvist, A. & Bent, S. F. A brief review of atomic layer deposition : from fundamentals to applications. *Biochem. Pharmacol.* **17,** 236–246 (2014).

74. HWANG, C. J. ALD(Atomic Layer Deposition) Process Technology in the Semiconductor Industry. *Phys. High Technol.* **21,** 37 (2012).

75. Cremers, V., Puurunen, R. L. & Dendooven, J. Conformality in atomic layer deposition: Current status overview of analysis and modelling. *Appl. Phys. Rev.* **6,** (2019).

76. Ovanesyan, R. A., Filatova, E. A., Elliott, S. D., Hausmann, D. M., Smith, D. C. & Agarwal, S. Atomic layer deposition of silicon-based dielectrics for semiconductor manufacturing: Current status and future outlook. *J. Vac. Sci. Technol. A* **37,** 060904 (2019).

77. Baptista, A., Silva, F., Porteiro, J., Míguez, J. & Pinto, G. Sputtering physical vapour deposition (PVD) coatings: A critical review on process improvement andmarket trend demands. *Coatings* **8,** (2018).

78. Triscone, J. M., Fischer, O., Brunner, O., Antognazza, L., Kent, A. D. & Karkut, M. G. YBa2Cu307/PrBa2Cu307 Superlattices: Properties of Ultrathin Superconducting Layers Separated by Insulating Layers. *Phys. Rev. Lett.* **64,** 804–807 (1990).

79. C. B. Eom, J. Z. Sun, K. Yamamoto, A. F. Marshall, K. E. Luther, and T. H. G. In situ grown YBa2Cu3O7−d thin films from single-target magnetron sputtering. *Appl. Phys. Lett.* **595,** 80–83 (2016).

80. Altissimo, M. E-beam lithography for micro-/nanofabrication. *Biomicrofluidics* **4,** (2010).

81. Vieu, C., Carcenac, F., Pépin, A., Chen, Y., Mejias, M., Lebib, A., Manin-Ferlazzo, L., Couraud, L. & Launois, H. Electron beam lithography: Resolution limits and applications. *Appl. Surf. Sci.* **164,** 111–117 (2000).

82. Pimpin, A. & Srituravanich, W. Reviews on micro- and nanolithography techniques and their applications. *Eng. J.* **16,** 37–55 (2012).

83. Wenner, F. A method for measuring Earth resistivity. *J. Washingt. Acad. Sci.* **5,** 561–563 (1915).

84. Oka, M., Yakushiji, T., Tsuchida, Y. & Enokizono, M. Non-destructive Evaluation of Fatigue Damage in the Stainless Steel by Using Electromagnetic Method. *E-Journal Adv. Maint.* **1,** 77–82 (2009).

85. Nasir, S., Hussein, M. Z., Zainal, Z., Yusof, N. A., Mohd Zobir, S. A. & Alibe, I. M. Potential valorization of by-product materials from oil palm: A review of alternative and sustainable carbon sources for carbon-based nanomaterials synthesis. *BioResources* **14,** 2352–2388 (2019).

86. Bracco, G. & Holst, B. *Surface Science Techniques*. *Springer Ser. Surf. Sci.* **51,** (2013).

87. FEIDENHANS'L, R. SURFACE STRUCTURE DETERMINATION BY X-RAY DIFFRACTION. *Surf. Sci. Rep.* **10,** 105–188 (1989).

88. Shinato, K. W., Huang, F. & Jin, Y. Principle and application of atomic force microscopy (AFM) for nanoscale investigation of metal corrosion. *Corros. Rev.* **38,** 423–432 (2020).

89. Benítez, J. J., Guzman-Puyol, S., Domínguez, E., Heredia, A. & Heredia-Guerrero, J. A. Applications and potentialities of Atomic Force Microscopy in fossil and extant plant cuticle characterization. *Rev. Palaeobot. Palynol.* **268,** 125–132 (2019).

90. George, J., Azad, L. B., Poulose, A. M., An, Y. & Sarmah, A. K. Nano-mechanical behaviour of biochar-starch polymer composite: Investigation through advanced dynamic atomic force microscopy. *Compos. Part A Appl. Sci. Manuf.* **124,** 105486 (2019).

91. Wang, B., Wu, X., Gan, T. H. & Rusinek, A. Finite element modelling of atomic force microscope cantilever beams with uncertainty in material and dimensional parameters. *Eng. Trans.* **62,** 403–421 (2014).

92. Wilschefski, S. C. & Baxter, M. R. Inductively Coupled Plasma Mass Spectrometry: Introduction to Analytical Aspects. *Clin. Biochem. Rev.* **40,** 115–133 (2019).

93. Yu, S. Neuro-Inspired Computing with Emerging Nonvolatile Memorys. *Proc. IEEE* **106,** 260–285 (2018).

94. Merolla, P. A., Arthur, J. V., Alvarez-icaza, R., Cassidy, A. S., Sawada, J., Akopyan, F., Jackson, B. L., Imam, N., Guo, C., Nakamura, Y., Brezzo, B., Vo, I., Esser, S. K., Appuswamy, R., Taba, B., Amir, A., Flickner, M. D., Risk, W. P., Manohar, R. & Modha, D. S. A million spiking-neuron integrated circuit with a scalable communication network and interface. *Science (80-.).* **345,** 668–673 (2014).

95. Prezioso, M., Merrikh-Bayat, F., Hoskins, B. D., Adam, G. C., Likharev, K. K. & Strukov, D. B. Training and operation of an integrated neuromorphic network based on metal-oxide memristors. *Nature* **521,** 61–64 (2015).

96. Molas, G., Robayo, D. A., Lopez, J. M., Grenouillet, L., Carabasse, C., Navarro, G., Sabbione, C., Bernard, M., Cagli, C., Castellani, N., Deleruyelle, D., Bocquet, M., Portal, J. M. & Nowak, E. Crosspoint Memory Arrays: Principle, Strengths and Challenges. in *2020 IEEE Int. Mem. Work. IMW 2020 - Proc.* 1–4 (2020). doi:10.1109/IMW48823.2020.9108143

97. Aziz, A., Jao, N., Datta, S. & Gupta, S. K. Analysis of Functional Oxide based Selectors for Cross-Point Memories. *IEEE Trans. Circuits Syst. I Regul. Pap.* **63,** 2222–2235 (2016).

98. Seok, J. Y., Song, S. J., Yoon, J. H., Yoon, K. J., Park, T. H., Kwon, D. E., Lim, H., Kim, G. H., Jeong, D. S. & Hwang, C. S. A review of three-dimensional resistive switching cross-bar array memories from the integration and materials property points of view. *Adv. Funct. Mater.* **24,** 5316–5339 (2014).

99. Park, W. Y., Kim, G. H., Seok, J. Y., Kim, K. M., Song, S. J., Lee, M. H. & Hwang, C. S. A Pt/TiO2/Ti Schottky-type selection diode for alleviating the sneak current in resistance switching memory arrays. *Nanotechnology* **21,** 195201 (2010).

100. Shin, Y. C., Song, J., Kim, K. M., Choi, B. J., Choi, S., Lee, H. J., Kim, G. H., Eom, T. & Hwang, C. S. (In,Sn)2O3/TiO2/Pt Schottky-type diode switch for the TiO2 resistive switching memory array. *Appl. Phys. Lett.* **92,** 162904 (2008).

101. Huang, J. J., Tseng, Y. M., Luo, W. C., Hsu, C. W. & Hou, T. H. One selector-one resistor (1S1R) crossbar array for high-density flexible memory applications. *Tech. Dig. - Int. Electron Devices Meet. IEDM* 31.7.1-31.7.4 (2011). doi:10.1109/IEDM.2011.6131653

102. Chen, Z. X., Yu, H. Y., Singh, N., Shen, N. S., Sayanthan, R. D., Lo, G. Q. & Kwong, D. L. Demonstration of tunneling FETs based on highly scalable vertical silicon nanowires. *IEEE Electron Device Lett.* **30,** 754–756 (2009).

103. Wang, X. P., Fang, Z., Li, X., Chen, B., Gao, B., Kang, J. F., Chen, Z. X., Kamath, A., Shen, N. S., Singh, N., Lo, G. Q. & Kwong, D. L. Highly compact 1T-1R architecture (4F2 footprint) involving fully CMOS compatible vertical GAA nano-pillar transistors and oxide-based RRAM cells exhibiting excellent NVM properties and ultra-low power operation. *Tech. Dig. - Int. Electron Devices Meet. IEDM* **6,** 493–496 (2012).

104. Kim, S., Liu, X., Park, J., Jung, S., Lee, W., Woo, J., Shin, J., Choi, G., Cho, C., Park, S., Lee, D., Cha, E. J., Lee, B. H., Lee, H. D., Kim, S. G., Chung, S. & Hwang, H. Ultrathin (<10nm) Nb2O5/NbO2 Hybrid Memory with Both Memory and Selector Characteristics for High Density 3D Vertically Stackable RRAM Applications. *Dig. Tech. Pap. - Symp. VLSI Technol.* 155–156 (2012). doi:10.1109/VLSIT.2012.6242508

105. Jo, S. H., Kumar, T., Narayanan, S. & Nazarian, H. Cross-Point Resistive RAM Based on Field-Assisted Superlinear Threshold Selector. *IEEE Trans. Electron Devices* **62,** 3477–3481 (2015).

106. Jo, S. H., Kumar, T., Narayanan, S., Lu, W. D. & Nazarian, H. 3D-stackable crossbar resistive memory based on Field Assisted Superlinear Threshold (FAST) selector. *Tech. Dig. - Int. Electron Devices Meet. IEDM* 6.7.1-6.7.4 (2015). doi:10.1109/IEDM.2014.7046999

107. Yoo, J., Kim, S. H., Chekol, S. A., Park, J., Sung, C., Song, J., Lee, D. & Hwang, H. 3D Stackable and Scalable Binary Ovonic Threshold Switch Devices with Excellent Thermal Stability and Low Leakage Current for High-Density Cross-Point Memory Applications. *Adv. Electron. Mater.* **5,** 1900196 (2019).

108. Song, J., Woo, J., Prakash, A., Lee, D. & Hwang, H. Threshold Selector with High Selectivity and Steep Slope for Cross-Point Memory Array. *IEEE Electron Device Lett.* **36,** 681–683 (2015).

109. Lee, S., Yoo, J., Park, J. & Hwang, H. Understanding of the Abrupt Resistive Transition in Different Types of Threshold Switching Devices from Materials Perspective. *IEEE Trans. Electron Devices* **67,** 2878–2883 (2020).

110. Vishwanath, S. K., Woo, H. & Jeon, S. Effect of dysprosium and lutetium metal buffer layers on the resistive switching characteristics of Cu-Sn alloy-based conductive-bridge random access memory. *Nanotechnology* **29,** 385207 (2018).

111. Song, J., Woo, J., Yoo, J., Chekol, S. A., Lim, S., Sung, C. & Hwang, H. Effects of Liner Thickness on the Reliability of AgTe/TiO2-Based Threshold Switching Devices. *IEEE Trans. Electron Devices* **64,** 4763–4767 (2017).

112. Goux, L., Opsomer, K., Degraeve, R., Ller, R. M., Detavernier, C., Wouters, D. J., Jurczak, M., Altimime, L. & Kittl, J. A. Influence of the Cu-Te composition and microstructure on the resistive switching of Cu-Te/Al2O3/Si cells. *Appl. Phys. Lett.* **99,** 053502 (2011).

113. Vishwanath, S. K., Woo, H. & Jeon, S. Non-volatile resistive switching in CuBi-based conductive bridge random access memory device. *Appl. Phys. Lett.* **112,** 253503 (2018).

114. Hua, Q., Wu, H., Gao, B., Zhao, M., Li, Y., Li, X., Hou, X., (Marvin) Chang, M. F., Zhou, P. & Qian, H. A Threshold Switching Selector Based on Highly Ordered Ag Nanodots for X-Point Memory Applications. *Adv. Sci.* **6,** (2019).

115. Jeong, W. H., Han, J. H. & Choi, B. J. Effect of Ag Concentration Dispersed in HfOx Thin Films on Threshold Switching. *Nanoscale Res. Lett.* **15,** (2020).

116. Ji, X., Song, L., He, W., Huang, K., Yan, Z., Zhong, S., Zhang, Y. & Zhao, R. Super Nonlinear Electrodeposition-Diffusion-Controlled Thin-Film Selector. *ACS Appl. Mater. Interfaces* **10,** 10165–10172 (2018).

117. Lee, T. H., Kang, D. Y. & Kim, T. G. Ag:SiOxNy-Based Bilayer ReRAM Structure with Self-Limiting Bidirectional Threshold Switching Characteristics for Cross-Point Array Application. *ACS Appl. Mater. Interfaces* **10,** 33768–33772 (2018).

118. Luo, Q., Xu, X., Liu, H., Lv, H., Gong, T., Long, S., Liu, Q., Sun, H., Banerjee, W., Li, N. & Liu, M. Cu BEOL Compatible Selector with High Selectivity (> 107), Extremely Low off-Current (~pA) and High Endurance (> 1010). *Tech. Dig. - Int. Electron Devices Meet. IEDM* 253–256 (2015).

119. Park, Y., Han, U. Bin, Kim, M. K. & Lee, J. S. Solution-Processed Flexible Threshold Switch Devices. *Adv. Electron. Mater.* **4,** 1–7 (2018).

120. Han, U. Bin, Lee, D. & Lee, J. S. Reliable current changes with selectivity ratio above 109 observed in lightly doped zinc oxide films. *NPG Asia Mater.* **9,** 1–8 (2017).

121. Park, J. H., Kim, D., Kang, D. Y., Jeon, D. S. & Kim, T. G. Nanoscale 3D Stackable Ag-Doped HfO x-Based Selector Devices Fabricated through Low-Temperature Hydrogen Annealing. *ACS Appl. Mater. Interfaces* **11,** 29408–29415 (2019).

122. Yang, H., Li, M., He, W., Jiang, Y., Lim, K. G., Song, W., Zhuo, V. Y. Q., Tan, C. C., Chua, E. K., Wang, W., Yang, Y. & Ji, R. Novel selector for high density non-volatile memory with ultra-low holding voltage and 107 on/off ratio. *Dig. Tech. Pap. - Symp. VLSI Technol.* **2015-Augus,** T130–T131 (2015).

123. Huang, G. Y., Wang, C. Y. & Wang, J. T. First-principles study of diffusion of Li, Na, K and Ag in ZnO. *J. Phys. Condens. Matter* **21,** (2009).

124. Erhart, P. & Albe, K. Diffusion of zinc vacancies and interstitials in zinc oxide. *Appl. Phys. Lett.* **88,** 10–13 (2006).

125. Yan, Y., Al-Jassim, M. M. & Wei, S. H. Doping of ZnO by group-IB elements. *Appl. Phys. Lett.* **89,** 87–90 (2006).

126. Volnianska, O., Boguslawski, P., Kaczkowski, J., Jakubas, P., Jezierski, A. & Kaminska, E. Theory of doping properties of Ag acceptors in ZnO. *Phys. Rev. B - Condens. Matter Mater. Phys.* **80,** 1–8 (2009).

127. Li, Y., Zhao, X. & Fan, W. Structural, electronic, and optical properties of Ag-doped ZnO nanowires: First principles study. *J. Phys. Chem. C* **115,** 3552–3557 (2011).

128. Thomas, M. A., Sun, W. W. & Cui, J. B. Mechanism of Ag doping in ZnO nanowires by electrodeposition: Experimental and theoretical insights. *J. Phys. Chem. C* **116,** 6383–6391 (2012).

129. Tynell, T. & Karppinen, M. Atomic layer deposition of ZnO: A review. *Semicond. Sci. Technol.* **29,** 043001 (2014).

130. Miikkulainen, V., Leskelä, M., Ritala, M. & Puurunen, R. L. Crystallinity of inorganic films grown by atomic layer deposition: Overview and general trends. *J. Appl. Phys.* **113,** 021301 (2013).

131. Janotti, A. & Van De Walle, C. G. Fundamentals of zinc oxide as a semiconductor. *Reports Prog. Phys.* **72,** 126501 (2009).

132. Gao, Z. & Banerjee, P. Review Article: Atomic layer deposition of doped ZnO films. *J. Vac. Sci. Technol. A* **37,** 050802 (2019).

133. Moulder, J. F. & Chastain, J. *Handbook of X-ray Photoelectron Spectroscopy: A Reference Book of Standard Spectra for Identification and Interpretation of XPS Data*. (Physical Electronics Division, Perkin-Elmer Corporation, 1992).

134. Kim, S. K., Hwang, C. S., Park, S. H. K. & Yun, S. J. Comparison between ZnO films grown by atomic layer deposition using H2O or O3 as oxidant. *Thin Solid Films* **478,** 103–108 (2005).

135. Park, J., Jung, T. H., Lee, J. H., Kim, H. S. & Park, J. S. The growth behavior and properties of atomic layer deposited zinc oxide films using hydrogen peroxide (H2O2) and ozone (O3) oxidants. *Ceram. Int.* **41,** 1839–1845 (2015).

136. Knoops, H. C. M., Elam, J. W., Libera, J. A. & Kessels, W. M. M. Surface loss in ozone-based atomic layer deposition processes. *Chem. Mater.* **23,** 2381–2387 (2011).

137. Bricalli, A., Ambrosi, E., Laudato, M., Maestro, M., Rodriguez, R. & Ielmini, D. Resistive Switching Device Technology Based on Silicon Oxide for Improved ON–OFF Ratio—Part II: Select Devices. *IEEE Trans. Electron Devices* **65,** 122–128 (2018).

138. Shukla, N., Grisafe, B., Ghosh, R. K., Jao, N., Aziz, A., Frougier, J., Jerry, M., Sonde, S., Rouvimov, S., Orlova, T., Gupta, S. & Datta, S. Ag/HfO2based threshold switch with extreme non-linearity for unipolar cross-point memory and steep-slope phase-FETs. *Tech. Dig. - Int. Electron Devices Meet. IEDM* 34.6.1-34.6.4 (2017). doi:10.1109/IEDM.2016.7838542

139. Grisafe, B., Jerry, M., Smith, J. A. & Datta, S. Performance Enhancement of Ag/HfO2 Metal Ion Threshold Switch Cross-Point Selectors. *IEEE Electron Device Lett.* **40,** 1602–1605 (2019).

140. Park, J., Yoo, J., Song, J., Sung, C. & Hwang, H. Hybrid Selector With Excellent Selectivity and Fast Switching Speed for X-Point Memory Array. *IEEE Electron Device Lett.* **39,** 1171–1174 (2018).

141. Lee, D., Kwak, M., Moon, K., Choi, W., Park, J., Yoo, J., Song, J., Lim, S., Sung, C., Banerjee, W. & Hwang, H. Various Threshold Switching Devices for Integrate and Fire Neuron Applications. *Adv. Electron. Mater.* **5,** 1800866 (2019).

142. Kim, S., Kim, M.-H., Kim, T.-H., Chen, Y.-C., Chang, Y.-F., Ismail, M., Kim, Y., Ryoo, K.-C. & Park, B.-G. Concurrent events of memory and threshold switching in Ag/SiNx/Si devices. *J. Vac. Sci. Technol. B* **36,** 051203 (2018).

143. Pung, S.-Y., Choy, K.-L., Hou, X. & Shan, C. Preferential growth of ZnO thin films by the atomic layer deposition technique. *Nanotechnology* **19,** 435609 (2008).

144. Malm, J., Sahramo, E., Perälä, J., Sajavaara, T. & Karppinen, M. Low-temperature atomic layer deposition of ZnO thin films: Control of crystallinity and orientation. *Thin Solid Films* **519,** 5319–5322 (2011).

145. Yuan, N. Y., Wang, S. Y., Tan, C. B., Wang, X. Q., Chen, G. G. & Ding, J. N. The influence of deposition temperature on growth mode, optical and mechanical properties of ZnO films prepared by the ALD method. *J. Cryst. Growth* **366,** 43–46 (2013).

146. Yousfi, E. B., Fouache, J. & Lincot, D. Study of atomic layer epitaxy of zinc oxide by in-situ quartz crystal microgravimetry. *Appl. Surf. Sci.* **153,** 223–234 (2000).

147. Jeon, S., Bang, S., Lee, S., Kwon, S., Jeong, W., Jeon, H., Chang, H. J. & Park, H.-H. Structural and Electrical Properties of ZnO Thin Films Deposited by Atomic Layer Deposition at Low Temperatures. *J. Electrochem. Soc.* **155,** H738–H743 (2008).

148. Makino, H., Miyake, A., Yamada, T., Yamamoto, N. & Yamamoto, T. Influence of substrate temperature and Zn-precursors on atomic layer deposition of polycrystalline ZnO films on glass. *Thin Solid Films* **517,** 3138–3142 (2009).

149. Kim, H. S., Lee, J. S., Kim, S. J., Lee, J., Lucero, A. T., Sung, M. M. & Kim, J. Realization of spatially addressable library by a novel combinatorial approach on atomic layer deposition: A case study of zinc oxide. *ACS Comb. Sci.* **21,** 445–455 (2019).

150. Langford, J. I. & Wilson, A. J. C. Scherrer after sixty years: A survey and some new results in the determination of crystallite size. *J. Appl. Crystallogr.* **11,** 102–113 (1978).

151. Ivanova, T., Homola, T., Bryukvin, A. & Cameron, D. Catalytic Performance of Ag2O and Ag Doped CeO2 Prepared by Atomic Layer Deposition for Diesel Soot Oxidation. *Coatings* **8,** 237 (2018).

152. Hämäläinen, J., Ritala, M. & Leskelä, M. Atomic layer deposition of noble metals and their oxides. *Chem. Mater.* **26,** 786–801 (2014).

153. Masango, S. S., Peng, L., Marks, L. D., Van Duyne, R. P. & Stair, P. C. Nucleation and growth of silver nanoparticles by AB and ABC-type atomic layer deposition. *J. Phys. Chem. C* **118,** 17655–17661 (2014).

154. Yuan, Z., Dryden, N. H., Vittal, J. J. & Puddephatt, R. J. Chemical Vapor Deposition of Silver. *Chem. Mater.* **7,** 1696 (1995).

155. Gaarenstroom, S. W. & Winograd, N. Initial and final state effects in the ESCA spectra of cadmium and silver oxides. *J. Chem. Phys.* **67,** 3500–3506 (1977).

156. Hagen, D. J., Pemble, M. E. & Karppinen, M. Atomic layer deposition of metals: Precursors and film growth. *Appl. Phys. Rev.* **6,** 041309 (2019).

157. Han, U.-B., Lee, D. & Lee, J.-S. Reliable current changes with selectivity ratio above 109 observed in lightly doped zinc oxide films. *NPG Asia Mater.* **9,** e351 (2017).

158. Park, Y., Han, U.-B., Kim, M.-K. & Lee, J.-S. Solution-Processed Flexible Threshold Switch Devices. *Adv. Electron. Mater.* **4,** 1700521 (2018).

159. Luo, Q., Xu, X., Liu, H., Lv, H., Gong, T., Long, S., Liu, Q., Sun, H., Banerjee, W., Li, L., Lu, N. & Liu, M. Cu BEOL compatible selector with high selectivity (> 107), extremely low off-current (~pA) and high endurance (> 1010). in *Int. Electron Devices Meet.* 10.4.1-10.4.4 (2015). doi:10.1109/IEDM.2015.7409669

160. Sun, Y., Song, C., Yin, S., Qiao, L., Wan, Q., Wang, R., Zeng, F. & Pan, F. Design of a Controllable Redox-Diffusive Threshold Switching Memristor. *Adv. Electron. Mater.* **6,** 1–20 (2020).

161. Yan, Y., Al-Jassim, M. M. & Wei, S. H. Doping of ZnO by group-IB elements. *Appl. Phys. Lett.* **89,** 87–90 (2006).

162. Roy, K., Jaiswal, A. & Panda, P. Towards spike-based machine intelligence with neuromorphic computing. *Nature* **575,** 607–617 (2019).

163. Takeuchi, K. Hybrid solid-state storage system with storage class memory and NAND flash memory for big-data application. *Proc. - IEEE Int. Symp. Circuits Syst.* 1046–1049 (2014). doi:10.1109/ISCAS.2014.6865318

164. Bakshi, K. Considerations for big data: Architecture and approach. *IEEE Aerosp. Conf. Proc.* 1–7 (2012). doi:10.1109/AERO.2012.6187357

165. Zhang, H., Chen, G., Ooi, B. C., Tan, K. L. & Zhang, M. In-Memory Big Data Management and Processing: A Survey. *IEEE Trans. Knowl. Data Eng.* **27,** 1920–1948 (2015).

166. Zhang, L., Cosemans, S., Wouters, D. J., Groeseneken, G., Jurczak, M. & Govoreanu, B. One-selector one-resistor cross-point array with threshold switching selector. *IEEE Trans. Electron Devices* **62,** 3250–3257 (2015).

167. Koo, Y. & Hwang, H. Zn1−xTex Ovonic Threshold Switching Device Performance and its Correlation to Material Parameters. *Sci. Rep.* **8,** 1–7 (2018).

168. Woo, J., Lee, D., Cha, E., Lee, S., Park, S. & Hwang, H. Control of Cu conductive filament in complementary atom switch for cross-point selector device application. *IEEE Electron Device Lett.* **35,** 60–62 (2014).

169. Liu, T., Verma, M., Kang, Y. & Orlowski, M. Volatile resistive switching in Cu/TaO x/δ-Cu/Pt devices. *Appl. Phys. Lett.* **101,** 2–5 (2012).

170. Wang, Z., Kumar, S., Williams, R. S., Nishi, Y. & Wong, H. S. P. Intrinsic limits of leakage current in self-heating-triggered threshold switches. *Appl. Phys. Lett.* **114,** (2019).

171. Li, H. Y., Huang, X. Di, Yuan, J. H., Lu, Y. F., Wan, T. Q., Li, Y., Xue, K. H., He, Y. H., Xu, M., Tong, H. & Miao, X. S. Controlled Memory and Threshold Switching Behaviors in a Heterogeneous Memristor for Neuromorphic Computing. *Adv. Electron. Mater.* **6,** (2020).

172. Wang, Z., Rao, M., Midya, R., Joshi, S., Jiang, H., Lin, P., Song, W., Asapu, S., Zhuo, Y., Li, C., Wu, H., Xia, Q. & Yang, J. J. Threshold Switching of Ag or Cu in Dielectrics: Materials, Mechanism, and Applications. *Adv. Funct. Mater.* **28,** (2018).

173. Park, J., Yoo, J., Song, J., Sung, C. & Hwang, H. Hybrid Selector With Excellent Selectivity and Fast Switching Speed for X-Point Memory Array. *IEEE Electron Device Lett.* **39,** 1171–1174 (2018).

174. Li, S., Liu, X., Nandi, S. K. & Elliman, R. G. Anatomy of filamentary threshold switching in amorphous niobium oxide. *Nanotechnology* **29,** (2018).

175. Sengottaiyan, R., Saxena, N. & Shukla, K. D. Rapid threshold switching dynamics of co-sputtered chalcogenide Ge 15 Te 85. *Semicond. Sci. Technol.* **36,** (2020).

176. Verdy, A., d'Acapito, F., Dory, J. B., Navarro, G., Bernard, M. & Noé, P. Effect of Nitrogen on the Amorphous Structure and Subthreshold Electrical Conduction of GeSeSb-Based Ovonic Threshold Switching Thin Films. *Phys. Status Solidi - Rapid Res. Lett.* **14,** 1–7 (2020).

177. Raty, J. Y. & Noé, P. Ovonic Threshold Switching in Se-Rich GexSe1−x Glasses from an Atomistic Point of View: The Crucial Role of the Metavalent Bonding Mechanism. *Phys. Status Solidi - Rapid Res. Lett.* **14,** 1–7 (2020).

178. Yoo, J., Woo, J., Song, J. & Hwang, H. Threshold switching behavior of Ag-Si based selector device and hydrogen doping effect on its characteristics. *AIP Adv.* **5,** (2015).

179. Ahn, H. W., Jeong, D. S., Cheong, B. K., Kim, S. D., Shin, S. Y., Lim, H., Kim, D. & Lee, S. A study on the scalability of a selector device using threshold switching in Pt/GeSe/Pt. *ECS Solid State Lett.* **2,** 31–34 (2013).

180. Lee, D., Kim, T. & Sohn, H. Highly reliable threshold switching behavior of amorphous Ga2Te3 films deposited by RF sputtering. *Appl. Phys. Express* **12,** 3–8 (2019).

181. Rupp, J. A. J., Waser, R. & Wouters, D. J. Vanadium Oxide for New Crossbar Selector. *IEEE Xplore* 7–10 (2016).

182. Song, J., Woo, J., Yoo, J., Chekol, S. A., Lim, S., Sung, C. & Hwang, H. Effects of Liner Thickness on the Reliability of AgTe/TiO2-Based Threshold Switching Devices. *IEEE Trans. Electron Devices* **64,** 4763–4767 (2017).

183. Van Den Hurk, J., Linn, E., Zhang, H., Waser, R. & Valov, I. Volatile resistance states in electrochemical metallization cells enabling non-destructive readout of complementary resistive switches. *Nanotechnology* **25,** (2014).

184. Hino, T., Hasegawa, T., Tanaka, H., Tsuruoka, T., Terabe, K., Ogawa, T. & Aono, M. Volatile and nonvolatile selective switching of a photo-assisted initialized atomic switch. *Nanotechnology* **24,** (2013).

185. Golden, T. D., Shumsky, M. G., Zhou, Y., VanderWerf, R. A., Van Leeuwen, R. A. & Switzer, J. A. Electrochemical Deposition of Copper(I) Oxide Films. *Chem. Mater.* **8,** 2499–2504 (1996).

186. Yamaguchi, Y., Yamazaki, M., Yoshihara, S. & Shirakashi, T. Photocatalytic ZnO films prepared by anodizing. *J. Electroanal. Chem.* **442,** 1–3 (1998).

187. Sun, Y., Zhao, X., Song, C., Xu, K., Xi, Y., Yin, J., Wang, Z., Zhou, X., Chen, X., Shi, G., Lv, H., Liu, Q., Zeng, F., Zhong, X., Wu, H., Liu, M. & Pan, F. Performance-Enhancing Selector via Symmetrical Multilayer Design. *Adv. Funct. Mater.* **29,** 1–9 (2019).

188. Francq, R., Snyders, R. & Cormier, P. A. Structural and Morphological study of ZnO-Ag thin films synthesized by reactive magnetron co-sputtering. *Vacuum* **137,** 1–7 (2017).

189. Musil, J., Baroch, P., Vlček, J., Nam, K. H. & Han, J. G. Reactive magnetron sputtering of thin films: Present status and trends. *Thin Solid Films* **475,** 208–218 (2005).

190. Chang, R. C., Chu, S. V., Lo, K. Y., Lo, S. C. & Huang, Y. R. Physical and structural properties of RF magnetron sputtered ZnO films. *Integr. Ferroelectr.* **69,** 43–53 (2005).

191. Jazmati, A. K. & Abdallah, B. Optical and structural study of ZnO thin films deposited by RF magnetron sputtering at different thicknesses: A comparison with single crystal. *Mater. Res.* **21,** 1–6 (2018).

192. Kunj, S. & Sreenivas, K. Defect free C -axis oriented zinc oxide (ZnO) films grown at room temperature using RF magnetron sputtering. *AIP Conf. Proc.* **1731,** 1–3 (2016).

193. Gan, K. J., Chang, W. C., Liu, P. T. & Sze, S. M. Investigation of resistive switching in copper/InGaZnO/Al2O3-based memristor. *Appl. Phys. Lett.* **115,** (2019).

194. Gao, W. & Li, Z. ZnO thin films produced by magnetron sputtering. *Ceram. Int.* **30,** 1155–1159 (2004).

195. Ondo-Ndong, R., Ferblantier, G., Al Kalfioui, M., Boyer, A. & Foucaran, A. Properties of RF magnetron sputtered zinc oxide thin films. *J. Cryst. Growth* **255,** 130–135 (2003).

196. Dave, P. Y., Patel, K. H., Chauhan, K. V., Chawla, A. K. & Rawal, S. K. Examination of Zinc Oxide Films Prepared by Magnetron Sputtering. *Procedia Technol.* **23,** 328–335 (2016).

197. Wang, W., Laudato, M., Ambrosi, E., Bricalli, A., Covi, E., Lin, Y.-H. & Ielmini, D. Volatile Resistive Switching Memory Based on Ag Ion Drift/Diffusion Part I: Numerical Modeling. *IEEE Trans. Electron Devices* **66,** 3795–3801 (2019).

198. Kozicki, M. N. & Barnaby, H. J. Conductive bridging random access memory - Materials, devices and applications. *Semicond. Sci. Technol.* **31,** 1–32 (2016).

199. Klaus, E. Magnetron sputtering of transparent conductive zinc oxide: relation between the sputtering parameters and the electronic properties. *J. Phys. D. Appl. Phys.* **33,** R17–R32 (2000).

200. Hu, Y. M., Li, J. Y., Chen, N. Y., Chen, C. Y., Han, T. C. & Yu, C. C. Effect of sputtering power on crystallinity, intrinsic defects, and optical and electrical properties of Al-doped ZnO transparent conducting thin films for optoelectronic devices. *J. Appl. Phys.* **121,** 085302 (2017).

201. Liu, F.-C., Li, J.-Y., Chen, T.-H., Chang, C.-H., Lee, C.-T., Hsiao, W.-H. & Liu, D.-S. Effect of Silver Dopants on the ZnO Thin Films Prepared by a Radio Frequency Magnetron Co-Sputtering System. *Materials (Basel).* **10,** 797 (2017).

202. Kang, H. S., Ahn, B. Du, Kim, J. H., Kim, G. H., Lim, S. H., Chang, H. W. & Lee, S. Y. Structural, electrical, and optical properties of p-type ZnO thin films with Ag dopant. *Appl. Phys. Lett.* **88,** 1–4 (2006).

203. Li, W. J., Kong, C. Y., Ruan, H. B., Qin, G. P., Huang, G. J., Yang, T. Y., Liang, W. W., Zhao, Y. H., Meng, X. D., Yu, P., Cui, Y. T. & Fang, L. Electrical properties and Raman scattering investigation of Ag doped ZnO thin films. *Solid State Commun.* **152,** 147–150 (2012).

204. Wang, X. B., Song, C., Geng, K. W., Zeng, F. & Pan, F. Luminescence and Raman scattering properties of Ag-doped ZnO films. *J. Phys. D. Appl. Phys.* **39,** 4992–4996 (2006).

205. Gaarenstroom, S. W. & Winograd, N. Initial and final state effects in the ESCA spectra of cadmium and silver oxides. *J. Chem. Phys.* **67,** 3500–3506 (1977).

206. Liu, Q., Long, S., Lv, H., Wang, W., Niu, J., Huo, Z., Chen, J. & Liu, M. Controllable growth of nanoscale conductive filaments in solid-electrolyte-based ReRAM by using a metal nanocrystal covered bottom electrode. *ACS Nano* **4,** 6162–6168 (2010).

207. Song, B., Cao, R., Xu, H., Liu, S., Liu, H. & Li, Q. A HfO2/SiTe based dual-layer selector device with minor threshold voltage variation. *Nanomaterials* **9,** (2019).

208. Shahrokhi, M. & Moradian, R. Structural, electronic and optical properties of Zn1−xZrxO nanotubes: first principles study. *Indian J. Phys.* **89,** 249–256 (2015).

209. Banerjee, W., Karpov, I. V., Agrawal, A., Kim, S., Lee, S., Lee, S., Lee, D. & Hwang, H. Highly-stable (< 3% fluctuation) Ag-based Threshold Switch with Extreme-low off Current of 0.1 pA, Extreme-high Selectivity of 109and High Endurance of 109Cycles. *Tech. Dig. - Int. Electron Devices Meet. IEDM* **2020-Decem,** 28.4.1-28.4.4 (2020).

210. Lee, S., Banerjee, W., Lee, S., Sung, C. & Hwang, H. Improved Threshold Switching and Endurance Characteristics Using Controlled Atomic-Scale Switching in a 0.5 nm Thick Stoichiometric HfO2 Layer. *Adv. Electron. Mater.* **7,** 1–8 (2021).

211. Song, J., Park, J., Moon, K., Woo, J., Lim, S., Yoo, J., Lee, D. & Hwang, H. Monolithic integration of AgTe/TiO2 based threshold switching device with TiN liner for steep slope field-effect transistors. *Tech. Dig. - Int. Electron Devices Meet. IEDM* 25.3.1-25.3.4 (2017). doi:10.1109/IEDM.2016.7838478

212. Samanta, S., Han, K., Das, S. & Gong, X. Improvement in Threshold Switching Performance Using AlO Interfacial Layer in Ag/AlO/SiO/W Cross-Point Platform. *IEEE Electron Device Lett.* **41,** 924–927 (2020).

213. Kim, S., Kim, Y. B., Kim, K. M., Kim, S. J., Lee, S. R., Chang, M., Cho, E., Lee, M. J., Lee, D., Kim, C. J., Chung, U. I. & Yoo, I. K. Performance of threshold switching in chalcogenide glass for 3D stackable selector. *Dig. Tech. Pap. - Symp. VLSI Technol.* (2013).

214. Shi, L., Zheng, G., Tian, B., Dkhil, B. & Duan, C. Research progress on solutions to the sneak path issue in memristor crossbar arrays. *Nanoscale Adv.* **2,** 1811–1827 (2020).

215. Abbas, H., Abbas, Y., Hassan, G., Sokolov, A. S., Jeon, Y. R., Ku, B., Kang, C. J. & Choi, C. The coexistence of threshold and memory switching characteristics of ALD HfO2memristor synaptic arrays for energy-efficient neuromorphic computing. *Nanoscale* **12,** 14120–14134 (2020).

216. James, A. P. & Chua, L. O. Analog Neural Computing With Super-Resolution Memristor Crossbars. *IEEE Trans. Circuits Syst. I Regul. Pap.* 1–12 (2021). doi:10.1109/TCSI.2021.3079980

217. Yao, P., Wu, H., Gao, B., Tang, J., Zhang, Q., Zhang, W., Yang, J. J. & Qian, H. Fully hardware-implemented memristor convolutional neural network. *Nature* **577,** 641–646 (2020).

218. Li, Y. & Ang, K.-W. Hardware Implementation of Neuromorphic Computing Using Large-Scale Memristor Crossbar Arrays. *Adv. Intell. Syst.* **3,** 2000137 (2021).

BIOGRAPHICAL SKETCH

Akshay Sahota is a doctoral student in the Electrical Engineering department in the Erik Jonsson School of Engineering and Computer Science at The University of Texas at Dallas (UTD), TX, USA. He received his (MTech + BTech) Dual degree in Electronics and Electrical Communication Engineering from Indian Institute of Technology (IIT) Kharagpur, Kharagpur, West Bengal, India in 2015. He was ranked in top 0.1% of 480,000 students (All India Rank-373) who wrote the Joint Entrance Examination (JEE) for IITs. During his time at IIT Kharagpur, in 2013, he was selected for a summer research internship program at Indian Institute of Science (IISc) - Bengaluru, Karnataka, India. During 2015-2016, he worked at Huawei Telecommunications Pvt. Ltd. as an engineer in Gurugram, Haryana, India. After that he studied for the GRE and TOEFL exams in order to apply for PhD positions and he was admitted to the doctoral program in Electrical Engineering department in Solid State Devices and Micro Systems Fabrication at UTD in Fall 2018. He currently maintains a good academic standing with a 4.0 GPA. His research interests include silver-based zinc oxide (ZnO) thin films' integration and characterization for threshold switching selectors, 3D X-point array, 1F1S neuromorphic circuits. He received the All-India Council for Technical Education (AICTE) GATE scholarship in 2015. Moreover, he also received merit based OK Kyun Kim and Youngmoo Cho Kim Graduate Fellowship two times consecutively in 2020 and 2021 and was a recipient of in-state tuition competitive scholarship waiver in 2020 and 2021.

CURRICULUM VITAE

Akshay Sahota

Department of Electrical and Computer Engineering

The University of Texas at Dallas

800 West Campbell Rd, TX 75080

Email: Akshay.Sahota@utdallas.edu

Education:

• The University of Texas at Dallas; PhD in Electrical Engineering, Sep 2021; Dissertation: "A Steep-slope Threshold Switching Selector Using Silver-doped Polycrystalline Zinc Oxide: Fabrication, Characterization, & Application for 3D X-Point Memory & Neuromorphic Devices".

• Indian Institute of Technology (IIT) Kharagpur; Dual Degree (MTech + BTech) in Electronics and Electrical Communication Engineering, June 2015.

Professional Experience:

• Engineer, Huawei Telecommunications Pvt. Ltd., Gurugram, Haryana, India, Aug 2015- July 2016.

Honors and Awards:

OK Kyun Kim and Youngmoo Cho Kim Graduate Fellowship, UT Dallas, 2020 & 2021

In-state tuition competitive scholarship waiver, UT Dallas, 2020 & 2021

Ranked 1st for Best Poster Award (co-author), Non-Volatile Memory Technology Symposium 2019, Durham, NC, US, 2019

All-India Council for Technical Education (AICTE) GATE scholarship, IIT Kharagpur, 2015

Publications:

1. Kim, H. S., Sahota, A., Mohan, J., Lucero, A. T., Chan Jung, Y., Kim, M., Lee, J., Choi, R., Kim, S. J., & Kim, J. (2021). Extremely low leakage threshold switch with enhanced characteristics via Ag doping on polycrystalline ZnO fabricated by facile electrochemical deposition for an X-point selector. *ACS Applied Electronic Materials*, 3, 2309–2316. https://doi.org/10.1021/acsaelm.1c00197
2. Jung, Y. C., Mohan, J., Hwang, S. M., Kim, J., Le, D. N., Sahota, A., Kim, N., Hernandez-Arriaga, H., Veyan, J., Kim, H. S., Kim, S. J., Choi, R., & Kim, J. (2021). A novel combinatorial approach to the ferroelectric properties in Hf X Zr 1− X O 2 deposited by atomic layer deposition. *Physica Status Solidi (RRL) – Rapid Research Letters*, 2100053. doi:10.1002/pssr.202100053
3. Hwang, S. M., Kim, H. S., Le, D. N., Ravichandran, A. V., Sahota, A., Lee, J., Jung, Y. C., Kim, S. J., Ahn, J., Hwang, B. K., Lee, L., Zhou, X., & Kim, J. (2021). Plasma-enhanced atomic-layer deposition of nanometer-thick SiNx films using Trichlorodisilane for etch-resistant coatings. *ACS Applied Nano Materials*, 4(3), 2558-2564. https://doi.org/10.1021/acsanm.0c03203
4. Kim, S. J., Mohan, J., Kim, H. S., Hwang, S. M., Kim, N., Jung, Y. C., Sahota, A., Kim, K., Yu, H., Cha, P., Young, C. D., Choi, R., Ahn, J., & Kim, J. (2020). A comprehensive study on the effect of tin top and bottom electrodes on atomic layer deposited ferroelectric Hf0.5Zr0.5O2 thin films. *Materials*, 13(13), 2968. https://doi.org/10.3390/ma13132968
5. Kim, H. S., Hwang, S. M., Meng, X., Byun, Y., Jung, Y. C., Ravichandran, A. V., Sahota, A., Kim, S. J., Ahn, J., Lee, L., Zhou, X., Hwang, B. K., & Kim, J. (2020). High growth rate and high wet etch resistance silicon nitride grown by low temperature plasma enhanced atomic layer deposition with a novel silylamine precursor. *Journal of Materials Chemistry C*, 8(37), 13033-13039. https://doi.org/10.1039/d0tc02866e
6. Sahota, A., Kim, H. S., Mohan, J., Jung, Y. C., Hernandez-Arriaga, H., Le, D. N., Kim, S. J., Lee, J.S.-, Ahn, J., & Kim, J. (2021). Highly Reliable Selection Behavior with Controlled Ag Doping of Nano-polycrystalline ZnO Layer for 3D X-Point Framework. *IEEE Electron Device Letters* (*under journal review*)

7. Sahota, A., Kim, H. S., Mohan, J., Le, D. N., Jung, Y. C., Kim, S. J., Lee, J.S.-, Ahn, J., Hernandez-Arriaga, H., & Kim, J. (2021). Nano-polycrystalline Ag doped ZnO layer for steep-slope threshold switching selectors. *AIP Advances* (*under journal review*)
8. *Kim, H. S., *Sahota, A., Meng, X., Mohan, J., Jung, Y. C., Lee, J.S.-, Kim, S. J., & Kim, J. (2021). Novel Approach using Atomic Layer Deposition of Ag Doped O_3-based Crystalline ZnO Films for Ultra-Steep Threshold Switching Selector. *Advanced Functional Materials* (*in-preparation*) *equal contributors

Conferences:

1. A. Sahota, H. S. Kim, J. Mohan, D. N. Lee, Y. C. Jung, S. J. Kim, J.S.- Lee, J. Ahn, H. Hernandez-Arriaga, and J. Kim, "Nano-polycrystalline Ag doped ZnO layer for steep-slope threshold switching selectors", 2021 International Workshop on Dielectric Thin Films for Future Electron Devices: Science and Technology (2021 IWDTF), Tokyo, Japan, 2021 (oral presentation – *accepted*)
2. A. Sahota, H. S. Kim, J. Mohan, Y. C. Jung, H. Hernandez-Arriaga, and J. Kim, "Highly Reliable Ultra-Steep Slope Threshold Switching Behavior with Controlled Ag Doping of Nano-polycrystalline ZnO Layer", 52nd IEEE Semiconductor Interface Specialists Conference (SISC), San Diego, CA, US, 2021 (poster presentation – *accepted*)
3. A. Sahota, H. S. Kim, J. Mohan, Y. C. Jung, and J. Kim, "Engineering Ag-based ZnO Thin Films to Reduce V_{th} Variability in Filament-type Threshold Switching Selectors for 3D Cross-point Memory Application", 51st IEEE Semiconductor Interface Specialists Conference (SISC), San Diego, CA, US, 2020 (poster presentation)
4. H. S. Kim, A. Sahota, J. Mohan, Y. C. Jung, and J. Kim, "Engineering Ag Doping Profile for Investigating Volatile Switching Characteristics to Reduce V_{th} Variability on CBRAM-type Selectors for Cross-point Array Application", 50th IEEE Semiconductor Interface Specialists Conference (SISC), San Diego, CA, US, 2019
5. H. S. Kim, A. Sahota, J. Mohan, Y. C. Jung, and J. Kim, "Volatile Switching Characteristics Per Doping Criteria for Understanding Improved Reliability on Ag-based

Selector", Non-Volatile Memory Technology Symposium 2019 (NVMTS 2019), Durham, NC, US, 2019 (*Ranked 1st for Best Poster's Award*)

6. H. S. Kim, A. Sahota, J. Mohan, H. Hernandez-Arriaga, and J. Kim, "Understanding the Improved Reliability on Ag-based Ultra-steep Threshold Switching Selectors for Cross-point Array", SRC TECHCON 2019, Austin, TX, US, 2019
7. H. S. Kim, A. Sahota, J. Mohan, H. Hernandez-Arriaga, and J. Kim, "Atomic Layer Deposited Crystalline Zinc Oxide for Silver-based Ultra-Steep Threshold Switching Selector", 19th International Conference on Atomic Layer Deposition, Bellevue, WA, US, 2019
8. J. Mohan, H. Hernandez-Arriaga, H. S. Kim, A. Khosravi, A. Sahota, R. M. Wallace, and J. Kim, "Scaling ferroelectric $Hf_{0.5}Zr_{0.5}O_2$ on Metal-Ferroelectric-Metal (MFM) and Metal-Ferroelectric-Insulator-Semiconductor (MFIS) structures", 19th International Conference on Atomic Layer Deposition, Bellevue, WA, US, 2019
9. H. S. Kim, A. Sahota, J. Mohan, H. Hernandez-Arriaga, and J. Kim, "Silver-based Reliable Ultra-steep Threshold Switching Selector for Cross-bar Array", 2019 Insulating Films on Semiconductors (INFOS 2019), Clare College, Cambridge University, Cambridge, UK, 2019